

**VISIBLE AND NEAR INFRARED SENSITIVE
PHOTOREFRACTIVE POLYMERS
FOR HOLOGRAPHIC DISPLAY APPLICATIONS**

by
Muhsin Eralp

A Dissertation Submitted to the Faculty of the
COLLEGE OF OPTICAL SCIENCES
In Partial Fulfillment of the Requirements
For the Degree of
DOCTOR OF PHILOSOPHY
In the Graduate College
THE UNIVERSITY OF ARIZONA

2007

THE UNIVERSITY OF ARIZONA
GRADUATE COLLEGE

As members of the Dissertation Committee, we certify that we have read the dissertation prepared by Muhsin Eralp

entitled "Visible and Near Infrared Sensitive Photorefractive Polymers for Holographic Display Applications"

and recommend that it be accepted as fulfilling the dissertation requirement for the Degree of Doctor of Philosophy

_____ Date: 03/07/2007
Nasser Peyghambarian, Dissertation Director

_____ Date: 03/07/2007
Robert A. Norwood, Member

_____ Date: 03/07/2007
Mahmoud Fallahi, Member

_____ Date: _____

_____ Date: _____

Final approval and acceptance of this dissertation is contingent upon the candidate's submission of the final copies of the dissertation to the Graduate College.

I hereby certify that I have read this dissertation prepared under my direction and recommend that it be accepted as fulfilling the dissertation requirement.

_____ Date: 03/07/2007
Dissertation Director: Nasser Peyghambarian

STATEMENT BY AUTHOR

This dissertation has been submitted in partial fulfillment of requirements for an advanced degree at The University of Arizona and is deposited in the University Library to be made available to borrowers under rules of the Library.

Brief quotations from this dissertation are allowable without special permission, provided that accurate acknowledgment of source is made. Requests for permission for extended quotation from or reproduction of this manuscript in whole or in part may be granted by the head of the major department or the Dean of the Graduate College when in his or her judgment the proposed use of the material is in the interests of scholarship. In all other instances, however, permission must be obtained from the author.

SIGNED: Muhsin Eralp

ACKNOWLEDGEMENTS

I would like to express my gratitude to my academic advisor, Professor Nasser Peyghambarian, for providing me with a great opportunity to conduct my research on this dissertation and motivating me throughout the years. He gave me the freedom and opportunity to choose and to explore a broad spectrum of research that I could not have found anywhere else. Additionally, I would like to extend my deepest gratitude to Dr. Robert A. Norwood for his direction and supervision in parts of my dissertation work. I have greatly benefited from both his superior knowledge and his kind personality. I want to thank Professor Mahmoud Fallahi for serving on my committee. I would like to acknowledge, Jayan Thomas, a great colleague whose hard work and patient collaboration brought success to this difficult project. Finally, I would also extend my thanks to Savas Tay, Pierre A. Blanche, Axel Schulzgen, Yushi Kaneda, Guoqiang Li, Michi Yamamoto and Peng Wang at Nitto Denko Technical, Y. A. Merzlyak and Mike Morrell for their valuable contributions to my research.

I thank my many colleagues at the College of Optical Sciences, who became my friends, contributed to my intellectual development, and made life outside of school pleasant.

DEDICATION

This work is dedicated to my parents who have always wished the best for me throughout my life.

TABLE OF CONTENTS

LIST OF FIGURES	8
LIST OF TABLES	13
ABSTRACT	14
1 INTRODUCTION.....	16
1.1 Photorefractive Effect	17
1.2 Motivation for Development of Photorefractive Polymers	20
1.3 Organization of the Present Work.....	23
2 FUNDAMENTALS OF PHOTOREFRACTIVITY	24
2.1 Photogeneration	27
2.2 Transport and Trapping.....	31
2.3 Build-up of Space-charge Field	39
2.3.1 <i>Kuktharev Model</i>	40
2.3.2 <i>Model for Polymers</i>	43
2.4 Physics of Poled Polymers.....	47
2.4.1 <i>First-Order (Linear) Optical Properties</i>	52
2.4.2 <i>Second-Order Nonlinear Optical Properties of Poled Polymers</i>	53
2.5 Refractive Index Modulation	57
2.5.1 <i>Purely Electro-optic Polymers</i>	57
2.5.2 <i>Low Glass Transition Temperature Polymers - Orientational Enhancement</i>	58
2.6 Diffraction Theory of Thick Gratings.....	63
2.6.1 <i>Transmission Geometry</i>	65
2.6.2 <i>Reflection Geometry</i>	70
2.7 Two-Beam Coupling (Self Diffraction) Theory	74
3 MATERIAL DEVELOPMENT	78
3.1 Guest-Host Polymer Composites.....	78
3.1.1 <i>Sensitizers</i>	81
3.1.2 <i>Transport Matrices</i>	82
3.1.3 <i>NLO Chromophores</i>	82
3.1.4 <i>Plasticizers</i>	83
3.2 Fully-Functionalized Polymers.....	83
3.3 Amorphous Glasses	83
3.4 Polymer Dispersed Liquid Crystals	84
3.5 Hybrid Organic Inorganic Composites	85
4 EXPERIMENTAL TECHNIQUES	86
4.1 Sample Preparation	86

TABLE OF CONTENTS - Continued

4.2	Probing Various Sub-processes Relevant to Photorefractivity.....	88
4.2.1	<i>Linear Absorption Properties</i>	88
4.2.2	<i>Photoconductive Properties</i>	89
4.2.3	<i>Orientalional Properties</i>	91
4.3	Photorefractive Measurements.....	95
4.3.1	<i>Sample Geometry</i>	95
4.3.2	<i>Four-Wave Mixing</i>	97
4.3.3	<i>Two-Beam Coupling</i>	105
5	RESULTS AND DISCUSSIONS.....	107
5.1	Reducing the Bias Voltage in Photorefractive Polymers.....	108
5.1.1	<i>Mixture of Chromophores</i>	109
5.1.2	<i>Reducing the Thickness</i>	109
5.1.3	<i>Material and Characterization</i>	110
5.2	Photorefractive Polymers Operating at NIR Wavelengths	116
5.2.1	<i>975nm</i>	117
5.2.2	<i>845nm</i>	124
5.3	Single-Pulse Gratings in Photorefractive Polymers.....	126
5.3.1	<i>Material Approach</i>	127
5.3.2	<i>Reading PR grating through 532nm and 633nm wavelengths</i>	127
5.3.3	<i>Submillisecond Response</i>	129
5.3.4	<i>100Hz Frame Rate</i>	132
5.4	Improving the Grating Persistence in Photorefractive Polymer Composites .	134
5.4.1	<i>Copolymer Approach</i>	135
5.4.2	<i>Thermal Fixing</i>	139
5.5	Large Efficiency in Reflection Geometry.....	142
5.5.1	<i>Sample Composition and Characterization</i>	142
5.5.2	<i>Analysis of Results in Reflection Geometry</i>	147
6	CONCLUSION AND OUTLOOK.....	152
	ABBREVIATIONS.....	156
	PUBLICATIONS & TALKS RELATED TO THIS WORK	158
	REFERENCES.....	159

LIST OF FIGURES

Figure 2-1: Schematic representation of the photorefractive effect in the case of a sinusoidal light pattern. A replica of the light pattern in terms of spatial refractive index variation (phase grating) is obtained. Notice that the phase grating is phase shifted compared to the light grating.	26
Figure 2-2: Schematic diagram of energy levels in a molecule. The first absorption (lowest energy) peak occurs when an electron is excited from the HOMO level to the LUMO.	28
Figure 2-3: The photogeneration process in organic photoconductors.....	28
Figure 2-4: Onsager curves for the field dependence of the quantum efficiency over a range of thermalization radii, r_0 ($T=300\text{K}$, $\epsilon = 3.5$).	30
Figure 2-5: Typical absorption band in a charge-transfer (CT) complex. Note that there is an additional absorption at longer wavelengths.	31
Figure 2-6: In disorder formalism, the energy distribution of hopping sites is assumed to have a Gaussian distribution.	34
Figure 2-7: The behavior of the electron-transfer rate predicted by Marcus theory. Notice the unusual behavior in the inverted regime. λ is the reorganization energy.	36
Figure 2-8: (a) Energy levels for acceptor and donor molecules as well as the charge-transfer complex (b) The processes involved as a photon is absorbed in the system.	37
Figure 2-9: Schematic representation of the charge generation, transport, trapping and recombination in organic photorefractive materials. Note that transport is through hopping from one molecule to another or through conjugated side-chains of the polymer matrix.	39
Figure 2-10: The amplitude (a) and phase (b) of the space-charge field as a function of applied field.	42
Figure 2-11: The phase and amplitude of the space-charge field as a function of applied field in the case of polymers.	46
Figure 2-12: Schematic of push-pull molecules (chromophores) for electro-optic and photorefractive applications.	48
Figure 2-13: Random dipole orientation in the cases of no field (isotropic) (a) and with field (non-centrosymmetric) (b). Note that, in isotropic and amorphous systems $\chi^{(2)} = 0$	49
Figure 2-14: Schematic of an individual rodlike molecule in the laboratory frame $\{X, Y, Z\}$ when an electric field is applied along the Z axis. $\{x,y,z\}$ is the frame attached to the molecule.	51
Figure 2-15: Ground state and first excited state of a push-pull molecule.	55
Figure 2-16: The total poling field in a low glass transition temperature polymer for standard slanted transmission geometry. Notice that the overall pattern is a combination of fixed external field and the periodically varying space-charge field.	60

Figure 2-17: Schematic representation of diffraction orders for Bragg (a) and Raman-Nath (b) regimes.	64
Figure 2-18: Schematic of slanted transmission geometry used in four-wave mixing experiments. In our standard transmission geometry $\theta_1 = 50^\circ$ and $\theta_2 = 70^\circ$. Therefore, the slant angle of grating, φ , becomes 58.8° for a refractive index of 1.65.	66
Figure 2-19: The effect of applied electric field (a) and grating spacing (b) on the diffraction efficiency of a photorefractive transmission grating. Two different cases of effective trap densities are considered.	69
Figure 2-20: The diffraction efficiency for a lossless phase grating under Bragg-mismatch conditions (transmission geometry).	70
Figure 2-21 : Schematic of the reflection geometry used in four-wave mixing experiments. In our standard symmetric reflection geometry $\theta_1 = \theta_2 = 72^\circ$, and $\varphi = 0$	71
Figure 2-22: The effect of applied electric field (a) and grating spacing (b) on the diffraction efficiency of a photorefractive reflection grating. Two different cases of effective trap densities are considered.	73
Figure 2-23: The diffraction efficiency for a lossless phase grating under Bragg-mismatch conditions (reflection geometry).	74
Figure 2-24: Two beam coupling geometry: energy is transferred from the pump beam into the probe beam.	75
Figure 2-25: The effect of applied electric field and grating spacing on the two-beam coupling gain of a photorefractive transmission grating. Two different cases of effective trap densities are considered.	77
Figure 3-1: Typical guest-host system. The functional elements are added into the polymer matrix.	79
Figure 3-2: Molecular structures for sensitizers commonly used in our guest-host polymer systems. C_{60} provides sensitivity in the red, TNFDM:PATPD provides absorption in the NIR (700-850nm) due to charge-transfer complex and DBM dye provides absorption for 900-1000nm region. Absorption at 532nm is obtained through the 7-DCST chromophore (see Figure 3-4).	81
Figure 3-3: Molecular structures for photoconducting polymers commonly used in our guest-host polymer systems. PATPD matrix has more conjugated sites, therefore better charge mobility.	82
Figure 3-4: Molecular structures for NLO chromophores commonly used in our guest-host polymer systems. 7-DCST is a smaller chromophore, therefore it has a faster orientation speed. 7-DCST also provides the necessary absorption at 532nm.	82
Figure 3-5: Molecular structures for plasticizer commonly used in our guest-host polymer systems.	83
Figure 4-1: Typical DSC measurement curve. The first drop in the heat flow is referred as T_g (glass transition temperature). The peak in the curve is at T_c (crystallization temperature) and the dip is at T_m (melting temperature)	88

- Figure 4-2: The Index ellipsoid: a p-polarized beam will sense both ordinary and the extra-ordinary refractive index. 92
- Figure 4-3: Schematic diagram of a transmission ellipsometry setup. 93
- Figure 4-4: Typical experimental transmittance curve for ellipsometry data. The fit is based on quadratically varying index modulation. 94
- Figure 4-5: The slanted transmission geometry with 532nm writing beams and 532nm/633nm reading beams. Notice that, the Bragg-matched angle depends on reading wavelength. 96
- Figure 4-6: Symmetric reflection geometry. 97
- Figure 4-7: Experimental setup used in four-wave mixing and two-beam coupling experiments. Note that many different lasers can be coupled into this system, simply through a replaceable mirror. 99
- Figure 4-8: Adjusting the reading angle without moving the spot in the test sample. The fast camera lens helps to fine tune the Bragg-matched angle for best condition which will result in 100% diffraction efficiency. 102
- Figure 5-1: Steady-state diffraction efficiency for both 20 μm and 105 μm thick devices, as the bias voltage is increased. The peak internal diffraction efficiency of the 20 μm device was 80%. External efficiency was around 58%, which is higher than a similar thick device, due to the low absorption of the thin device. 112
- Figure 5-2: (a) Typical growth of diffraction efficiency when one of the writing beams is switched on. The line is a biexponential fit. The total writing beam irradiance was $1\text{W}/\text{cm}^2$ and a bias voltage of 1.4 kV was applied through the device. (b) The net diffraction efficiency is recorded as one writing beam is modulated at 1-30Hz (full cycle write and erase) frequency. The inset shows the response of the photorefractive device at a 30Hz frame rate. 114
- Figure 5-3: The drop of peak efficiency as the state of the hologram is changed from thick (Bragg) to thin (Raman-Nath). The grating spacing is increased to vary the Kogelnik's Q value. The shift in the peak efficiency reveals the growth in index modulation with increased grating spacing. 115
- Figure 5-4: Absorption spectrum of the dye is shown near the wavelength under consideration. Chemical structure of the sensitizing dye is also shown. Close to linear intensity dependence [$\sigma \sim I^{0.93}$ (C1, open circles) and $\sigma \sim I^{0.85}$ (C2, dark circles)] of the photoconductivity is observed at an electric field of 56 V/ μm (inset). 118
- Figure 5-5: Steady-state diffraction efficiency vs external electric field for both C2 (open circles) and C1 (dark squares); the solid line is a theoretical fit for a trap density of $2.3 \times 10^{16} \text{ cm}^{-3}$. Transient growth of the diffraction efficiency as the second writing beam is turned on for C2 is shown in the inset. The solid line in the inset is a bi-exponential growth fit ($\tau_1=33\text{ms}$, $\tau_2=320\text{ms}$, weight factor $m=0.5$). 121
- Figure 5-6: The electric field dependence of the two beam coupling gain coefficient of C2 (open triangles) and C1 (dark triangles) for p-polarized writing beams. The absorption coefficient $\alpha=13 \text{ cm}^{-1}$ is included for comparison. 123

- Figure 5-7: (a) The absorption spectra of the sample sensitive at 845nm, (b) the transient response (inset) and steady-state diffraction efficiency curves 125
- Figure 5-8: The steady-state diffraction efficiency when read through green (circles) and red (square) beams. The slanted transmission geometry used in the writing process is shown in the inset. The red reading beam comes in a slightly different angle to achieve the Bragg condition. The peak of the efficiency is reached at different fields for different reading wavelengths. 129
- Figure 5-9: The fast rise and decay of diffraction efficiency of PATPD: 7-DCST: ECZ: C₆₀ (54.5:25:20:0.5 wt. %) when exposed to two interfering single pulses of 1 ns pulsewidth with total 4mJ/cm² fluence. The bias field was kept at 95V/μm and the reading beam wavelength was at 633nm. The internal efficiency reached a maximum of 56% (or 35% efficiency after all losses) in only 1.8ms time. The fast time constant for the rise section of the curve is 300μs. The line is an exponential fit function with four time constants (2 for the rise and 2 for the decay). 131
- Figure 5-10: The single-pulse diffraction efficiency when the total pulse energy is varied as 0.2, 0.38, 0.75, 1.5, 3.0 mJ/cm². The maximum diffraction efficiency increases linearly with the pulse energy for the most part. 132
- Figure 5-11: The decay of the grating diffraction efficiency is accelerated through a separate, uniform cw illumination at 532nm. The gated illumination lasted only 5ms (gray window) with an exposure of 6mJ/cm². The grating is totally erased 10ms after the pulse arrived. This fast rise and decay proves that we can operate this device at 100Hz (write and erase) frame rates using single pulse writing and gated erasure. 133
- Figure 5-12: The rise and decay of diffraction efficiency in the case of composites based on (a) homopolymer [PATPD:7DCST:ECZ:C₆₀] and (b) copolymer [(TPD:CbZ:DCST/5:5:1) Copolymer: 7F-DCST:ECZ]. The writing was through a single-pulse beam at 532nm with 1ns pulsewidth, 2.5mJ/cm² energy and the reading was with a cw 633nm beam. 138
- Figure 5-13: The photo and dark current values for PR composites with 3 different copolymer transport elements at 25 °C (a) and at 42 °C (b). TPD:DCST (10:1) copolymer has the largest photocurrent, while CbZ:DCST (10:1) copolymer has the lowest. Note that at elevated temperatures, the dark current becomes very strong and washes out the grating. 139
- Figure 5-14: Water-cooled thermoelectric apparatus used for thermal fixing tests..... 140
- Figure 5-15: The long decay curve for a thermally fixed PR device. The writing was done above 40 °C and the device is left to decay at 16 °C..... 141
- Figure 5-16: (a) Variation of the diffraction efficiency with respect to the external readout angle mismatch (p-polarized readout). As the mismatch angle is varied, the diffraction efficiency peaks at different field values. The line is the case without birefringence. The case for s-polarized readout is given in (b). An offset angle is not needed in the case of s-polarized readout 145

- Figure 5-17: The build-up of the diffraction efficiency as the second writing beams is switched on. The data is fitted to a bi-exponential growth function. The fast and slow time constants are given in the inset. The bias voltage was $76\text{V}/\mu\text{m}$ 146
- Figure 5-18: Variation of the diffraction efficiency curve with respect to the external readout angle mismatch (p-polarized readout) including the fitted curves based on theory. 149
- Figure 5-19: Variation of diffraction efficiency as a function of bias field for the composition PVK:7-DCST:ECZ:BBP:C₆₀ (49.5:35:10:5:0.5 wt.%). Each curve has a slight offset by the amount shown in the inset. 151

LIST OF TABLES

Table 1-1: General properties of recording materials used in holography	22
Table 5-1: Summary table for C1 and C2. Conductivity values given are at 56V/ μm applied field and 1W/cm ² intensity. Diffraction efficiencies and response times are measured at 95V/ μm . Speed is determined from $[mt_1+(1-m)t_2]^{-1}$. τ_g is the time constant from the stretched exponential fit (see Section 4.3.2).	122

ABSTRACT

This work presents recent advances in photorefractive polymer composites towards improved efficiency, speed, persistence of holograms and sensitivity at both visible and near infrared wavelengths. Besides the pure performance characteristics, a thin-device approach is presented to reduce operating voltage of these devices to practical levels and these materials are analyzed in both reflection and transmission geometries.

The thin device operating at 1.3kV holds erasable, Bragg holograms with 80% efficiency in addition to its video-rate response time. The transition of hologram state from 'thick' to 'thin' is analyzed in detail. On the near IR portion of spectrum, new photorefractive polymer composites have been developed that enable high performance operation at 845nm and 975nm. Utilizing our novel photorefractive materials we demonstrate large diffraction efficiency in four-wave mixing experiments and video-rate response times. A major step towards achieving submillisecond response times is obtained through recording photorefractive gratings with individual nanosecond pulses at 532nm. At 4 mJ/cm² illumination, a maximum diffraction efficiency of 56% has been obtained with a build-up time of only 300μs (t_I). This fast response enables applications in optical processing requiring frame rates of 100Hz or more. Due to the short duration of the writing pulses, the recording is insensitive to vibrations. Combining molecules that have different frontier orbital energies in a copolymer system and utilizing thermal fixing approach has led to long grating lifetimes of more than several hours. Later, in this dissertation, two low-glass-transition photorefractive polymer composites are investigated in reflection geometry. 60% is diffraction efficiency is observed in 105μm

thick devices of a PVK based composite. The reflection holograms are more sensitive to reading angle and slight birefringence due to the poling of chromophores has proven to cause a Bragg mismatch.

1 INTRODUCTION

We live in a world that is driven by the power of information. The flow of information has grown enormously in recent time. Optical technologies, in particular, are a key enabler for transporting, processing, storing and displaying the large amount of information. The development of optical technologies relies heavily on the progress achieved in fabricating innovative materials with high performance at low cost. Among many different materials, plastics or synthetic polymers are expected to play a key role in development of future optical technologies, due to their chemical flexibility and low cost.

Initially, organic materials and especially polymeric materials were mainly used for their structural, insulating, and dielectric properties. Later, polymers played a critical role in advancing the semiconductor industry by enabling large scale integration through the development of UV and electron beam lithographic resists. In recent decades, new functionalities such as electrical, electro-optical, and light-emission properties have been built into organic materials and polymers. Organic materials are currently used in electro-optic modulators,¹ organic light emitting diodes (OLED),^{2,3} photo-voltaic devices,^{4,5} transistors,^{6,7} and in many other photonics applications.⁸ Their performance has been improved significantly to the levels where they outperform their best inorganic counterparts. For instance, electro-optic polymers with electro-optic activities much higher than LiNbO₃ crystal, a standard in the electro-optic industry, have been demonstrated.⁹ Over the years, the environmental and thermal properties of polymers for photonic devices have matured considerably. Other breakthroughs were seeded by the development of new processing technologies. Organic materials can be fabricated with

inexpensive techniques such as spin casting, photolithography,¹⁰ ink-jet printing,¹¹ and commonly used injection molding.¹² The early development of electro-optic and photoconducting polymers for optical switches and xerography helped photorefractive polymers to experience rapid development. Among the many groups of organic materials, photorefractive polymers can potentially become the materials of choice for real-time optical processing and holographic storage applications.

1.1 Photorefractive Effect

The photorefractive (PR) effect refers to photo-induced change in refractive index of an optical material. The PR effect is reversible and is created through space-charge-field formation and electro-optic nonlinearity. It is important to avoid confusing the PR effect with the large number of other local reversible mechanisms which can modify the index of refraction of a material in response to an optical beam, such as photochromism, thermochromism, thermorefraction, etc. All of these local mechanisms lack the nonlocal aspect of the PR effect due to the phase shift between the light grating and phase grating. An important consequence of this phase shift is energy transfer between two light beams interfering in a PR medium, called asymmetric two-beam coupling (TBC).

The PR effect was first observed in 1966 in a LiNbO₃ crystal as optical damage.¹³ This discovery then launched extensive studies of the effect in inorganic crystals such as LiNbO₃, KNbO₃, BaTiO₃, Bi₁₂SiO₂₀ (BSO), Sr_xBa_{1-x}NbO₃, InP:Fe, GaAs, multiple-quantum-well semiconductors, and several others.^{14,15,16} In the 1990s, organic PR materials were developed.^{17,18} Since the first demonstration of photorefractivity in a

polymer,¹⁹ numerous polymer composites have been developed and the performance level of this new class of materials rapidly improved by several orders of magnitude, to a level where they outperform numerous inorganic crystals that are expensive and difficult to grow. Current materials can exhibit millisecond response times and can have refractive index modulation amplitude close to 0.01. A review of the most recent organic PR materials is given in Ref. 20.

The PR effect has not yet found wide-spread commercial applications in the case of inorganic materials. This can be attributed to the difficulty associated with the growth of crystals. Organic materials, on the other hand, offer low-cost, ease, flexibility of fabrication and tunability over the properties. In addition to that, organic materials can have relatively large figure of merit of nonlinearity compared to inorganics (10 times or more, depending on the molecular nonlinearity). The figure of merit doesn't vary much from material to material for the inorganic materials. On the other hand, for organic materials, nonlinearity is a molecular property arising from the asymmetry of the electronic charge distribution in the ground and excited states which determine the relative refractive index change possible in the materials.²⁰

The major disadvantages of organic materials are the requirement for high bias voltages, relatively short device lifetime, and susceptibility to temperature changes.

The ideal PR material would be sensitive over a wide spectral range, from the near-ultraviolet to the near-infrared. Unfortunately, there is no single material that can operate over this broad wavelength region. Many of the most efficient PR materials show

an optimum response in the visible region. In the near-infrared (NIR), the performance of PR materials has recently been optimized.^{21,22,23}

In recent years, outstanding gain coefficients have been reported in devices using nematic liquid crystals. Gain coefficients as large as 3700 cm^{-1} have been reported in devices which use photo-generated space charges developed in photoconducting layers to modulate the alignment of adjacent undoped liquid crystals.²⁴ However the operation of these devices has so far been restricted to the Raman-Nath regime, leading to multiple diffracted orders. Recently, hybrid organic-inorganic devices have shown large gain coefficients ($> 1600 \text{ cm}^{-1}$).²⁵ In these devices, inorganic PR crystals are used as windows for undoped nematic liquid crystal cells. The unexpectedly large gain has been attributed to the occurrence of a pre-tilt of the liquid crystal molecules at the inorganic window surfaces, leading to an induced molecular polarity through flexoelectric effect.²⁶

Synthetic efforts have resulted in a broad array of materials with 100% diffraction efficiencies and outstanding TBC gain coefficients at low electric fields over wide spectral ranges, including the NIR wavelength region. A number of ways to create thermodynamically stable materials with high optical quality have been proposed. PR response times on the order of milliseconds have been achieved in a variety of materials, including polymer composites, amorphous glasses and liquid crystals. Many of the previously proposed applications have been demonstrated and novel effects that may lead to new applications have been documented (see next section).

1.2 Motivation for Development of Photorefractive Polymers

Organic photorefractive materials have many potential applications that involve real-time holography. Large-scale PR polymer devices can be fabricated using one of the traditional plastic manufacturing technologies (injection molding) without compromising the PR performance.²⁷ Some examples of these applications are holographic data storage,²⁸ phase conjugation,^{29,30} image processing (correlation and pattern recognition),^{31,32} image amplification,^{33,34} dynamic holography,³⁵ imaging through scattering media,^{36,37} and 3D displays.

In the case of holographic data storage, PR polymers are attractive materials for rewriteable holographic storage applications because they display high diffraction efficiencies, in addition to having reasonable optical quality and in some cases long dark lifetimes. To obtain long data storage times a thermal fixing method has been proposed in a PR polymer composite.³⁸ Using angle multiplexing, many pages of data can be stored by changing the angle of the reference beam for each page of recording.

Phase conjugation, which is also referred to as “time reversal”, produces a replica of an optical beam that propagates through space with the complex conjugate phase of the original beam, which may be viewed as propagation backward in time.³⁰ The potential applications of phase conjugation include the transmission of undistorted images through the atmosphere,³⁹ phase locking of lasers and optical interferometry.

Applications involving rewritable 3D displays are a new application direction for PR polymers. Thin films of PR polymers have the advantage of being scalable to large area and can be produced at low cost. A new method based on recording fringe patterns

on to an array of holographic elements referred to as “hogel” has been developed by the MIT Media Lab.⁴⁰ Each hogel is a small piece of the hologram and possesses a homogeneous spectrum (distribution of spatial frequencies). This approach opens a direction towards producing fixed or rewriteable large-area 3D displays. Besides the computation and experimentation challenges involved in bringing realistic 3D images to viewers, the recording material has its own issues. Efficient rewriteable materials with high spatial frequency resolving power are required.

Many types of materials other than classic photographic emulsions have been developed to record images in 3D. Depending on the material, the holographic information is recorded as either an amplitude or a phase grating. Amplitude holograms have lower diffraction efficiencies than phase holograms and are therefore used rarely. Most materials used for phase holograms reach the theoretical diffraction efficiency for holograms, which is 100% for thick holograms (Bragg) and 34% for thin holograms (Raman-Nath). Depending on the type of material used, some post-write processing might be necessary. Table 1 summarizes the materials used for holographic recording. The resolution limit given in the table indicates the maximum number of interference lines per mm of grating. Among many recording materials, polymers have distinctive features such as excellent diffraction efficiency and high resolution. They can be mass produced at low-cost, they are flexible and large-area devices can be readily made with polymers. Permanent 3D images can be recorded in photopolymers; however the film is cured by exposure to light and cannot be written into again. Organic PR materials, on the

other hand, are rewriteable media and there's no post-processing involved after the recording of holograms.

Material	Reusable	Processing	Type of hologram	Max. efficiency	Required exp. [mJ/cm ²]	Resolution limit [mm ⁻¹]
Photographic emulsions	No	Wet	Amplitude	6%	0.001–0.1	1,000–10,000
			Phase (bleached)	60%		
Dichromated gelatin	No	Wet	Phase	100%	10	10,000
Photoresists	No	Wet	Phase	33%	10	3,000
Photothermoplastics	Yes	Charge and heat	Phase	33%	0.01	500–1,200
Photopolymers	No	Post exposure	Phase	100%	1–1,000	2,000–5,000
Photochromics	Yes	None	Amplitude	2%	10–100	>5,000
Photorefractives	Yes	None	Phase	100%	0.1–50,000	2,000–10,000

Table 1-1: General properties of recording materials used in holography⁴¹

PR polymers offer an efficient, dense, rewriteable media without any need for post processing. When high quality images are recorded with high resolution into an array of holographic elements through a scanning head, mechanical vibrations that exist in the environment will be a critical limitation. In order to avoid vibrations, recording with nanosecond (ns) pulses is necessary. Ns pulses will freeze out mechanical vibrations and prevent washout of the interference fringes. Therefore, PR polymers sensitive to single-pulse exposure and having long persistence are critical for the demonstration of a practical rewriteable 3D display.

The combination of a hogel-based recording scheme and real-time high-performance photorefractive polymers will enable 3D rewriteable displays.

1.3 Organization of the Present Work

The information provided in Chapters 2 and 3 is intended to supplement the necessary background for understanding the results discussed in Chapter 5. The details of experimental techniques used are discussed in Chapter 4. A general description of the photorefractive effect and in particular the latest physical models developed for understanding the PR effect in polymer composites are included in Chapter 2. A description of key material components necessary for state-of-art operation and a summary of other material approaches will be provided in Chapter 3. Chapter 4 summarizes the experimental techniques used to probe photorefractive materials. Some of these techniques are used to probe subprocesses leading to the overall PR effect.

The work presented in Chapter 5 provides key solutions to several of the limitations existing photorefractive polymers: (1) provide alternative material and device approaches to reduce the bias voltage while maintaining the high performance, (2) extend the sensitivity of PR materials into the near-infrared and provide high performance operation at two particular wavelengths: 845nm and 975nm, (3) improve the dynamics of the PR material even further to achieve submillisecond response times using single-pulse exposure, (4) increase the decay time through copolymer-based photoconductors and thermal fixing, (5) understand the behavior of low- T_g PR polymers in reflection geometry and optimize it for holographic display applications.

2 FUNDAMENTALS OF PHOTOREFRACTIVITY

A photorefractive (PR) material records a replica of the light distribution in terms of index-modulated phase gratings, also referred as photo-induced refractive index change in the material. PR materials possess two important properties; they are photoconductive and they exhibit the electro-optic effect. Unlike other physical processes that generate a phase grating, the PR effect is fully reversible and has a nonlocal aspect. The recorded holograms can be erased with a spatially uniform light beam. The nonlocal aspect of the PR effect arises from the physical motion of charges in the material. An important consequence of this phase shift is energy transfer between two light beams interfering in a PR medium, known as asymmetric two-beam coupling.

The mechanism that leads to the formation of index modulation involves the build-up of space-charge field through absorption of light, generation of carriers, their transport and trapping over macroscopic distances. The resulting electric field between positive and negative charges produces a refractive index change through orientational (birefringence) and nonlinear optical effects. Particularly in a common guest-host PR polymer, a hole is created by photoexcitation of a sensitizer molecule and subsequently it is transported by hopping between charge transport agent (CTA) molecules until it falls in a trap while electron stays intact. An external field is required to facilitate this process. The nonlinear optical (NLO) chromophore provides the necessary electro-optic response and birefringence.

Due to both the derivative factor in Poisson's equation ($\pi/2$ phase shift) and the spatial transport of charges, the index modulation distribution has a phase shift ($< \pi/2$)

with respect to the periodic light distribution produced by two interfering writing beams. This phase shift enables coherent energy transfer between two beams propagating in a thick PR film. This property, referred to as two-beam coupling, is used to build amplifiers.

When two coherent beams interfere, the light pattern will be a spatially modulated intensity distribution $I(x)$ which is given by:

$$I = I_0[1 + m \cos(2\pi x / \Lambda)] \quad (1)$$

where $I_0 = I_1 + I_2$ is the total incident intensity, i.e., the sum of the intensities of the two beams; $m = 2\sqrt{I_1 I_2} / (I_1 + I_2)$, the fringe visibility and Λ , the spatial wavelength or periodicity. In the standard slanted transmission geometry (see section 2.6.1) the grating spacing can be expressed as:

$$\Lambda = \frac{\lambda}{2n \sin[(\alpha_2 - \alpha_1) / 2]} \quad (2)$$

where n is refractive index of the polymer film, λ the optical wavelength in vacuum, and α_1 and α_2 the internal angles (inside the material) of the two writing beams relative to the sample normal. Λ gives the period of the sinusoidal light distribution which can be very short in the reflection geometry (0.15-0.3 μm) and an order longer in the transmission geometry (1-20 μm) when visible optical wavelengths are employed.

The four major steps leading to the formation of a PR phase grating are shown in Figure 2-1. These steps are (1) absorption of light and generation of charge carriers; (2) transport through diffusion and drift of charge carriers (either electrons or holes

depending on the transport matrix) over a fraction of grating spacing leading to separation of electrons and holes; (3) trapping of these charge carriers and the build-up of a space-charge field; (4) and modulation of the refractive index by the periodic space-charge field.

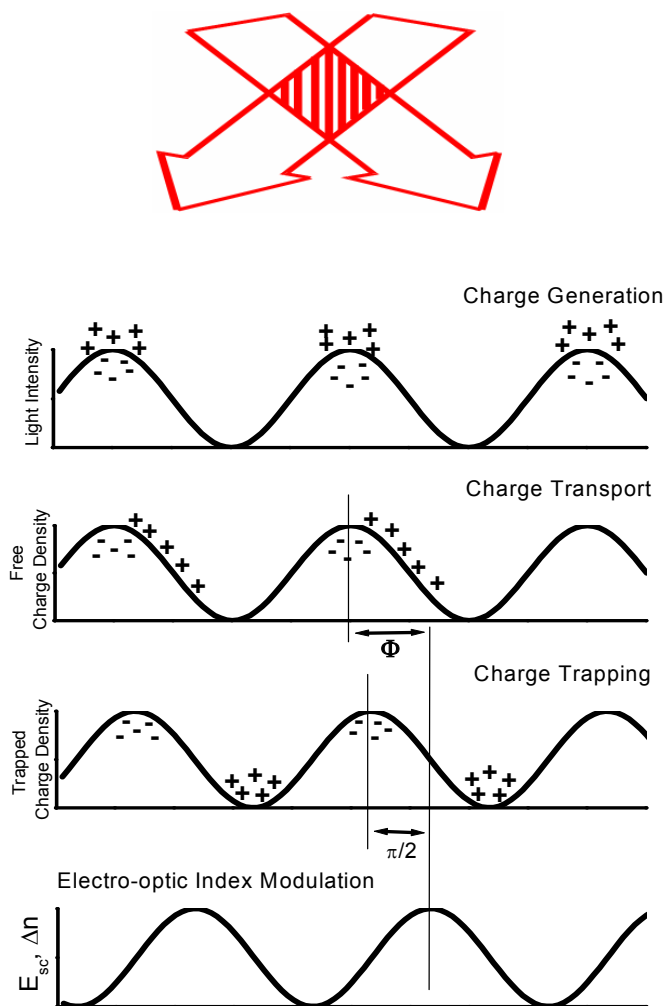


Figure 2-1: Schematic representation of the photorefractive effect in the case of a sinusoidal light pattern. A replica of the light pattern in terms of spatial refractive

index variation (phase grating) is obtained. Notice that the phase grating is phase shifted compared to the light grating.

We will now present the physical models currently used to describe charge generation, transport, trapping and build-up of space-charge field in amorphous organic photoconductors and discuss the physics of polymers doped with nonlinear optical chromophores. Later on in this section, the diffraction theory of thick holograms and two-beam coupling will be presented.

2.1 Photogeneration

The PR effect is initiated with the absorption of light and creation of charge carriers. Upon light illumination, first a correlated electron-hole pair is created, later this pair separate with the help of diffusion or drift in the case of an electric field. The photogeneration efficiency in organic materials is strongly field-dependent.

To understand photogeneration in organic materials, one should understand the electronic band structure in these materials. As in semiconductors, there are two major energy levels. However, unlike semiconductors, each molecule has its own independent energy levels. The charge is generated through excitation from the highest occupied molecular orbital (HOMO) into the lowest unoccupied molecular orbital (LUMO). The ionization potential (I_p) defines the level of the HOMO and is referred to the amount of energy required to remove the loosely bound electron. To define the LUMO level, one can talk about electron affinity (EA) which is the energy involved as an electron is added to the molecule (see Figure 2-2).

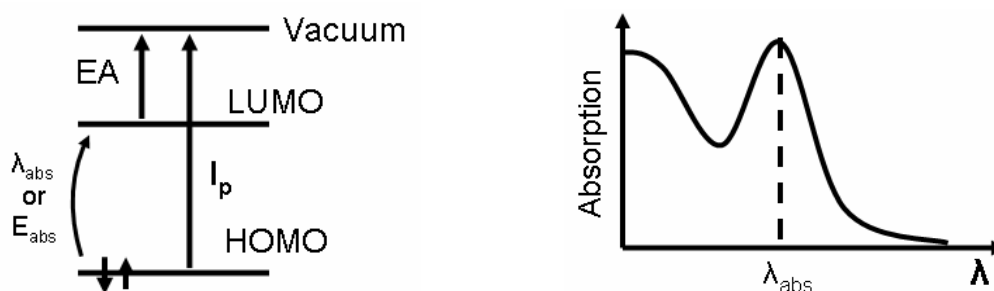


Figure 2-2: Schematic diagram of energy levels in a molecule. The first absorption (lowest energy) peak occurs when an electron is excited from the HOMO level to the LUMO.

The quantum efficiency is a quantity defined as the percentage of photons hitting a photosensitive material that will produce an electron-hole pair. The key step in photogeneration is the charge transfer reaction between the excited sensitizer molecule A^* (acceptor) and the transport molecule D (donor) (see Figure 2-3). The ionization potential of the charge generator should be larger than that of the transport matrix for best charge generation.

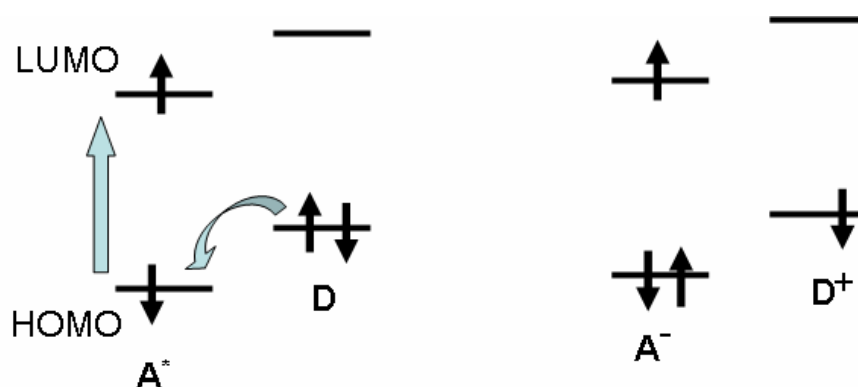


Figure 2-3: The photogeneration process in organic photoconductors

The theory developed by Onsager^{42,43} for the dissociation of ionic pairs in weak electrolytes under applied fields has been found to describe reasonably well the

temperature and electric field dependence of the photogeneration efficiency in some of the photoconductors.⁴⁴

Onsager Model:

This model assumes the formation of an uncorrelated electron-hole pair (or exciton) followed by the formation of an intermediate charge-transfer state in which the electron and the hole are thermalized and separated by an average distance of r_0 . Then, one of the carriers can escape from its twin with a given probability if that distance is comparable to or higher than the so-called Coulomb radius given by:

$$r_c = e^2 / 4\pi\epsilon_0\epsilon k_B T \quad (3)$$

where e is the elementary charge and ϵ the relative dielectric constant. In this model, the photogeneration efficiency can be expressed as:

$$\phi(E) = \phi_0 \left[1 - \zeta^{-1} \sum_{n=0}^{\infty} A_n(\kappa) A_n(\zeta) \right] \quad (4)$$

where $A_n(x)$ is a recursive formula given by:

$$A_n(x) = A_{n-1}(x) - \frac{x^n \exp(-x)}{n!} \quad (5)$$

and

$$A_0(x) = 1 - \exp(-x) \quad (6)$$

here, $\zeta = er_0 E / k_B T$ and $\kappa = r_c / r_0$.

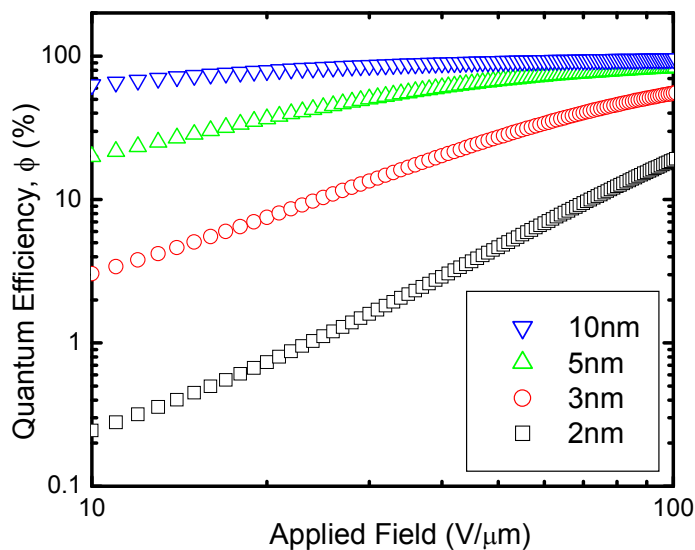


Figure 2-4: Onsager curves for the field dependence of the quantum efficiency over a range of thermalization radii, r_0 ($T=300\text{K}$, $\varepsilon = 3.5$).

The values of the thermalization radius that are used in order to get the best fit to the experimental data (see Figure 2-4) are often too high to have real physical meaning. Therefore, Onsager's theory offers only a qualitative framework to describe the field dependence of photogeneration in organic photoconductors.

Charge-transfer (CT) complexes for photogeneration:

The intermolecular interaction between the donor D and the acceptor A can lead to a new absorption band that does not appear in the spectrum of either component alone (see Figure 2-5). Hence, spectral sensitivity in the visible and the near infrared part of the spectrum can be achieved with CT complexes. Many of the near-infrared absorption in recent PR polymers based on the PVK matrix is achieved this way. For example the

interaction between PVK polymer and TNFM molecule creates absorption with a tail extending all the way up to 900nm.⁴⁵ Good photoreceptors (acceptors) are good CT complexes. The choice of a sensitizer is often dictated by the transport molecule and the best performance is obtained by optimizing the charge-transfer properties between a given sensitizer and its parent transport molecule.

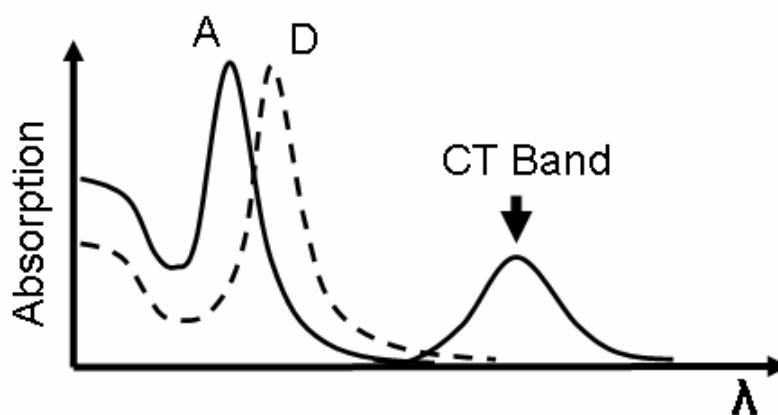


Figure 2-5: Typical absorption band in a charge-transfer (CT) complex. Note that there is an additional absorption at longer wavelengths.

Photogeneration efficiency is commonly measured using a xerographic discharge technique^{46,47} or estimated from the dc photoconductivity.⁴⁸

2.2 Transport and Trapping

In amorphous systems like organic polymeric composites, the charge carrier moves through successive hopping between the molecules. Unlike crystalline materials where charge moves in highly delocalized bands, the transport mechanism in amorphous materials requires a different mechanism and description. In molecularly doped polymers,

organic glasses, or polymers with charge transport moieties as side chains, hopping occurs between charge transporting molecular sites, and disorder is due to impurities, different conformational orders, site energy distribution, etc. of the charge transporting molecules. In conjugated polymers, hopping proceeds through the conjugated parts of the polymer chain, and the disorder is due to impurities, kinks, and cross-links in the conjugated path.⁴⁹ The presence of high concentration of trapping sites leads to charge transport characterized by trapping and detrapping events that closely resemble a charge hopping. Bassler and coworkers⁵⁰ have developed a disorder formalism for organic amorphous materials which is widely used in the current organic PR materials. In amorphous systems, every transport event between two molecules must be considered as a discrete event. In other words each hop is an independent event.

The hopping process can be characterized by an electron-transfer function between two nearby molecules. It is generally field assisted and thermally activated. In organic materials, electron transport occurs among the LUMO, whereas hole transport takes place in the HOMO. Depending on the nature of the polymer, the transport system can be unipolar (either hole or electron transport) or bipolar (both electron and hole transport). Most of the photoconductors used in organic PR composites are unipolar so that a nonuniform space-charge distribution can be obtained.

The empirical form for the field and temperature dependence of the mobility was developed by Poole-Frenkel⁵¹ which is given in the form as below,

$$\mu \propto \exp \left[-\frac{(\Delta - \beta\sqrt{E})}{k_B T_m} \right] \quad (7)$$

where Δ is the activation energy, β and T_m are constants determined experimentally. This relationship remains an important empirical function for experimental data fitting and provides building blocks for other models that utilize mobility as part of the process, such as the PR model developed by Schildkraut and coworkers.⁵² However, the Poole-Frenkel model is based on physically unrealistic assumptions that require Coulomb traps at each hopping site.

The disorder formalism considers that the lack of long-range order creates a manifold of localized states with superimposed energetical and positional disorder. The energy distribution of hopping sites is assumed to follow a Gaussian distribution with standard deviation σ (see Figure 2-6). Positional disorder is assumed to result from local variations of distances between hopping sites which is randomly distributed over the space and is described by Σ . This model also assumes that the phase is lost after consecutive hopping events. Therefore, each hopping event is considered as statistically independent.

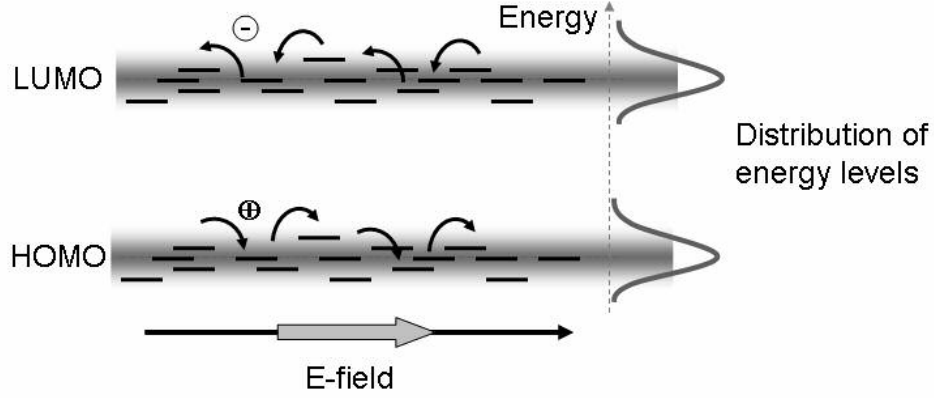


Figure 2-6: In disorder formalism, the energy distribution of hopping sites is assumed to have a Gaussian distribution.

The disorder formalism is based on the argument that charge transport occurs by activated hopping with asymmetric Miller-Abrahams⁵³ probability. In Miller-Abrahams form, the hopping rate ν_{ij} between two sites with energies ε_i and ε_j is,

$$\nu_{ij} = \nu_0 \exp(-2\gamma\Delta R_{ij}) \begin{cases} \exp\left[-\frac{\varepsilon_j - \varepsilon_i}{k_B T}\right] & ; \varepsilon_j > \varepsilon_i, \\ 1 & ; \varepsilon_j < \varepsilon_i \end{cases} \quad (8)$$

where ν_0 is a frequency prefactor, γ the inverse decay constant and ΔR_{ij} the distance between the two sites. The first exponential stands for the wave function overlap between two sites, and the bracketed portion describes the thermally activated hopping probability. A charge hopping from high to low energy sites is not restricted by any condition and such downward jump is not affected by the presence of electric field. Therefore, effects arising from strong charge-phonon coupling are neglected.

In disorder formalism, the charge carrier mobility at moderate field strengths is described by the following expression:

$$\mu = \mu_0 \exp \left\{ \left[C (\sigma / k_B T)^2 - \Sigma^2 \right] \sqrt{E} - (2\sigma / 3k_B T)^2 \right\} \quad (9)$$

where μ_0 is a pre-factor and C a constant given by $2.9 \times 10^{-4} (cm/V)^{1/2}$. The key parameters of the formalism are the diagonal energetic disorder parameter (σ) and the off-diagonal positional parameter (Σ). The mobility is typically an increasing function of electric field and temperature. The disorder formalism seems to model reasonably well for a majority of the photoconductors used in current PR materials. However, recent experimental observations of a decrease in mobility with the increasing electric field prompted a reexamination of the assumptions of the disorder formalism and, in particular, the treatment of hopping using Marcus electron-transfer rates⁵⁴ instead of Miller-Abrahams rates.⁵⁵

Marcus theory⁵⁴ makes several predictions concerning electron-transfer between donor and acceptor molecules. The so-called reorganizational energy λ , is defined as the energy required to optically excite an electron from an electron donor to an acceptor. The rate of electron transfer will exponentially increase as a function of the energy difference (non-inverted regime) up to a point. When the energy difference becomes too large the electron transfer rate will decrease (inverted regime). The electron-transfer rate is quantified in the form below:

$$k = k_0 \exp(-\beta \Delta R) \exp\left[-\frac{(\lambda - \Delta E)^2}{4k_B T \lambda}\right] \quad (10)$$

where k_0 is pre-exponential factor, β the constant for positional dependence, ΔR the distance between hopping sites, λ the reorganization energy, ΔE the energy difference between hopping states and $k_B T$ the thermal energy. The first part states that, the transfer rate will decrease as the distance between donor molecules is increased, similar to Miller-Abraham form. The transfer rate will increase exponentially as the energy difference goes up until reaching the reorganizational energy and will decrease as the energy gap increases further (in the inverted regime) (see Figure 2-7).

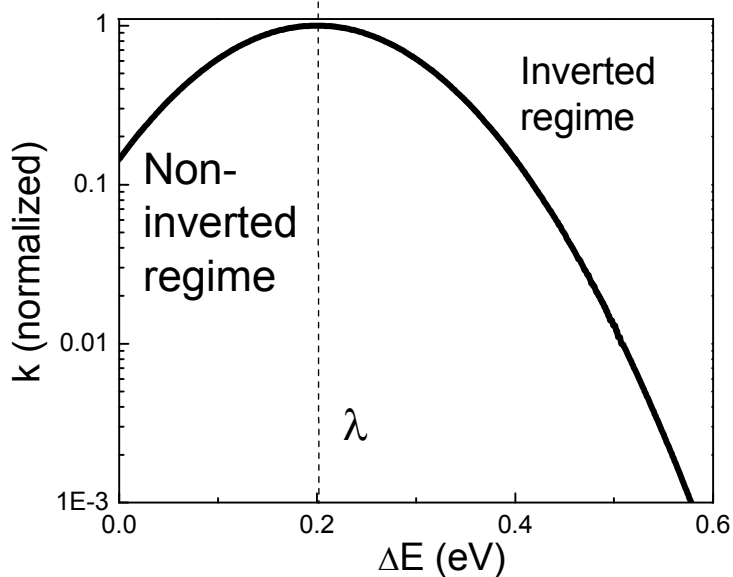


Figure 2-7: The behavior of the electron-transfer rate predicted by Marcus theory. Notice the unusual behavior in the inverted regime. λ is the reorganization energy.

In the work of Hendrickx and coworkers⁵⁵, a series of hole-transport molecules with different ionization (I_p) potentials were doped with C_{60} sensitizer. Light absorption was due to the charge-transfer complex formed between the hole-transport molecules and sensitizer (see Figure 2-8). The rate of electron transfer was observed to increase exponentially with increasing enthalpy of complexation (ΔH_c) or decreasing donor I_p . Unlike a transfer rate of unity according to the Miller-Abraham form; this experimental observation follows an exponential electron-transfer rate predicted by Marcus theory in the non-inverted regime.

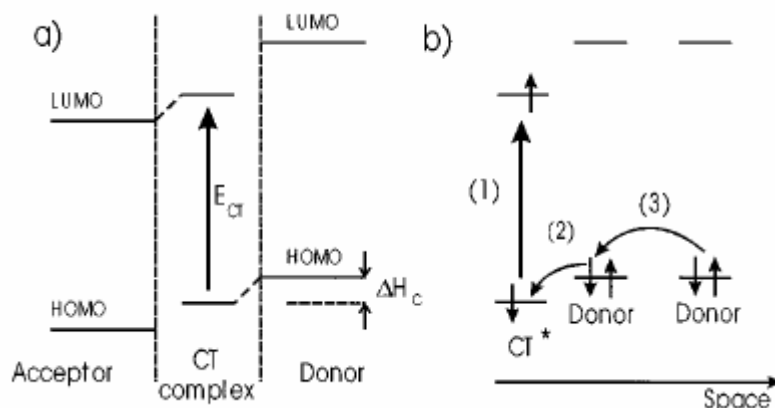


Figure 2-8: (a) Energy levels for acceptor and donor molecules as well as the charge-transfer complex (b) The processes involved as a photon is absorbed in the system.

In PR polymer composites, generally, mobility decreases as the dipole moment of a host or a dopant increases due to dipole-dipole interactions affecting energetic disorder^{56,57} and mobility increases as a function of concentration of the charge transport moiety.⁵⁸ If the I_p of the dopant is close to that of the main transport molecule, the

dopants can participate in transport and either increase or decrease mobility. The dopants may act as a traps. Therefore the relative I_p of each element in the composite will affect transport properties.

Mobility Measurements:

Charge carrier mobility can be measured by time-of-flight (TOF),⁵⁹ holographic time-of-flight (HTOF)⁶⁰ and estimated from the dc photoconductivity.⁶¹ In the TOF case, a short pulse (ns or μ s) is absorbed through a thin layer of material and the pulse train of charges is monitored through the flow of current. A composite with many traps gives a dispersive response curve, on the other hand when there are few traps the response is non-dispersive (ballistic mobility).

Trapping Sites:

A trapping site is a local region of the material where the mobile charge is prevented from participating in transport for some period of time. For example, in a hopping picture, a site with lower total energy for the hole may act as a trap, and the lifetime of the carrier in the trap will be determined by the trap depth compared to thermal energy. When long lifetimes of gratings are desired, the relative energy levels have to be considered. In a hole-transport matrix, the traps can be either shallow (charge can be easily detrapped both optically and thermally) and deep (a detrapping rate of at least one order of magnitude less than a shallow trap).

Trapping and recombination properties of PR composites have been extensively studied over the past few years.⁶² In particular, infrared optical spectroscopy⁶³ was employed to probe the PR trap density, while various modifications of dc

photoconductivity measurements proved to be effective in studies of trapping, detrapping, and recombination parameters.

Most photoconductors currently used in PR composites are donor-like molecules.

A typical diagram for charge transfer and trapping is depicted in the Figure 2-9.

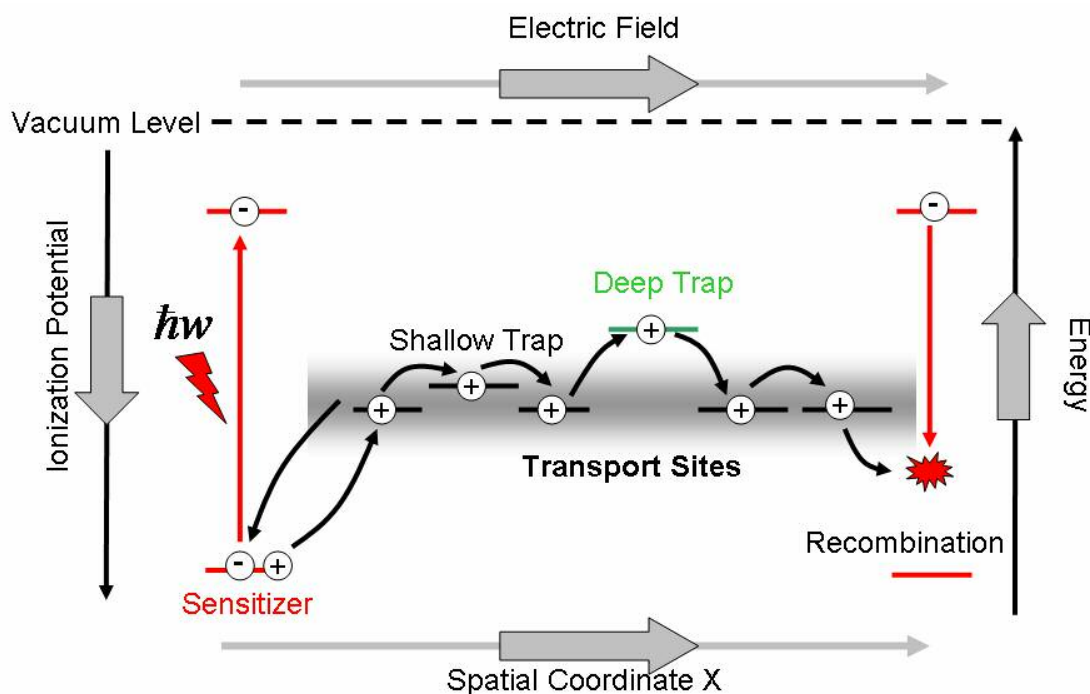


Figure 2-9: Schematic representation of the charge generation, transport, trapping and recombination in organic photorefractive materials. Note that transport is through hopping from one molecule to another or through conjugated side-chains of the polymer matrix.

2.3 Build-up of Space-charge Field

The theoretical description of the space-charge field was first developed by Kukhtarev⁶⁴ for inorganic crystals through the solution of a set of rate equations. Briefly,

these charge density rate equations for density of charges contain terms for generation, diffusion, drift and recombination. To develop a better model for organic materials, Schildkraut et al⁵² included the rate equation for trap density and took into account the field dependence of both photogeneration efficiency and carrier mobility. The PR model was further developed by Ostroverkhova et al⁶² who introduced in the model two kinds of traps: shallow and deep. In the latest study,⁶² the term "deep" meant that the rate of thermal detrapping for these traps was at least an order of magnitude smaller than that of the shallow traps, but still having a nonzero probability for detrapping.

Here, we will begin with the theory that's widely used to describe the PR effect in both inorganic and organic materials.

2.3.1 *Kuktharev Model*

The Kuktharev model describes the equilibrium space-charge field by solving a set of rate equations for the standard band transport model developed for inorganic crystals.⁶⁴ It gives the first-order component of the steady-state space-charge field created by a sinusoidal light distribution. The results are applicable to organic materials as well. An extension of this model for polymers is discussed in the next section.

The amplitude of the space charge field (E_{sc}) based on Kuktharev model is given by:

$$E_{SC} = m \left(\frac{(E_0^2 + E_D^2)}{(1 + E_D/E_q)^2 + (E_0/E_q)^2} \right)^{1/2} \quad (11)$$

where m is the fringe visibility and E_0 the component of the applied field along the grating wave vector. The diffusion field, E_D , is defined as:

$$E_D = \frac{Kk_B T}{e} \quad (12)$$

where $K = 2\pi/\Lambda$ is the magnitude of the grating wave vector, k_B is the Boltzmann constant, T the temperature and e the elementary charge. The trap limited field E_q is given by:

$$E_q = \frac{eN_{eff}}{K\varepsilon\varepsilon_0} \quad (13)$$

where ε is the dielectric constant, ε_0 the permittivity constant and N_{eff} the effective density of traps.

The phase shift Θ between the space charge field and the light intensity pattern is given by:

$$\Theta = \arctan \left[\frac{E_D}{E_0} \left(1 + \frac{E_D}{E_q} + \frac{E_0^2}{E_D E_q} \right) \right] \quad (14)$$

If transport takes place only by diffusion, the phase shift is $\pi/2$, otherwise it depends on the relative strength of the diffusion and drift processes.

Calculated values of amplitude and phase of the space-charge field as a function of applied field are shown in the Figure 2-10 for different values of the trap density N_{eff} .

In the trap limited regime, when the density of traps is small, the space-charge field

reaches a constant value. When the trap density is large, the space charge field increases linearly with external applied field. Figure 2-10 (b) shows how the applied field affects the phase shift at various trap densities.

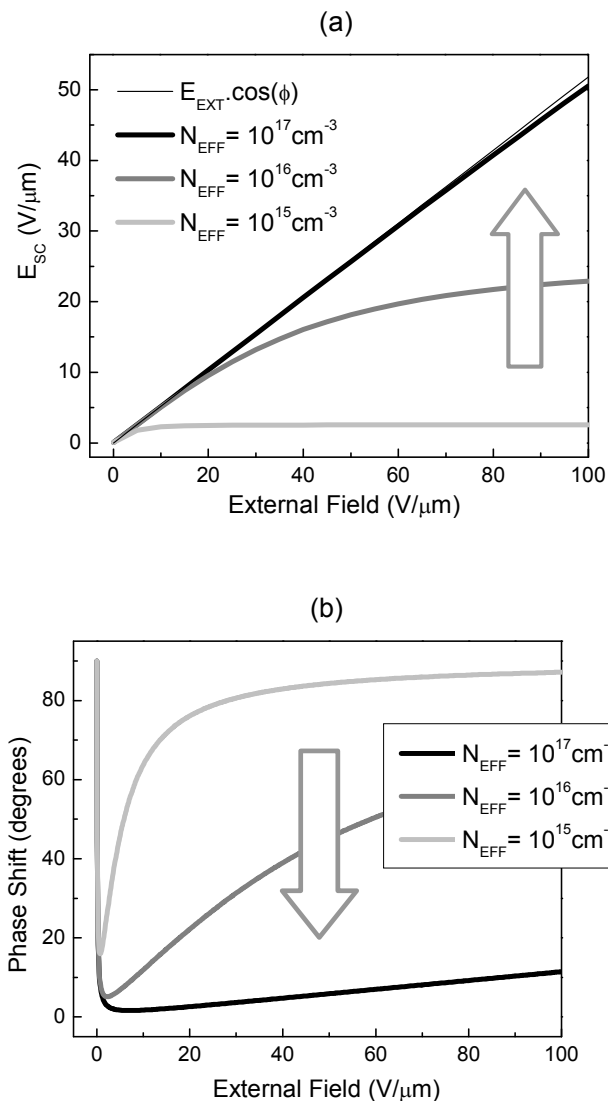


Figure 2-10: The amplitude (a) and phase (b) of the space-charge field as a function of applied field.

2.3.2 Model for Polymers

The mechanism leading to space charge field formation in polymers can also be explained through Kukharev theory; however, major differences do exist.^{65,66,67,68} In polymers, both photogeneration efficiency and carrier mobility are highly field dependent.⁵²

Schildkraut and coworkers⁵² have developed analytic expressions for zero-order and first-order Fourier components of the charge density and the space-charge field in photoconducting polymers. The empirical field dependence of the quantum efficiency of hole-conducting polymers is considered as:

$$\phi(E) \propto s(E) \propto E^p ; \quad s(E) = s_0 (E / E_0)^p \quad (15)$$

where E is the local field, E_0 the value of the projection of applied field in the direction of grating vector and p is a numeric exponent that can be determined experimentally.

The hole mobility μ is modeled as,

$$\mu(E) = \mu_0 \exp \left[C \left((E/E_0)^{1/2} - 1 \right) \right] \quad (16)$$

where C is an experimentally determined constant and μ_0 the value of the mobility at the field E_0 .

According to the Langevin theory,⁶⁹ the recombination and trapping rates are field dependent because they are proportional to the charge carrier's mobility:

$$\gamma_R(E) = \gamma_T(E) = \frac{e\mu(E)}{\varepsilon_{eff}\varepsilon_0} \quad (17)$$

where ε is the dielectric constant and ε_0 the permittivity constant. The steady-state space-charge field amplitude is

$$E_{SC} = A \frac{imE_q(E_D + iE_0)}{B_1 + B_2} \quad (18)$$

E_D is the diffusion field defined above. Under the further assumption that the average hole density is small compared with the total concentrations of generator (N_G) and trapping molecules (N_T), other quantities appearing in Equation (18) are as follows:

$$A = \frac{s_0 I_0 + \gamma_T N_T}{\gamma_T N_T} \quad (19)$$

is a dimensionless factor, and

$$E_q = \frac{e}{\varepsilon_{eff}\varepsilon_0 K} \frac{\gamma_T N_T (N_G - N_T)}{s_0 I_0 + (e\mu_0 N_G / \varepsilon_{eff}\varepsilon_0)} \equiv \frac{e}{\varepsilon_{eff}\varepsilon_0 K} N_{eff} \quad (20)$$

which is similar to the trap-limited field in Kukharev model, but depends also on the light intensity and on the mobility (due to Langevin recombination). B_1 and B_2 are,

$$B_1 = E_D + (1 + Ap)E_q + \left[1 + \frac{1}{2}C \left(E_D \frac{E_0}{E_{ref}} \right)^{1/2} \right] E_I \quad (21)$$

$$B_2 = E_0 + \frac{E_D E_q}{E_0} \left[\frac{1}{2}C \left(\frac{E_0}{E_{ref}} \right)^{1/2} - Ap \right] \quad (22)$$

where E_{ref} is a reference value of the applied field for which the constant C is determined. Finally, E_I is,

$$E_I = \frac{s_0 I_0}{s_0 I_0 + \gamma_T N_T} \frac{e}{\epsilon_{eff} \epsilon_0 K} (N_G - N_T) \quad (23)$$

In Figure 2-11, we plot the field dependence of the real and imaginary components of the space-charge field. The curves are obtained using the parameters $\Lambda = 3.1 \mu m$, $E_{ref} = 1V / \mu m$, $s(E_{ref}) = 1 cm^2 / Ws$, $p = 1$, $I_0 = 1W / cm^2$, $\mu(E_{ref}) = 10^{-7} cm^2 / Vs$, $C = 3$, $\epsilon_{eff} = 3.5$, $N_G = 5 \times 10^{15} cm^{-3}$, $N_T = 10^{16} cm^{-3}$, $T = 295K$ and projection angle $\phi = 60 \text{ deg}$. $\text{Im}(E_{SC})$ is responsible for the energy transfer between the beams in TBC experiment. $\text{Im}(E_{SC})$ can become dominant if the applied field is large.

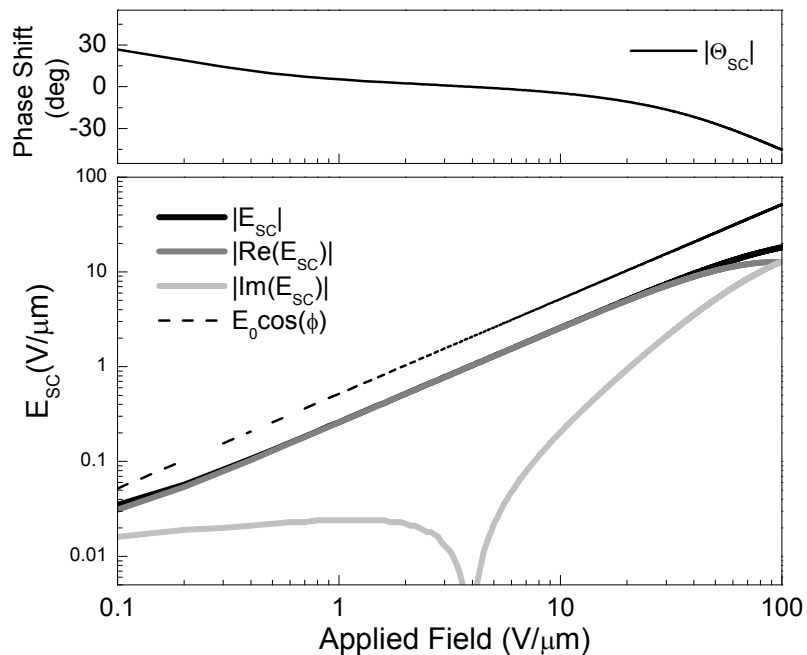


Figure 2-11: The phase and amplitude of the space-charge field as a function of applied field in the case of polymers.

Any model describing the formation of PR gratings in polymers may need a large number of parameters and maybe valid only in certain limiting situations. Therefore, most researchers in polymeric PR materials use the conventional Kuktharev model⁶⁴ to explain their results. However it's evident that more theoretical and experimental work is needed in order to establish a generally recognized theory for space-charge formation in polymers.

2.4 Physics of Poled Polymers

Relating macroscopic properties of PR polymers to the individual molecular properties and establishing a structure-property relationship has been very challenging and is subject to intensive research. The recent advances especially in the electro-optic polymers have been possible through simultaneous improvement of the magnitude of nonlinearity at molecular level and through a better understanding of intermolecular interactions between molecules in the polymer matrix. The oriented gas model has proven to be a good approximation to describe the linear and second-order nonlinear optical properties of poled polymers.⁷⁰ PR polymers are doped with nonlinear optical (NLO), intramolecular charge-transfer molecules referred to as chromophores. Charge-transfer molecules, in other words push-pull molecules, consist of an electron-accepting group (A) connected to an electron-donating group (D) through a π -conjugated bridge (see Figure 2-12). These molecules have a strong permanent dipole moment and are highly polarizable. External electric fields can orient these molecules in one direction. This effect is counteracted by thermal energy and can be hindered by interaction of the molecules with the surrounding host matrix^{71,72} as well as with each others. This asymmetric polarization also provides the potential for strong second order nonlinear optical properties.

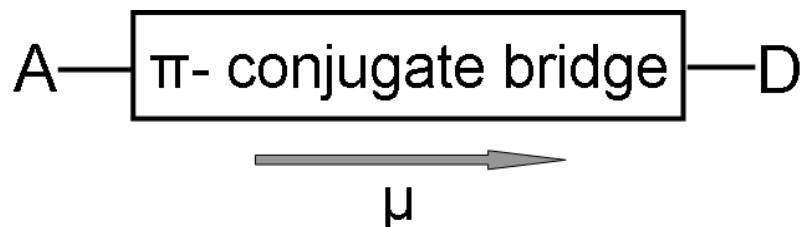


Figure 2-12: Schematic of push-pull molecules (chromophores) for electro-optic and photorefractive applications.

The second-order nonlinear susceptibility $\chi^{(2)}$, can only exist in non-centrosymmetric materials (materials that do not possess an inversion symmetry). On the other hand, all materials including amorphous polymers can exhibit a non-vanishing third-order nonlinear susceptibility $\chi^{(3)}$. In centrosymmetric materials, the polarization induced by two electric fields pointing in opposite directions are equal in amplitude but have opposite sign ($P(-E) = -P(E)$). One can easily demonstrate that in this case the constant in front of the quadratic nonlinear term must be zero ($\chi^{(2)} = 0$). Noncentrosymmetry is a necessary condition for electro-optic and PR materials which are based on second-order nonlinear processes. A polymer matrix doped with polar molecules can be made non-centrosymmetric through the application of a bias field above the glass transition temperature (T_g) of the material (see Figure 2-13). The system is simply heated above T_g and a bias field is applied, the polar molecules will orient to the bias and the system is cooled down to room temperature with the bias field maintained. In this way a net orientation of molecules in the film is achieved; they are “frozen” in place according to the laws of statistical mechanics. In this case, the decomposition temperature

of the poled molecule (or dye) needs to be more than the T_g . If the molecules are aligned along a preferred direction, the medium will be optically anisotropic. But in addition to being anisotropic, the molecules should all point in the same direction, i.e. the dipoles should be aligned.

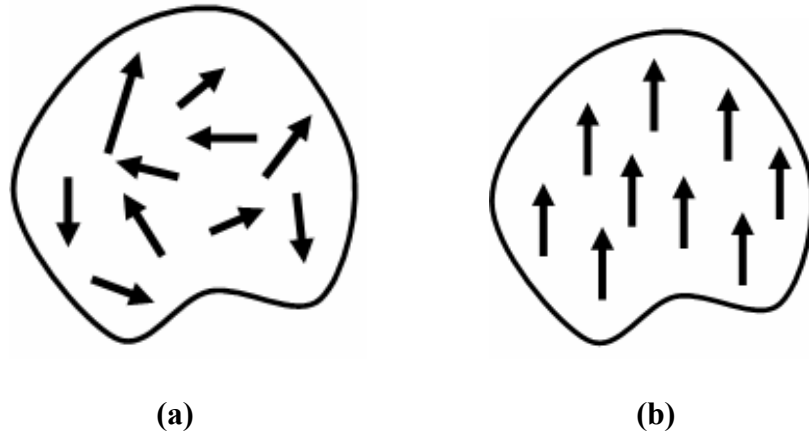


Figure 2-13: Random dipole orientation in the cases of no field (isotropic) (a) and with field (non-centrosymmetric) (b). Note that, in isotropic and amorphous systems $\chi^{(2)} = 0$.

By analogy with macroscopic systems, molecules exhibit second-order nonlinearities only if centrosymmetry is broken. The microscopic molecular polarization components of a molecule for a nonresonant excitation can be written as:

$$p_i = \mu_i + \sum_j \alpha_{ij} E_j + R^{(2)} \sum_{jk} \beta_{ijk} E_j E_k + R^{(3)} \sum_{jkl} \gamma_{ijkl} E_j E_k E_l + \dots \quad (24)$$

where α_{ij} , β_{ijk} , γ_{ijkl} are tensor elements and E_j, E_k, E_l are components of the electric field at the molecule. The subscripts i, j, k and l refer to Cartesian coordinates expressed in the molecular frame. $R^{(n)}$ are degeneracy factors that depend on the

nonlinear process and the frequencies of the electric fields involved in the interaction. μ_i is the ground-state dipole moment of the molecule. The linear polarizability is given by the tensor $\tilde{\alpha}$. The microscopic equivalent of the macroscopic susceptibility $\tilde{\chi}^{(2)}$ is described by $\tilde{\beta}$ and is called the *first hyperpolarizability*. Similarly, $\tilde{\gamma}$ is the second hyperpolarizability and is the molecular equivalent of the macroscopic susceptibility $\tilde{\chi}^{(3)}$.

On a macroscopic level in the frame (X, Y, Z) of the laboratory, the nonlinear polarization induced in the polymer can be described as:

$$P_I = \chi_{IJ}^{(1)} E_J + R^{(2)} \chi_{IJK}^{(2)} E_J E_K + R^{(3)} \chi_{IJKL}^{(3)} E_J E_K E_L + \dots \quad (25)$$

where I, J, K and L refer to components expressed in the lab frame.

The oriented gas model⁷⁰ can predict macroscopic nonlinear properties from the orientational distribution of molecules for a given field, density of molecules and their microscopic nonlinear optical properties. Cylindrical symmetry around the main z axis of the molecule is assumed for simplicity and chromophores can be considered as rodlike molecules (see Figure 2-14). The degree of orientation can be simply described by assuming a statistical Boltzmann distribution of molecules.

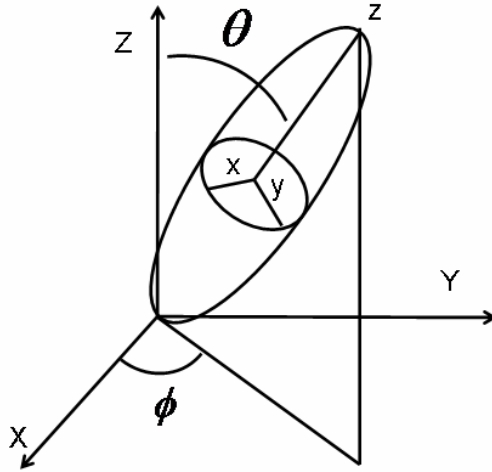


Figure 2-14: Schematic of an individual rodlike molecule in the laboratory frame $\{X, Y, Z\}$ when an electric field is applied along the Z axis. $\{x, y, z\}$ is the frame attached to the molecule.

The normalized orientational distribution function $G(\varphi, \theta, \psi)$ (φ, θ and ψ are Euler angles) is approximated to be a Maxwell-Boltzmann distribution function expressed as:

$$G(\Omega)d\Omega = \frac{\exp\left(-\frac{U(\theta)}{k_B T}\right) \sin \theta d\theta}{\int_0^\pi \exp\left(-\frac{U(\theta)}{k_B T}\right) \sin \theta d\theta} \quad (26)$$

where $U(\theta)$ is the interaction potential energy between the poling field and the dipole moment. This interaction energy is given by:

$$U(\theta) = \mu^* \cdot E_p - \frac{1}{2} p \cdot E_p \approx -x k_B T \cos \theta \quad \text{with } x = \frac{\mu^* \cdot E_p}{k_B T} \quad (27)$$

with μ^* being the modulus of the permanent dipole moment of the chromophore and is corrected for the local field effects of the surrounding matrix and p is the induced dipole moment. E_p is the modulus of the poling field applied along the Z axis of the laboratory frame.

Later in this section, the orientational order can be described by averaged quantities in the form $\langle \cos^n \theta \rangle$ which with these approximations are given by:

$$\langle \cos^n \theta \rangle = \frac{\int_0^\pi \cos^n \theta \exp(x \cos \theta) \sin \theta d\theta}{\int_0^\pi \exp(x \cos \theta) \sin \theta d\theta} = L_n(x) \quad (28)$$

where x is a dimensionless parameter defined in Equation (27) and $L_n(x)$ are Langevin functions of order n . When $x < 1$ (weak poling field limit), the Langevin functions can be approximated to:

$$L_1(x) \approx \frac{x}{3} \quad L_2(x) \approx \frac{1}{3} + \frac{2x^2}{45} \quad L_3(x) \approx \frac{x}{5} \quad (29)$$

2.4.1 First-Order (Linear) Optical Properties

In the molecular principal axes, the polarizability tensor of the rodlike molecule can be written as:

$$\tilde{\alpha} = \begin{pmatrix} \alpha_{xx} & 0 & 0 \\ 0 & \alpha_{yy} & 0 \\ 0 & 0 & \alpha_{zz} \end{pmatrix} = \begin{pmatrix} \alpha_{\perp} & 0 & 0 \\ 0 & \alpha_{\perp} & 0 \\ 0 & 0 & \alpha_{\parallel} \end{pmatrix} \quad (30)$$

where the subscripts \perp and \parallel refer to the direction perpendicular and parallel to the z axis of the molecules. For a poling field applied along the Z axis, the change in refractive index along all three axes between an unpoled and poled film is (in CGS units):

$$\begin{aligned} \Delta n_z^{(1)}(\omega) &= \frac{2\pi N f_{\infty}}{n} (\alpha_{\parallel} - \alpha_{\perp}) \left(\langle \cos^2 \theta \rangle - \frac{1}{3} \right) \\ &= \frac{2\pi}{n} \frac{2}{45} N f_{\infty} (\alpha_{\parallel} - \alpha_{\perp}) \left(\frac{\mu^*}{k_B T} \right)^2 E_p^2 \end{aligned} \quad (31)$$

$$\Delta n_x^{(1)}(\omega) = \Delta n_y^{(1)}(\omega) = -\frac{1}{2} \Delta n_z^{(1)}(\omega) \quad (32)$$

where N is the number of molecules, f_{∞} is a Lorentz-Lorentz type of expression given by $f_{\infty} = (\varepsilon_{\infty} + 2)/3$. Note that, the linear index modulation or birefringence is a quadratic function of the poling field. This expression is useful for predicting the ellipsometric index modulation (birefringence) as will be discussed in Section 5.5.

2.4.2 Second-Order Nonlinear Optical Properties of Poled Polymers

Poled polymers such as PR polymers belong to the ∞mm symmetry group. With this geometry, the second-order susceptibility tensor has only three independent tensor elements which can be further reduced to two independent components when Kleinmann symmetry holds, away from any electronic resonances of the chromophore. The third-rank tensor of the second order susceptibility is:

$$\chi^{(2)} = \begin{pmatrix} 0 & 0 & 0 & 0 & \chi_{31}^{(2)} & 0 \\ 0 & 0 & 0 & \chi_{31}^{(2)} & 0 & 0 \\ \chi_{31}^{(2)} & \chi_{31}^{(2)} & \chi_{33}^{(2)} & 0 & 0 & 0 \end{pmatrix} \quad (33)$$

The tensor elements are written in a contracted way, $I = 1, 2, 3$ and $J = 1, 2, \dots, 6$.

When the poling field is applied along the Z axis, the two independent second-order susceptibility tensor elements become:

$$\chi_{33}^{(2)} = \chi_{ZZZ}^{(2)} = Nf_0 f_\infty f_\infty \beta_{zzz} \langle \cos^3 \theta \rangle = Nf_0 f_\infty f_\infty \beta_{zzz} \frac{\mu^* E_P}{5k_B T} \quad (34)$$

$$\chi_{31}^{(2)} = \chi_{ZXX}^{(2)} = Nf_0 f_\infty f_\infty \beta_{zzz} \left(\langle \cos \theta \rangle - \langle \cos^3 \theta \rangle \right) / 2 = Nf_0 f_\infty f_\infty \beta_{zzz} \frac{\mu^* E_P}{15k_B T} \quad (35)$$

where, it's assumed that the only nonvanishing component of β_{ijk} is β_{zzz} , the component along the z axis of the molecule. This approximation is valid for rod-like molecules that have cylindrical symmetry. For the dc or low-frequency field, the local field factor can be approximated by the Onsager expression:

$$f_0 = \frac{\varepsilon(\varepsilon_\infty + 2)}{(2\varepsilon + \varepsilon_\infty)} \quad (36)$$

f_∞ is a Lorentz-Lorenz type of expression given by $f_\infty = (\varepsilon_\infty + 2)/3$.

The first hyperpolarizability factor, β :

To predict the nonlinear optical properties of push-pull molecules a simple two-level model is proposed.⁷³ In the two-level model, the intramolecular charge-transfer interaction between acceptor and donor is considered and the fact that β is not only governed by the ground-state electronic distribution but also by that of the excited states.

The hyperpolarizability is considered to be the sum of hyperpolarizabilities of the substituents (add) and an intramolecular charge transfer interaction through the π -conjugated bridge (CT):

$$\beta = \beta_{add} + \beta_{CT} \quad (37)$$

The charge-transfer part is approximated to a two-level interaction between the ground state (g) and the first excited state (e) as illustrated in Figure 2-15 below:

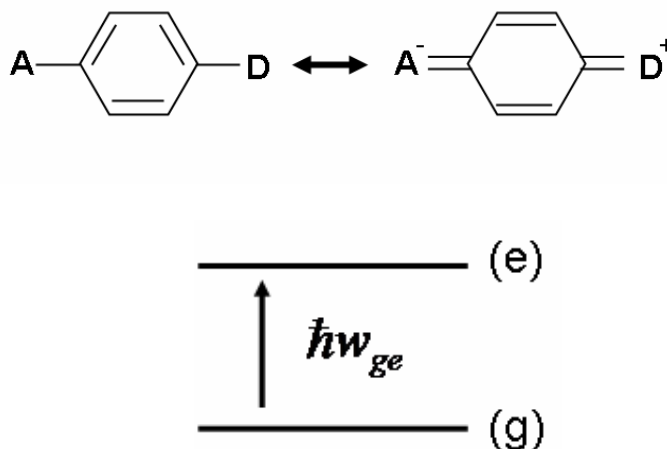


Figure 2-15: Ground state and first excited state of a push-pull molecule.

The charge-transfer contribution to the hyperpolarizability for an electro-optic effect varies with the wavelength as follows:

$$\beta_{CT}(\omega, 0, \omega) = \beta_0 \frac{(3 - \lambda_{ge}^2 / \lambda^2)}{3(1 - \lambda_{ge}^2 / \lambda^2)} \quad (38)$$

where λ_{ge} is the corresponding wavelength of absorption peak for the transition between the ground-state and the excited state ($\hbar\omega_{ge}$) and β_0 the zero-frequency value. This dispersion relation shows that the second-order nonlinearity is enhanced when the

operating wavelength is chosen to be close to the absorption maximum of chromophore. This resonance enhancement has important consequences on the design of PR polymers. The transparency of the material at half of the wavelength of the exciting beam is no longer required and as a result the nonlinearity can be much higher if the operating wavelength is closer to the absorption maximum, but still in a region of small absorption.

The first hyperpolarizability β of the chromophore can be obtained in solution through electric field-induced second harmonic generation (EFISH) experiments.⁷⁴ These experiments are usually performed off-resonance at a wavelength that is different from the one at which the PR experiments are performed. Therefore, it's convenient to extrapolate the dispersion-free value β_0 from the value that is measured by EFISH experiments.

Electro-optics:

The treatment in the field of electro-optics is slightly different than that based on susceptibility terms. One can easily show that the electro-optic tensor elements and the second-order nonlinear susceptibility elements are related by (in MKS units):

$$r_{ij} = -\frac{2}{n^4} \chi_{ji}^{(2)} \quad (39)$$

The electro-optic tensor for poled polymers is given by:

$$\tilde{r} = \begin{pmatrix} 0 & 0 & r_{13} \\ 0 & 0 & r_{13} \\ 0 & 0 & r_{33} \\ 0 & r_{13} & 0 \\ r_{13} & 0 & 0 \\ 0 & 0 & 0 \end{pmatrix} \quad (40)$$

r_{13} has units of pm/V. r_{33} is an important factor that determines the nonlinearity of the material in the case of electro-optic modulators.

In summary, the degree of index modulation in the PR effect is influenced by the electro-optic and birefringence properties of the material. On the molecular level, both polarizability and hyperpolarizability elements are important factors that need to be maximized. On the macroscopic level, the degree of order of the chromophores after poling, their concentration, and also the values of the dielectric constants (static and optical) of the host play a role in the poling process through the local field factors. As described in the Equation (38), selecting an operating wavelength at twice the absorption maximum also plays an important role.

2.5 Refractive Index Modulation

2.5.1 *Purely Electro-optic Polymers*

For purely electro-optic pre-poled polymers, the index modulation is only due to the electro-optic effect. The refractive index modulation is strongly anisotropic and depends on the configuration, the symmetry class of the sample and the polarization of the reading beam. In pre-poled polymer, the index modulation is:

$$\Delta n(x) = -\frac{1}{2} n^3 r_{eff} E_{sc}(x) \quad (41)$$

r_{eff} is the effective electro-optic coefficient which depends on the symmetry and orientation of the material.

$$r_{eff} = \hat{e}_d^* \cdot \tilde{\epsilon} \cdot [\hat{R} : \hat{k} \cdot \tilde{\epsilon} \cdot \hat{e}_i] \quad (42)$$

where $\tilde{\epsilon}$ and \hat{R} are the second-rank dielectric tensor and the third-rank electro-optic tensor, respectively. \hat{e}_i and \hat{e}_d are unit vectors of polarization for incident beam and diffracted order.

In standard slanted transmission geometry (see section 2.6.1), the effective electro-optic coefficients for s-polarized and p-polarized readout beams becomes:

$$\mathbf{r}_{eff}^s = \mathbf{r}_{13} \cos \varphi \quad (43)$$

$$\mathbf{r}_{eff}^p = \mathbf{r}_{13} \cos \alpha_1 \cos \alpha_2 \cos \varphi + \mathbf{r}_{13} \sin(\alpha_1 + \alpha_2) \sin \varphi + \mathbf{r}_{33} \sin \alpha_1 \sin \alpha_2 \cos \varphi \quad (44)$$

The effective electro-optic coefficient increases with slant angle and for the p-polarized readout beam is about 3 times stronger than s-polarized beam. Note that for the unslanted configuration ($\alpha_1 = -\alpha_2$), the electro-optic coefficient for both of the polarizations vanishes.

2.5.2 Low Glass Transition Temperature Polymers - Orientational Enhancement

As PR polymers were developed through the guest-host approach, the glass transition temperature (T_g) of the resulting composite was lowered. The chromophore was shown to act as a plasticizer. The addition of non-chromophoric plasticizers reduced

the T_g even more. If the T_g of the composite is close to room temperature or below, the chromophores are free to orient with the applied electric field. The applied field will then be a superposition of the external field and the spatially modulated space-charge field (Figure 2-16 shows the case for slanted transmission geometry). This superposition results in a periodic orientation of the chromophores that orient to the total electric field. In this case, the refractive index modulation has two contributions: the electro-optic and birefringence contribution. The electro-optic effect is related to the second-order nonlinearity, while the birefringence is due to the anisotropy of the linear polarizability. This effect is important, since it can lead to large refractive index modulation.

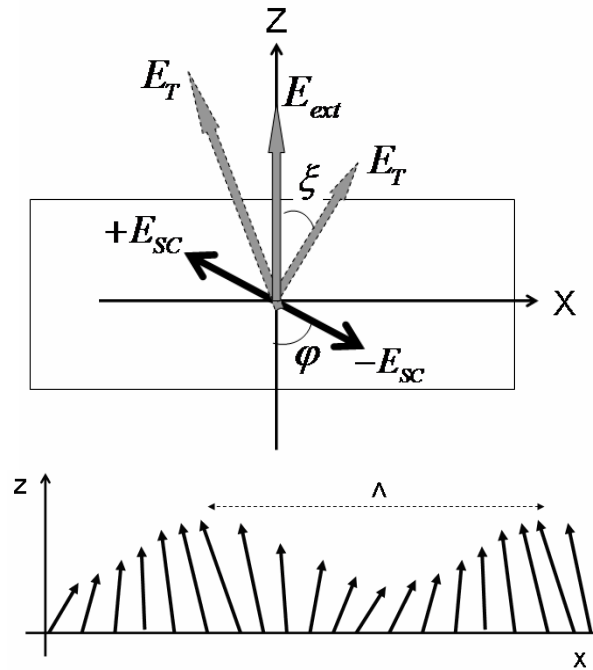


Figure 2-16: The total poling field in a low glass transition temperature polymer for standard slanted transmission geometry. Notice that the overall pattern is a combination of fixed external field and the periodically varying space-charge field.

The total poling field in the slanted transmission geometry is:

$$\mathbf{E}_T(\mathbf{r}) = [E_{sc}(\mathbf{r}) \sin \varphi] \hat{X} + [E_{ext} + E_{sc}(\mathbf{r}) \cos \varphi] \hat{Z} \quad (45)$$

with the spatially modulating space-charge field given by $E_{sc}(\mathbf{r}) = E_{sc} \exp(i\mathbf{K}\cdot\mathbf{r})$. The total poling field makes a periodically changing angle ξ with respect to the laboratory Z axis given by:

$$\xi = \arctan \left[\frac{E_{sc}(\mathbf{r}) \sin \varphi}{E_{ext} + E_{sc}(\mathbf{r}) \cos \varphi} \right] \quad (46)$$

The contribution of the birefringence to the refractive index modulated at the spatial frequency K for a given slanted four-wave mixing geometry can be written as:

$$\Delta n_{eff}^{(1)} = \frac{2\pi}{n} \hat{e}_d^* \cdot T(\mathbf{r}) \cdot \Delta \tilde{\chi}^{(1)} T^{-1}(\mathbf{r}) \cdot \hat{e}_i \quad (47)$$

here, $T(\mathbf{r})$ is the transformation matrix between laboratory and local coordinates. \hat{e}_i and \hat{e}_d are unit vectors of polarization direction for incident beam and diffracted order.

The following expressions are derived for the different contributions to the refractive index modulation for each polarization of the readout beam. One gets:

$$\Delta n_{K,S}^{(1)} = -\frac{2\pi}{n} B E_{ext} E_{sc} \cos \varphi \quad (48)$$

$$\Delta n_{K,P}^{(1)} = \frac{2\pi}{n} B E_{ext} E_{sc} \left[2 \sin \alpha_1 \sin \alpha_2 \cos \varphi - \cos \alpha_1 \cos \alpha_2 \cos \varphi + \frac{3}{2} \sin(\alpha_1 + \alpha_2) \sin \varphi \right] \quad (49)$$

with,

$$B = \frac{2}{45} N f_{\infty} (\alpha_{//} - \alpha_{\perp}) \left(\frac{\mu^*}{k_B T} \right)^2 \quad (50)$$

In the standard slanted transmission geometry, it can easily be shown that the birefringence contribution is enhanced by a factor of 2 for p-polarized readout compared to s-polarization.

Likewise, the electro-optic contribution to the refractive index modulation can be written as

$$\Delta n_{eff}^{(2)} = \frac{4\pi}{n} \hat{e}_d^* \cdot T(\mathbf{r}) \cdot \Delta \tilde{\chi}^{(2)} T^{-1}(\mathbf{r}) \cdot \hat{e}_i \quad (51)$$

with the expressions for s and p polarizations as:

$$\Delta n_{K,S}^{(2)} = \frac{8\pi}{n} C E_{ext} E_{sc} \cos \varphi \quad (52)$$

$$\Delta n_{K,P}^{(2)} = \frac{8\pi}{n} C E_{ext} E_{sc} [\cos \alpha_1 \cos \alpha_2 \cos \varphi + 3 \sin \alpha_1 \sin \alpha_2 \cos \varphi + \sin(\alpha_1 + \alpha_2) \sin \varphi]$$

(53)

with,

$$C = \frac{N f_0 f_\infty \beta \mu^*}{15 k_B T} \quad (54)$$

In the standard slanted transmission geometry, the electro-optic contribution is enhanced by a factor of 3 for a p-polarized readout compared to s-polarization. The electro-optic contribution ($\Delta n^{(2)}$) is enhanced by a factor of 2 in low T_g polymers in contrast to the case for prepoled high- T_g polymers. One has to keep in mind that, the recording geometry of the sample plays an important role for large refractive index modulations. Slant is a necessary element for achieving large index modulation. In the case of reflection geometry, one has to modify the expressions given above.

The total refractive index modulation is the summation of the first-order (birefringence) and second-order (electro-optic) contributions described above. Based on this summation, one can define the following figure of merit for chromophores:⁷⁵

$$FOM = \frac{2}{9kT} \mu^2 \Delta\alpha + \mu\beta \quad (55)$$

To maximize the orientational birefringence, large polarizability anisotropy $\Delta\alpha = (\alpha_{//} - \alpha_{\perp})$ is desired. On the electro-optic side, the chromophore should have both a large hyperpolarizability β and large dipole moment μ for the best refractive index modulation.

2.6 Diffraction Theory of Thick Gratings

Depending on the material, the holographic information is recorded as either amplitude or phase grating. Amplitude holograms have lower diffraction efficiencies than phase holograms and are therefore used more rarely. Most of the time, the holograms written in the PR materials are volume (thick) holograms. Materials used for phase holograms reach the theoretical diffraction efficiency for holograms, which is 100% for thick holograms (Bragg) and 34% for thin holograms (Raman-Nath).⁷⁶ As stated in Kogelnik's paper,⁷⁷ the Q factor can be used to separate the Bragg (one strong diffracted order at Bragg incidence) from the Raman-Nath (several diffracted orders) regimes:

$$Q = 2\pi\lambda d / n\Lambda^2 \quad (56)$$

where λ is the vacuum wavelength, d the thickness of the film, n the mean refractive index and Λ the grating spacing. One can consider a grating 'thick' when the condition $Q > 5-10$ holds, while the condition for the thin grating case is: $Q < 1$. For instance, when the sample is 100 μ m thick, this condition requires $\Lambda < 7\mu$ m to see a thick hologram

effect and $\Lambda > 15\mu m$ to observe thin hologram effect. One should keep in mind that, the angular Bragg selectivity will reduce as the device is made thinner. The different types of diffraction orders are depicted schematically in Figure 2-17.

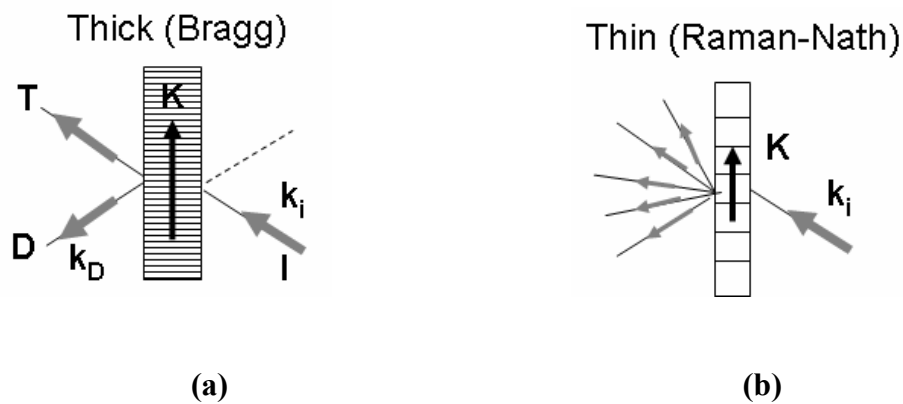


Figure 2-17: Schematic representation of diffraction orders for Bragg (a) and Raman-Nath (b) regimes.

When the index modulation is large in the material, the state of the hologram can be reliably specified if a parameter ρ (first defined by Nath)⁷⁸ is utilized. It is defined as

$$\rho = \lambda^2 / \Lambda^2 n \Delta n_1 \quad (57)$$

where Δn_1 is the refractive index modulation for a phase grating. Based on this parameter, the hologram is considered thin when $\rho \leq 1$ holds.

The sum of the propagation wave vectors in Bragg gratings can be given as:

$$\mathbf{k}_D = \mathbf{k}_i \pm \mathbf{K} \quad (58)$$

where \mathbf{k}_D is the diffracted, \mathbf{k}_i incident, \mathbf{K} the grating wave vector. In this case, the diffraction is into one order which is the first order.

However in the Raman-Nath (thin) case, there will be multiple orders:

$$\mathbf{k}_p = \mathbf{k}_i \pm m\mathbf{K} \quad m = 0, 1, 2, \dots \quad (59)$$

2.6.1 *Transmission Geometry*

When both of the writing beams are incident from one side of the recording sample, the geometry is considered as transmission geometry. The practical range for grating spacing in this geometry is 1-20 μm for visible wavelengths.

The applied electric field plays an important role in the photogeneration, transport and poling processes. PR polymers are typically sandwiched in between two pieces of transparent ITO-coated glass. The electric field is then applied in the direction perpendicular to polymer film. The sample has to be slanted when recorded in transmission geometry. That's because (1) the effective electro-optic coefficient will be large due to the symmetry of polymers poled this way (2) there will be a component of the applied field along the grating vector in order to act as a drift bias for the transport of the carriers.

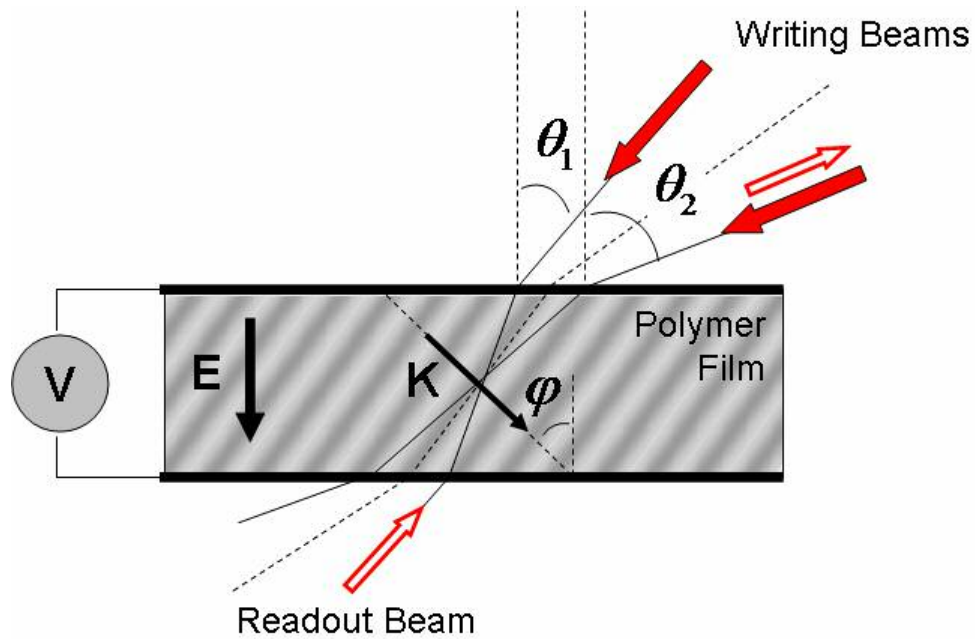


Figure 2-18: Schematic of slanted transmission geometry used in four-wave mixing experiments. In our standard transmission geometry $\theta_1 = 50^\circ$ and $\theta_2 = 70^\circ$. Therefore, the slant angle of grating, ϕ , becomes 58.8° for a refractive index of 1.65.

In the transmission geometry, the grating spacing and the amplitude of the wave-vector are calculated from:

$$\Lambda = \frac{\lambda}{2n \sin[(\alpha_2 - \alpha_1)/2]} \quad K = \frac{2\pi}{\Lambda} \quad (60)$$

where α_1 and α_2 are writing beam angles with respect to the laboratory Z axis measured inside the sample and n the refractive index of polymer. In our standard geometry, the

grating is spacing is $3.1\mu\text{m}$ when the writing beams are coming at 50° and 70° for a wavelength of 633nm ($n=1.65$).

The slant angle defined inside the material is given by:

$$\varphi = \frac{\pi}{2} - \frac{(\alpha_1 + \alpha_2)}{2} \quad (61)$$

The diffraction efficiency can be obtained from the coupled-wave theory for thick holograms developed by Kogelnik⁷⁷. The diffraction efficiency for a lossless phase grating under Bragg-mismatch condition is given by:

$$\begin{aligned} \eta &= \sin^2 \left(\nu^2 + \xi^2 \right)^{1/2} / (1 + \xi^2 / \nu^2) \\ \nu &= \frac{\pi \Delta n d}{\lambda \sqrt{c_i c_d}} \hat{e}_i \cdot \hat{e}_d \\ \xi &= \Delta \alpha K d \sin(\varphi - \alpha_1) / 2c_d = -\Delta \lambda K^2 d / 8\pi n c_d \\ c_i &= \cos \alpha_i \\ c_d &= \cos \alpha_i - \frac{\lambda}{n \Lambda} \cos \varphi \end{aligned} \quad (62)$$

where Δn is the refractive index modulation amplitude of the phase grating, \hat{e}_i and \hat{e}_d are the unit polarization vectors of the incident reading beam and the diffracted beam and d the thickness of the material. $\Delta \alpha$ is the deviation angle inside the materials for off-Bragg conditions, while c_i and c_d are the obliquity factors.

When the readout beam is incident at α_1 , with the expressions for Λ and φ , the obliquity factors reduce to $c_i = \cos \alpha_1$ and $c_d = \cos \alpha_2$, *i.e.* diffracted order will counter-

propagate with the other writing beam. At Bragg incidence, the expression given above can be simplified to the form:

$$\eta = \sin^2 \left[\frac{\pi \Delta n d}{\lambda \sqrt{\cos \alpha_1 \cos \alpha_2}} \cos(\alpha_1 - \alpha_2) \right] \quad (63)$$

This expression is used to determine the internal (lossless) diffraction efficiency in our polymers. The absorption and reflection losses are included later to calculate the external diffraction efficiency. The case for lossy gratings discussed in Kogelnik's paper is not included here, because the absorption loss doesn't change the behavior of the diffraction efficiency curve other than reducing the peak value. One can combine both the Kukhtarev model and Kogelnik's expression for thick holograms and obtain a typical diffraction efficiency curve with respect to the external field and grating spacing as shown in Figure 2-19. The variations in trap density are also depicted.

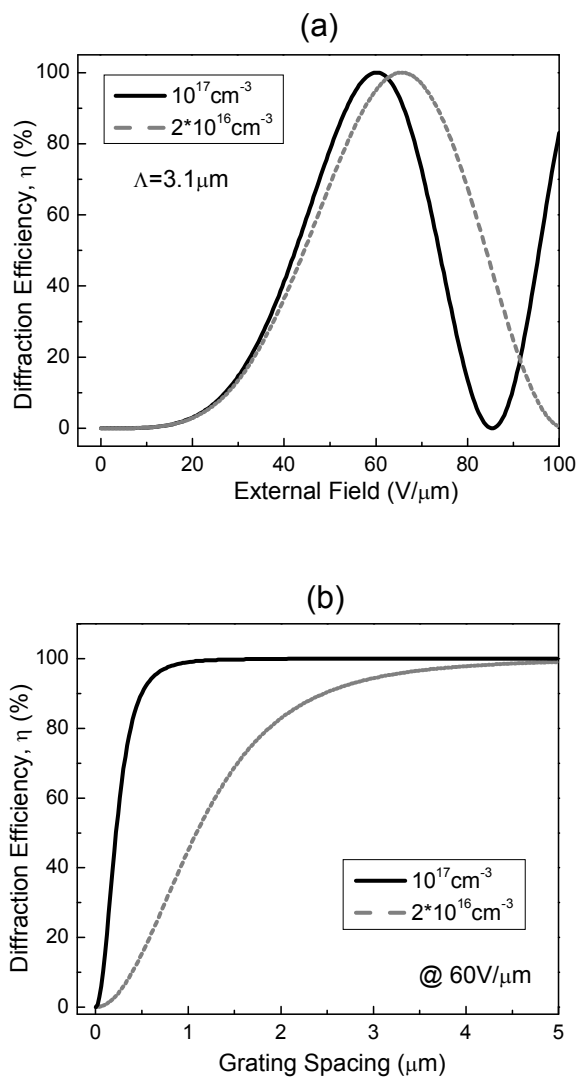


Figure 2-19: The effect of applied electric field (a) and grating spacing (b) on the diffraction efficiency of a photorefractive transmission grating. Two different cases of effective trap densities are considered.

When the reading beam is deviated from the Bragg angle, the efficiency will vary as shown in Figure 2-20 for transmission.

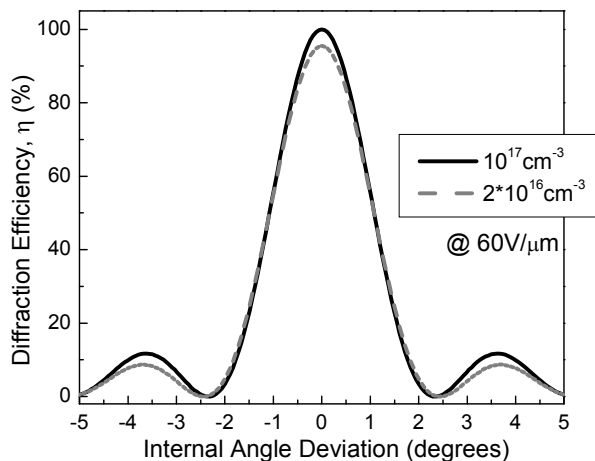


Figure 2-20: The diffraction efficiency for a lossless phase grating under Bragg-mismatch conditions (transmission geometry).

2.6.2 Reflection Geometry

In the reflection geometry, the writing beams are incident on different sides of the recording sample. The practical range for grating spacing in this geometry is 0.15-0.3 μm at visible wavelengths. With this geometry, the applied field will have a large projection on the grating vector to improve the space-charge field. On the other hand, due to the symmetry class of poled polymers, the effective electro-optic coefficient will decrease if the writing beam angles with respect to the laboratory Z axis (sample normal) are reduced.

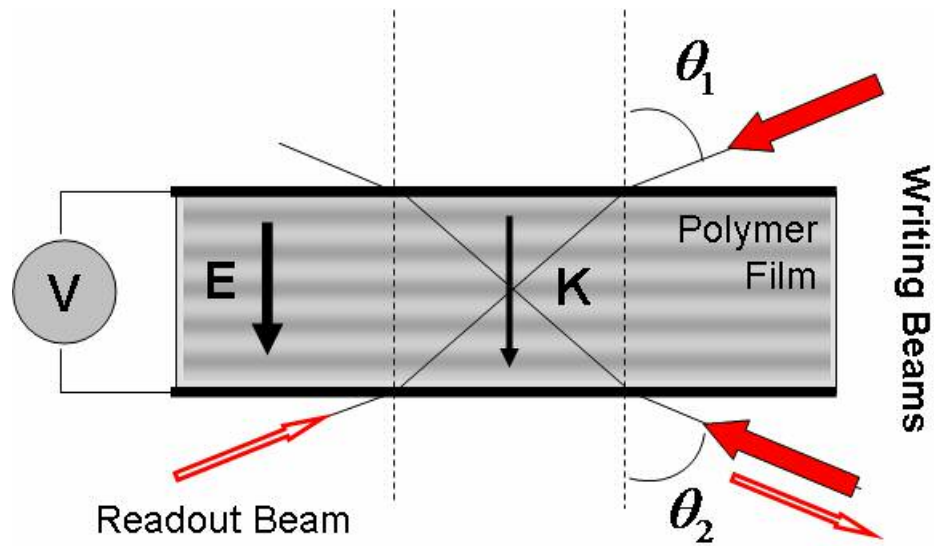


Figure 2-21 : Schematic of the reflection geometry used in four-wave mixing experiments. In our standard symmetric reflection geometry $\theta_1 = \theta_2 = 72^\circ$, and $\varphi = 0$.

In reflection, the grating spacing and the slant angle are:

$$\Lambda = \frac{\lambda}{2n \sin \left[\frac{\pi - (\alpha_2 + \alpha_1)}{2} \right]} \quad (64)$$

$$\varphi = (\alpha_2 - \alpha_1) / 2 \quad (65)$$

The angles are with respect to the laboratory Z axis measured inside the sample (see Figure 2-21). The grating spacing is $0.235 \mu\text{m}$ when the writing beams are incident at 72 degrees from each side of the sample at a wavelength of 633nm.

In reflection geometry, the diffraction efficiency for a lossless phase grating under Bragg-mismatch condition is given by:⁷⁷

$$\begin{aligned}
 \eta &= 1 / \left[1 + (1 - \xi^2 / \nu^2) / \sinh^2 \left(\sqrt{\nu^2 - \xi^2} \right) \right] \\
 \nu &= \frac{i\pi\Delta nd}{\lambda\sqrt{c_i c_d}} \hat{e}_i \cdot \hat{e}_d \\
 \xi &= \Delta\alpha K d \sin(\varphi - \alpha_1) / 2c_d = \Delta\lambda K^2 d / 8\pi n c_d
 \end{aligned} \tag{66}$$

At Bragg incidence, the expression given above can be simplified into the form:

$$\eta = \tanh^2 \left[\frac{\pi\Delta nd}{\lambda\sqrt{\cos \alpha_1 \cos \alpha_2}} \right] \tag{67}$$

This function defines the internal (lossless) diffraction efficiency in our polymers. The curve for diffraction efficiency is given in Figure 2-22. The absorption and reflection losses are added later to calculate the external diffraction efficiency.

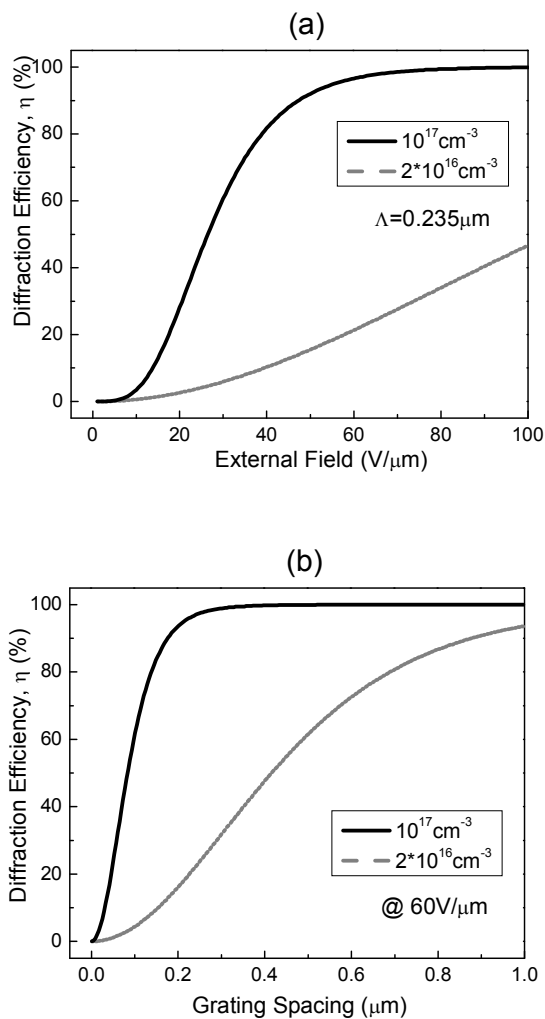


Figure 2-22: The effect of applied electric field (a) and grating spacing (b) on the diffraction efficiency of a photorefractive reflection grating. Two different cases of effective trap densities are considered.

When the reading beam deviates from the Bragg angle, the efficiency will vary as shown in Figure 2-23.

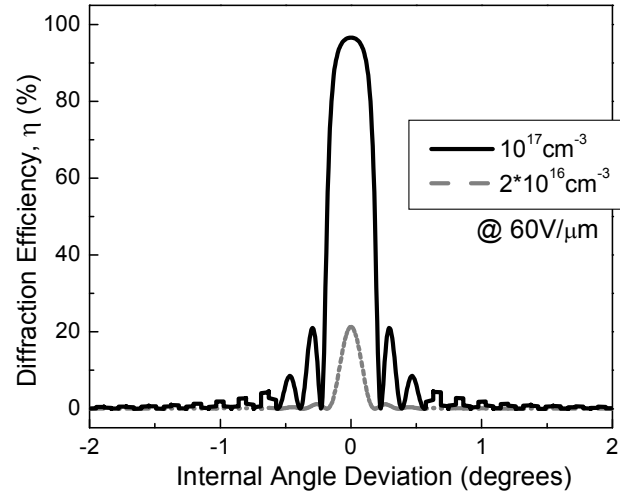


Figure 2-23: The diffraction efficiency for a lossless phase grating under Bragg-mismatch conditions (reflection geometry).

Reflection holograms are more sensitive to the Bragg mismatch than transmission holograms, as the Kogelnik's Q is larger in this geometry.

2.7 Two-Beam Coupling (Self Diffraction) Theory

In the two beam coupling case, the two writing beams have coherent energy coupling, in which the intensity of one of the beams can be amplified at the expense of the loss for the other. This effect happens when there is a phase shift between the light grating and the phase grating. This non-local response is the signature of the PR effect and opens a wide range of applications. Maximum energy transfer occurs when the light distribution and the refractive index modulation are phase shifted by 90° . This phase shift happens naturally when the space-charge field is built up by diffusion process only (no applied field). However, in polymers the photogeneration and transport properties are

highly field-dependent; therefore the charge carriers build up space charge field through drift, instead of diffusion. In the drift case, the phase shift is usually smaller than 90° .

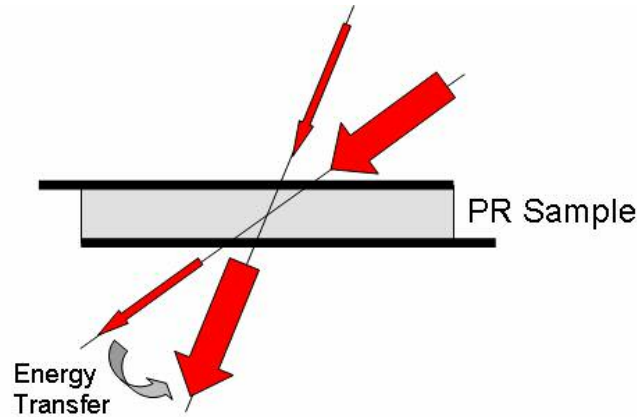


Figure 2-24: Two beam coupling geometry: energy is transferred from the pump beam into the probe beam.

Coherent energy exchange between two writing beams is characterized by a gain coefficient Γ which is given by:

$$\Gamma = \frac{4\pi}{\lambda} (\hat{e}_1 \cdot \hat{e}_2^*) \Delta n \sin \Theta \quad (68)$$

where \hat{e}_1 and \hat{e}_2 are the polarization vectors of the writing beams, Δn the refractive index modulation and Θ the phase shift between the space-charge field and the interference pattern.

To determine the value of the gain coefficient, one generally conducts an experiment in which the intensity of the transmitted beam $I_1(z)$ is first measured with the second beam on and then measured with the second beam blocked. The ratio of these two intensities is defined as the gain factor γ_0 :

$$\gamma_0 = \frac{I_1(z)(I_2 \neq 0)}{I_1(z)(I_2 = 0)} = \frac{(1+b)\exp(\Gamma d)}{b + \exp(\Gamma d)} \quad (69)$$

where we have introduced the ratio of writing beams, $b = I_2(0)/I_1(0)$.

Finally the gain coefficient is derived from the measured value of γ_0 and the ratio between the intensities of the two interfering beams:

$$\Gamma = \frac{1}{d} [\ln b\gamma_0 - \ln(1+b-\gamma_0)] \quad (70)$$

A weak signal beam can be amplified when interfered with a strong pump beam inside a PR material. Over a distance of d , the intensity of the signal beam will increase exponentially:

$$I_1(d) \approx I_1(0) \exp[(\Gamma - \alpha)d] \quad (71)$$

where α is the absorption coefficient. The typical behavior of TBC gain as a function of field and grating spacing is plotted in Figure 2-25.

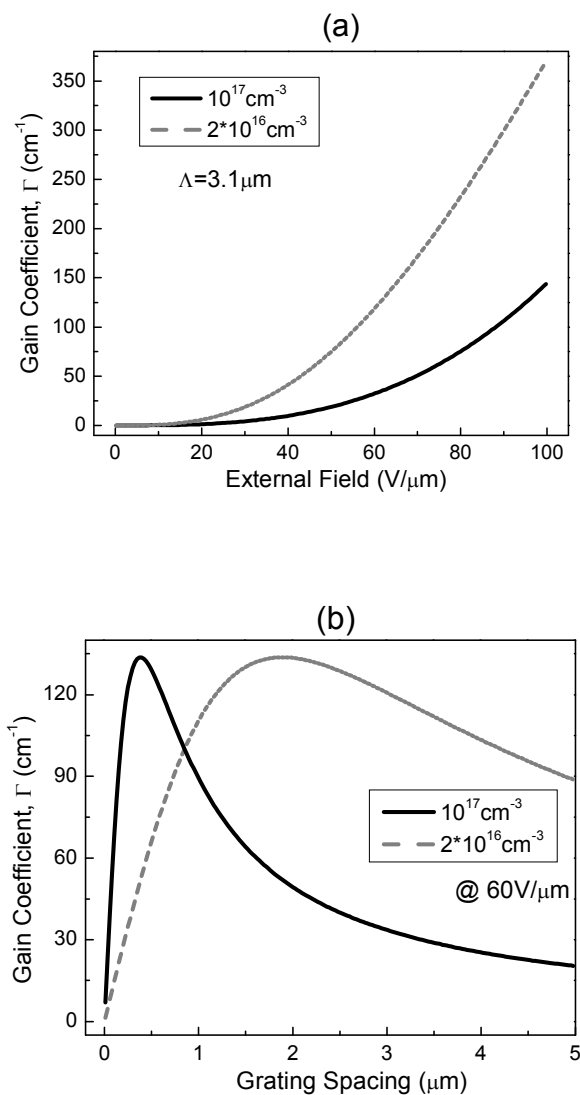


Figure 2-25: The effect of applied electric field and grating spacing on the two-beam coupling gain of a photorefractive transmission grating. Two different cases of effective trap densities are considered.

Note that, depending on the trap density in a PR material, the best two-coupling gain is obtained at a certain grating spacing value.

3 MATERIAL DEVELOPMENT

Over the past several years, tremendous progress has been made in improving photorefractive (PR) organic materials. High performance properties has been achieved in a variety of different functional materials such as guest-host polymer composites, fully-functionalized polymers, polymer dispersed liquid crystals (PDLCs) and hybrid organic-inorganic composites. A detailed description for guest-host polymer composites will be given, due to their wide chemical flexibility and their primary use in our PR devices. An overview of other materials is also provided for comparison.

3.1 Guest-Host Polymer Composites

In PR polymers, a guest-host composite approach is generally adopted to achieve the best combination of separate functions that lead to photorefractivity. A host polymer is chosen to efficiently transport holes and it can also act as a trapping agent, a sensitizer is introduced that generates the necessary charges, a nonlinear optical (NLO) chromophore is included to enhance the refractive index modulation and the addition of a plasticizer facilitates the orientation of these chromophores. In most PR polymers made today, an externally applied field is used to both accelerate the charge transport process and to orient the chromophores such that both bulk polarizability anisotropy and intrinsic electro-optic effects are induced. To increase the speed and efficiency of this process at ambient temperatures, a plasticizing molecule is often added into the host, with the effect of lowering the glass transition temperature of the host to ambient temperature (20-25°C). Molecules with large polarizability anisotropies and dipole moments are chosen and the

resulting orientation in the presence of the applied field (and the environment of a low-glass-transition polymer) provides the desired refractive index change. Relatively small molecules are generally preferred, to increase the orientation speed and to reduce the absorption of chromophores in the visible region.

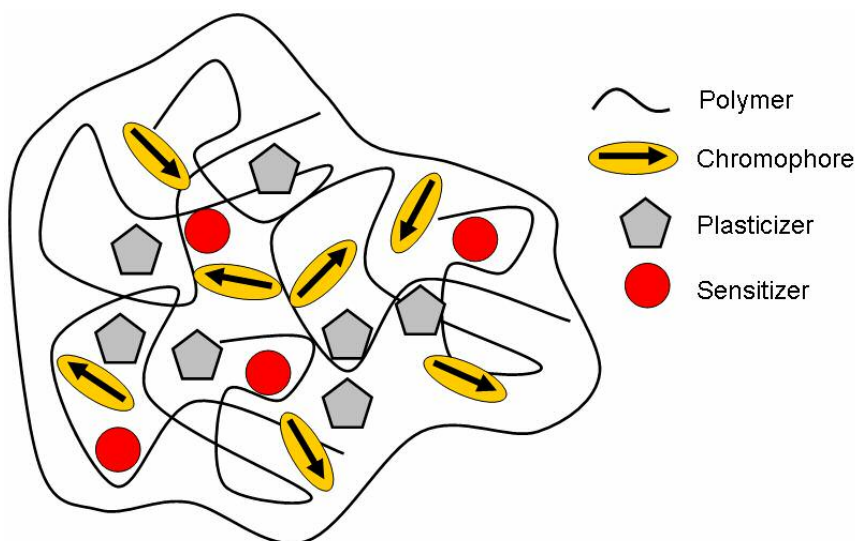


Figure 3-1: Typical guest-host system. The functional elements are added into the polymer matrix.

Typical photoconducting polymers contain highly conjugated (i.e. lots of delocalized π electrons) monomers. Both the backbone and more importantly the side chains contribute to the conduction. Highly conjugated side chains are preferred for a rapid PR performance. Photoconducting polymers are usually hole-transport materials.

The physical properties of an organic polymeric system depend not only the chemical structure of the molecules, but also on the average chain length and distribution, tacticity (3D arrangement) and glass-transition temperature (T_g). T_g determines whether or not significant molecular motion can take place. Below T_g , functional side groups or

dopants such as electro-optic chromophores can have restricted orientational mobility and strongly interact with the polymer backbone. However, above T_g they can freely rotate and chromophores can align to the applied field. A room temperature T_g has been an important factor in achieving high diffraction efficiencies. It's preferred so that the chromophores can orient freely to enhance the refractive index modulation in the system.

Chromophores can also be used for sensitization. The length of the π -conjugation bridge defines the absorption maximum of the molecule. This can be understood through particle in the box model, commonly taught in the quantum mechanics. The narrower the well, the wider the separation between the energy of the states is. For sensitization in the near infrared (NIR) region, the conjugated bridge needs to be long enough to get low-energy absorption. A chromophore with an absorption peak in the NIR has recently been included in a composite for demonstration of PR effect at 980nm.²² However, longer conjugated bridge length can lead to reduced orientational properties.

Overall, the advantage of guest-host polymer composites is the ability to tune their properties by varying the concentration and type of constituents. The disadvantages include the potential phase separation and crystallization that can occur when highly polar chromophores are added in large concentrations to nonpolar matrices.⁷⁹ Also, as discussed above, the addition of a plasticizer reduces the T_g and therefore enhances chromophore orientation in the meantime increases the inert volume, which deteriorates photoconductive and NLO properties.

Material Design:

The most common PR composites include ~40-60 wt % of photoconductive polymer (PVK, PATPD, TPD-PPV, etc.) to provide sufficient transport sites, ~25-35 wt % of NLO chromophore (7-DCST, DBDC, LCs, etc.) to ensure a sufficient electro-optic response, ~15-30 wt % of plasticizer (ECZ, BBP, etc.) to facilitate chromophore orientation by lowering the T_g of the material, and finally, a small amount (usually below 1 wt %) of sensitizer (e.g., C_{60} , TNFDM, etc.) to assist in charge photogeneration. The chemical structures for each of these functional elements commonly used in our polymer composites are given below:

3.1.1 Sensitizers

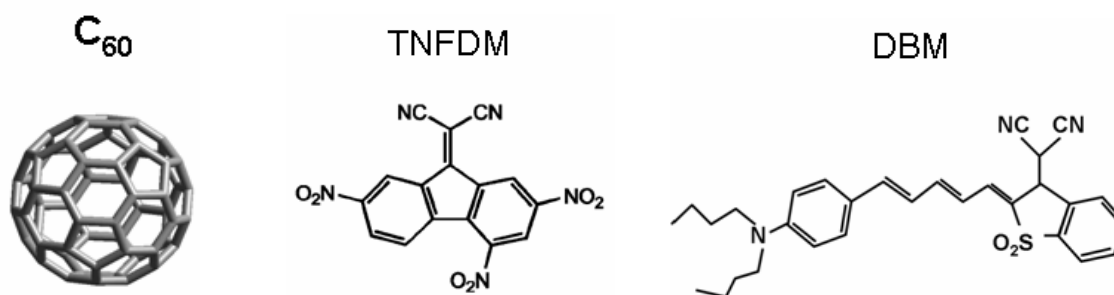


Figure 3-2: Molecular structures for sensitizers commonly used in our guest-host polymer systems. C_{60} provides sensitivity in the red, TNFDM:PATPD provides absorption in the NIR (700-850nm) due to charge-transfer complex and DBM dye provides absorption for 900-1000nm region. Absorption at 532nm is obtained through the 7-DCST chromophore (see Figure 3-4).

3.1.2 Transport Matrices

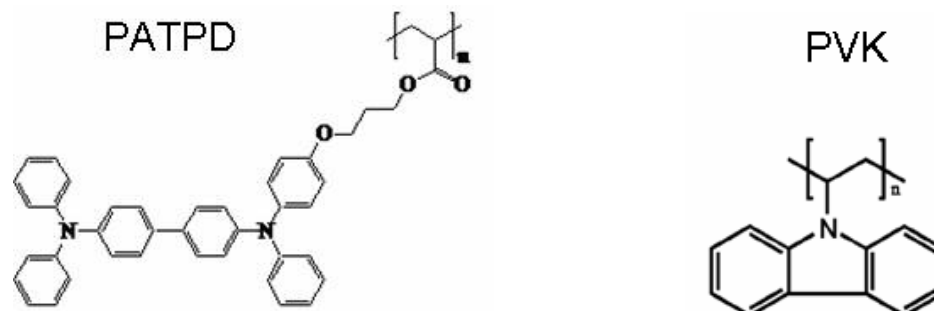


Figure 3-3: Molecular structures for photoconducting polymers commonly used in our guest-host polymer systems. PATPD matrix has more conjugated sites, therefore better charge mobility.

3.1.3 NLO Chromophores

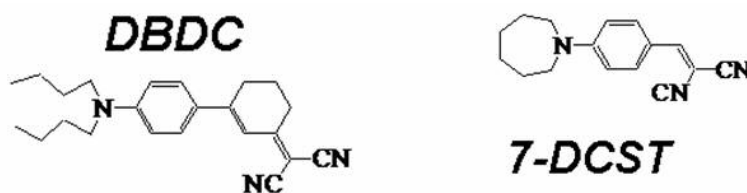


Figure 3-4: Molecular structures for NLO chromophores commonly used in our guest-host polymer systems. 7-DCST is a smaller chromophore, therefore it has a faster orientation speed. 7-DCST also provides the necessary absorption at 532nm.

3.1.4 Plasticizers

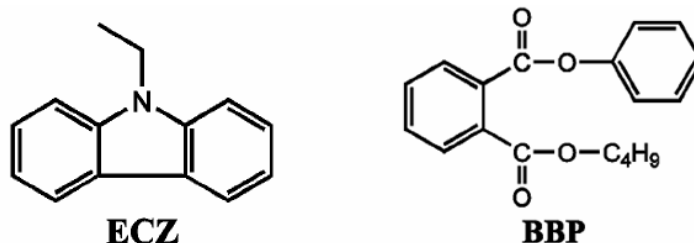


Figure 3-5: Molecular structures for plasticizer commonly used in our guest-host polymer systems.

3.2 Fully-Functionalized Polymers

In fully-functionalized polymers, different functional elements (sensitizer, transport element, NLO chromophore) are all incorporated as side chains to polymer backbone. This approach requires a much larger synthetic effort and has not been used as much as the guest-host approach. Fully functionalized polymers eliminate the problems of phase separation and crystallization and therefore could lead to better thermal stability and longer shelf life for potential devices. A recent review of strategies of material design applied to the synthesis of fully functionalized polymers can be found in Ref. 80. Despite their long shelf times, the PR response speed in these materials has been slow.

3.3 Amorphous Glasses

Organic glasses are materials containing typically one primary molecular component that provides the functions of amorphous polymer as well as the NLO molecule. The advantage of organic glasses is that the density of NLO moieties and charge transporting sites is the maximum achievable due to tight packing of the

molecules in the glass, yet there is no phase separation problem such as that which occurs in polymer composites when high concentration of chromophores is introduced. The disadvantage is that the easy tunability of properties that is the case for polymer composites is reduced to synthetic modifications of the glass-forming molecule. In addition, the molecule must be designed to prevent self-crystallization to maintain optical clarity and be tuned to the optimal optical and thermal properties. The response time in this class of material is longer, of the order of seconds.²⁰

3.4 Polymer Dispersed Liquid Crystals

Polymer-dispersed liquid crystals (PDLCs) contain high concentrations of both polymer and liquid crystalline molecules that phase separate into droplets. In PDLCs used for photorefractivity, the polymer typically provides the photoconductive properties needed for the space-charge field formation, while the liquid crystal (LC) droplets provide orientational nonlinearity needed for the refractive index modulation. The advantage of PDLCs compared with traditional polymer composites is that LC molecules in droplets can be reoriented with much lower electric fields than those used in polymer composites, therefore less power consumption results. A recent review of LC-containing PR materials, including PDLCs can be found in Ref. 81. The weak points of PDLCs include high losses due to scattering, which prevent high net gain, and slow, on the order of minutes, PR dynamics due to their low mobilities. LC containing PR materials are good for low resolution applications where the gratings are usually in the Raman-Nath regime ($Q < 1$) and therefore have low efficiency.

3.5 Hybrid Organic Inorganic Composites

A recent review of the optical properties of hybrid organic-inorganic composites can be found in Ref. 82. Semiconductor quantum dots such as CdS or CdSe, have been introduced in small concentrations into standard PVK and PPV based composites to improve the sensitivity.^{83,84} For PR materials, an attractive property of quantum dots as sensitizer is that their wavelength of maximum sensitivity is size-dependent which allows for tunability of the PR sensitivity over a range of wavelengths such as near-infrared wavelengths.⁸³ In addition, it was found that doping photoconductive polymers (e.g., PVK, PPV) with quantum dots improved photoconductive properties.⁸⁵ Inorganic dopants other than quantum dots have been included as trapping agents into a polymer composite.⁸⁶

4 EXPERIMENTAL TECHNIQUES

In this chapter, we will describe the measurement techniques used to test the performance of state-of-art photorefractive (PR) polymers. Other than direct measurement of field-dependent diffraction efficiency in the four-wave mixing geometry and gain in the two-beam coupling geometry, we will also examine the experiments related to probing subprocesses that contributes to the PR effect, such as photoconductivity and ellipsometry.

4.1 Sample Preparation

The polymer composites prepared were based on a guest-host approach. The polymer host (usually a photoconducting polymer) is doped with functional elements such as the chromophore, sensitizer and plasticizer in predetermined weight percentages. The components can be in powdered, crystalline solids, or in liquid phase. The purity of each component is critical to obtain reproducible and reliable results. The techniques of purification vary for different materials, which we won't be discussing here.

To make the pre-cake of the sample, the material components are combined in a solvent to allow thorough mixing. Often the sensitizer is pre-dissolved in a solvent to disperse it better and to simplify dispensing of a relatively small amount of material easy. The solution of components is filtered and then put in a flask and stirred. The evaporation process is done with a rotary evaporator which can remove the bulk of the solvent, through application of both heat and mild vacuum to speed the process. Controlled evaporation is achieved by partially submerging the flask containing the solution in a

heated bath of distilled water. The rotation prevents the solids from turning into foam by the boiling solvent. When the material is dry enough it is removed from the evaporator and drying is continued in a vacuum oven at higher temperature. The dried product is then extracted from the flask and placed between two sheets of glass. The sample is placed on a hot plate and brought to a temperature below melting temperature which makes it viscous. A shearing action with some pressure is applied to make a homogeneous film. The sample is often quenched by contact with a cold plate to preserve its amorphous state after mixing.

Once the cake is ready, it is cut into small pieces and placed on one of the two small glass substrates with indium-tin oxide (ITO) electrodes facing upward. To ensure a uniform and desired thickness of the polymer film, small dots of glass beads, suspended in silicon vacuum grease are dropped around the edges of one glass substrate. The two halves of the sample are then placed on a hot plate to allow the material to approach its melting temperature. The two halves are then gently pressed together to prevent formation of air bubbles in the film. The edges of the sample are sealed with epoxy to protect the composite film from environmental factors such as moisture absorption, as well as to make them more robust in handling.

Measurement of Glass Transition Temperature (T_g):

A common method used to measure T_g is differential scanning calorimetry (DSC). The composite is placed into a small pan and heated while the device monitors the heat flow in and out of the sample. A typical heat flow curve can be obtained as shown in the picture. Polymers will burn typically above 300-400 °C. Some composites can have a

broad T_g and making it hard to determine the exact value. To lower the T_g of a polymer, a plasticizing element is added. The plasticizer can typically be a monomer of the photoconducting polymer or single molecules that will introduce extra space for motion. A plasticizer with a HOMO level close to the polymer matrix is preferred for better charge transport properties.

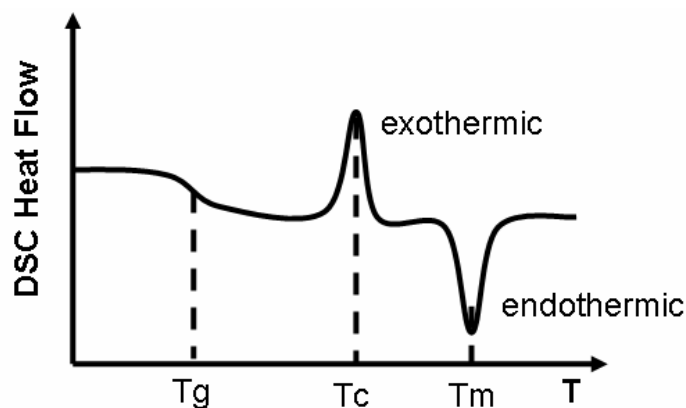


Figure 4-1: Typical DSC measurement curve. The first drop in the heat flow is referred as T_g (glass transition temperature). The peak in the curve is at T_c (crystallization temperature) and the dip is at T_m (melting temperature)

4.2 Probing Various Sub-processes Relevant to Photorefractivity

4.2.1 Linear Absorption Properties

Determining the absorption coefficient of polymers is crucial as it's the first step in the PR process. In most cases, we want to know the absorption over a range of wavelengths. We have used a Cary 5G spectrophotometer for this purpose. The Cary 5G uses broadband sources and detectors in conjunction with monochromators to provide a

high signal-to-noise ratio with control over the bandwidth and resolution used in the measurement. There are two arms to allow precise comparison of two samples and correct the baseline. One is used as a reference path, while the other is used for sample measurements. The reference path, however, is often simply an empty device with ITO coated glass but no polymer. There are various types of sample fixtures with apertures for controlling the beam size. It is generally important to use similar fixtures in the two sample paths, even if there is not a reference sample in the reference path. The Cary 5G allows calibration of the full-scale (100% transmittance) and baseline (0% transmittance) values, which improves accuracy, as well. The results are generally recorded as either transmittance values or absorbance. The transmittance is defined as:

$$T = \frac{I_{transmitted}}{I_{incident}} \quad (72)$$

whereas absorbance, also called optical density (OD) defined as

$$A = OD = \log_{10} T = \alpha d \log_{10} e \quad (73)$$

here d is the sample thickness in centimeter and α the absorption coefficient in units of inverse centimeters.

4.2.2 Photoconductive Properties

The first stage of PR grating formation (build-up of the space charge field) relies on the photoconductive properties of materials such as photogeneration efficiency, carrier mobility, trapping and recombination. Among many other techniques, dc

photoconductivity experiments proved to be very effective in studying all these processes. Here we will discuss only dc conductivity experiments.

Photoconductivity is measured at the operating wavelength using a conventional dc technique. An electric field is applied to the sample and the weak current passing through the device is recorded. The photocurrent is calculated as the difference between total current in the presence of light (typically $1\text{W}/\text{cm}^2$) and the dark current. The ‘‘apparent’’ photoconductivity values are calculated from the measured total current (i_{tot}), dark current (i_{dark}), applied electric field (E) and electrode overlap area ($S_{electrode}$):

$$\sigma_{photo} = (i_{tot} - i_{dark}) / (ES_{electrode}) = \sigma_{tot} - \sigma_{dark} \quad (74)$$

where σ_{tot} is the total conductivity and σ_{dark} is the dark conductivity. In this case, the beam is assumed to cover the whole electrode overlap area. If a beam with smaller spot size (S_{beam}) is incident, the equation will be slightly modified, which can be given by:

$$\sigma_{photo} = \frac{i_{total}}{ES_{beam}} - \frac{i_{dark}}{ES_{electrode}} (S_{electrode}/S_{beam} - 1) \quad (75)$$

To assign the change in photoconductivity upon sensitization to a certain process, it is necessary to account for absorption in the samples with relatively large absorption coefficients, because the beam considerably attenuates as it propagates through the medium. If the absorbing medium is viewed as a sequence of resistors⁸⁷ whose resistance increases monotonically as the beam is attenuated, then the intrinsic photoconductivity σ_{photo}^i of the sample (assuming uniformly illuminated electrodes) is

$$\sigma_{photo}^i = \sigma_{dark} \frac{\exp[\alpha da] - \exp[\alpha da \sigma_{dark} / \sigma_{tot}]}{\exp[\alpha da \sigma_{dark} / \sigma_{tot}] - 1} \quad (76)$$

where a is a power law exponent ($\sigma_{photo}^i \sim I^a$), d is the sample thickness, and α is the absorption coefficient. For small absorption coefficients ($\alpha d \ll 1$), the equation transforms into “apparent” form.

To eliminate the contribution of the increase in absorption to the increase in photoconductivity, we need to normalize the intrinsic photoconductivity values at the absorbed light intensity as follows:

$$\sigma_{photo}^n = \frac{\sigma_{photo}^i}{1 - \exp(-\alpha d)} \quad (77)$$

4.2.3 *Orientational Properties*

Refractive index modulation in PR polymers is through electro-optic nonlinearities. In low- T_g PR organic materials, a major mechanism responsible for this step is NLO chromophore reorientation in the space-charge field (OE effect)⁸⁸. Therefore, the ability of the chromophores to reorient in the electric field is an important property that contributes to the overall PR performance.

Poled polymer system are uniaxial with two different refractive indices (ordinary and extraordinary), n_o and n_e (see Figure 4-2). If the incoming wave is s-polarized, it will only see the ordinary refractive index: $n(\theta) = n_o$, independent of angle θ . In the case of p-polarized wave, the index ($n_e(\theta)$) is given by:

$$\frac{1}{n_e^2(\theta)} = \frac{\cos^2 \theta}{n_o^2} + \frac{\sin^2 \theta}{n_e^2} \quad (78)$$

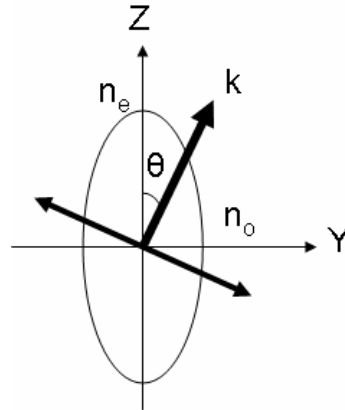


Figure 4-2: The Index ellipsoid: a p-polarized beam will sense both ordinary and the extra-ordinary refractive index.

Electric field-induced birefringence was measured using a conventional transmission ellipsometry technique (see Figure 4-3). Light of a wavelength longer than the operating wavelength (so there will be no absorption) is employed. The sample is placed between two crossed polarizers. The angle between the sample normal and the light beam is usually picked as 45° . The residual sample birefringence is compensated by a Soleil-Babinet compensator, (1) to eliminate transmitted light that could be detected in the absence of the electric field or (2) to add a $\pi/2$ phase retardance to operate in the linear section of intensity curve. The electric field was applied to the sample and the intensity of transmitted light was recorded as a function of increasing bias field. The birefringence ($|n_e - n_o|$) of the poled polymer was calculated using the formula given below:

$$|n_e - n_o| = \frac{\lambda \cos \varphi}{2\pi L \sin^2 \varphi} \arcsin(\sqrt{I/I_{\max}}) \quad (79)$$

where λ is the wavelength, φ is the internal angle of incidence, L is the sample thickness, and I_{\max} is the maximum transmitted intensity.

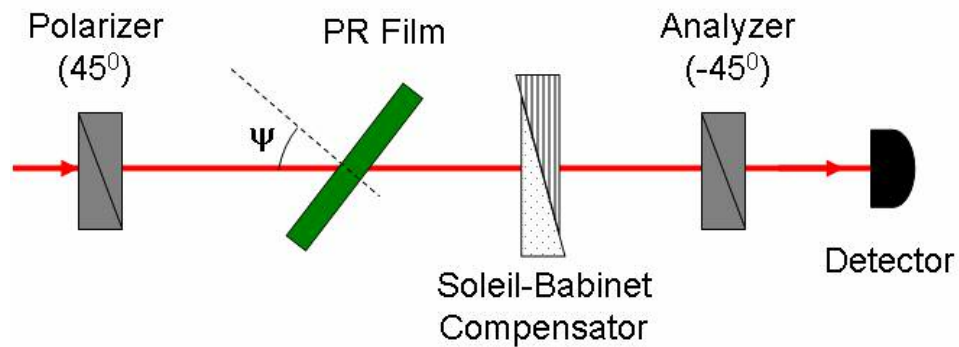


Figure 4-3: Schematic diagram of a transmission ellipsometry setup.

Based on the linear theory (see Section 2.4.1) in poled polymers, an external bias field will induce index modulation which has quadratic field behavior. Therefore, a typical transmittance curve in ellipsometry measurements can be fitted to a quadratic birefringence ($|n_e - n_o|$) function (see Figure 4-4).

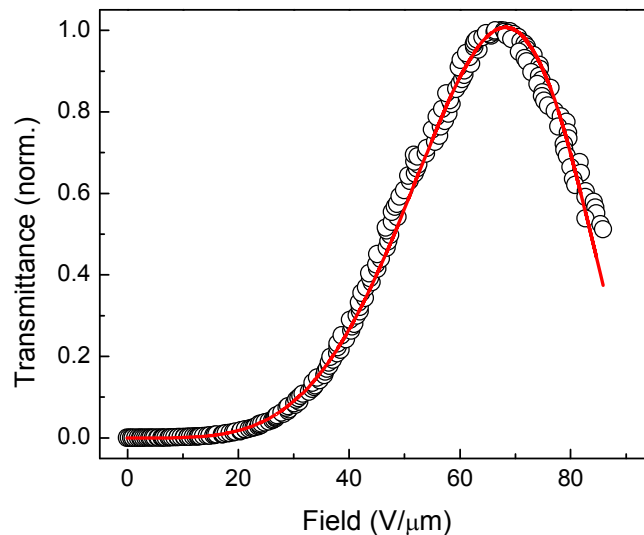


Figure 4-4: Typical experimental transmittance curve for ellipsometry data. The fit is based on quadratically varying index modulation.

Transient ellipsometry measurements help to clarify limiting factors in PR temporal performance by estimating the orientation speed of the chromophores. To probe rotational speeds below ms times, the high voltage source is required to have a fast switching time. The rise time (slew rate) for the current HV source (Matsusada) is $360\text{V}/\mu\text{s}$ or $22\mu\text{s}$ to reach 8kV . The detector is connected to an the oscilloscope and oscilloscope is triggered by the trigger output of the pulse generator. The pulse generator controls the output of the Matsusada high voltage amplifier. The compensator is used to set the output signal into the linear range. The scope trigger is armed, and the pulse generator is enabled. As the pulse generator sets the high-voltage supply, it triggers the scope, which acquires the signal. This signal provides the information desired about the

electro-optic transient response of the PR device. The rise of the transmitted signal is recorded as a function of time. Later in the analysis, the data is fitted to a bi-exponential function (see section 4.3.2.2).

4.3 Photorefractive Measurements

In this section, we will examine the means of determining the internal and external diffraction efficiency of PR gratings through four-wave mixing experiments and the beam-coupling gain by two-beam coupling observations. We will describe both steady-state and transient four-wave mixing methods which will allow observation of grating strength and dynamics in the state-of-the-art PR polymer devices.

4.3.1 *Sample Geometry*

The polymer film is sandwiched in between two glass plates partially-coated with indium-tin oxide (ITO) electrodes. The bias field is applied via the electrodes in a fixed direction.

In the slanted transmission geometry, the two writing beams are incident from one side of the sample. The sample's surface is tilted 60° (ψ) relative to the writing beam bisector. The writing beam angles are $\theta_1 = 50^\circ$ and $\theta_2 = 70^\circ$ in air. The same-wavelength readout beam counter-propagates with respect to the writing beam which makes a smaller angle with the sample surface normal. When the readout wavelength is different from the writing beams, the Bragg angle is deviated from counter-

propagation. In Figure 4-5, the wavelengths of writing beams are 532nm and 532nm or 633nm for reading.

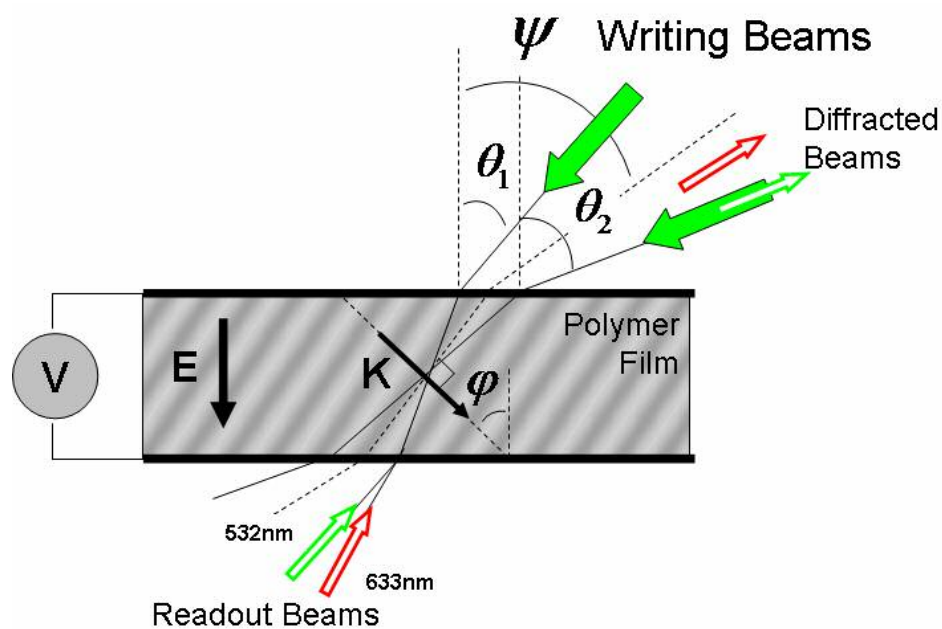


Figure 4-5: The slanted transmission geometry with 532nm writing beams and 532nm/633nm reading beams. Notice that, the Bragg-matched angle depends on reading wavelength.

In symmetric reflection geometry, each writing beam is incident on a different side of the sample. The sample normal is perpendicular to the writing beam bisector. The writing beams make an angle of 72° with respect to the sample normal.

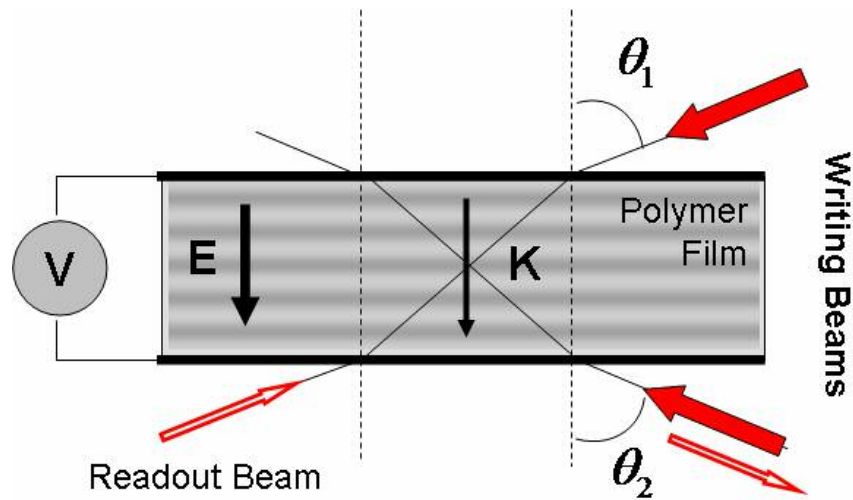


Figure 4-6: Symmetric reflection geometry

4.3.2 Four-Wave Mixing

In a four-wave mixing process, two strong writing (the summed intensities of the writing beams is typically $1\text{W}/\text{cm}^2$) beams are interfered to create a sinusoidal grating, while a weak third readout beam ($<1\%$ of writing beam intensity) probes the strength of the grating simultaneously. When the wavelengths of the writing beams and the readout beam are identical, the process is referred to degenerate four-wave mixing (DFWM) and the best efficiency is obtained when the readout beam counter-propagates with one of the writing beams. When the readout wavelength is different, it's called non-degenerate four-wave mixing (NFWM). In this case, the Bragg angle will be different from the degenerate case depending on the wavelength detuning. Four-wave mixing measurements are a critical part of material characterization. Using this experimental system, we can probe the exact diffraction efficiency and response time for a PR material. The system is

flexible to allow for measurements of other parameters such as spatial frequency dependence and Bragg angle sensitivity of gratings.

The current configuration of the four-wave mixing setup is modified slightly compared to its form several years ago. The probe beam is separated from the writing beams through a polarizing beam-splitter (PBS) component, instead of a pellicle beam splitter. A half-wave plate in front of the PBS component helps to adjust the relative ratio for read and write beams. Many different lasers (free-space or fiber-coupled) can be coupled into the same beam path as the He-Ne laser through insertion of a replaceable mirror, therefore the experimental system can be flexibly used at various wavelengths in the visible and near-infrared. Switching the system from visible to NIR, however, requires replacing some of the polarizing optics (PBS and NPBS). When a laser with a short coherence length such as a semiconductor laser is used, the path difference between the writing beams needs to be minimal. To ensure that, a delay line can be introduced into one of the writing beam paths and the other writing path can be adjusted.

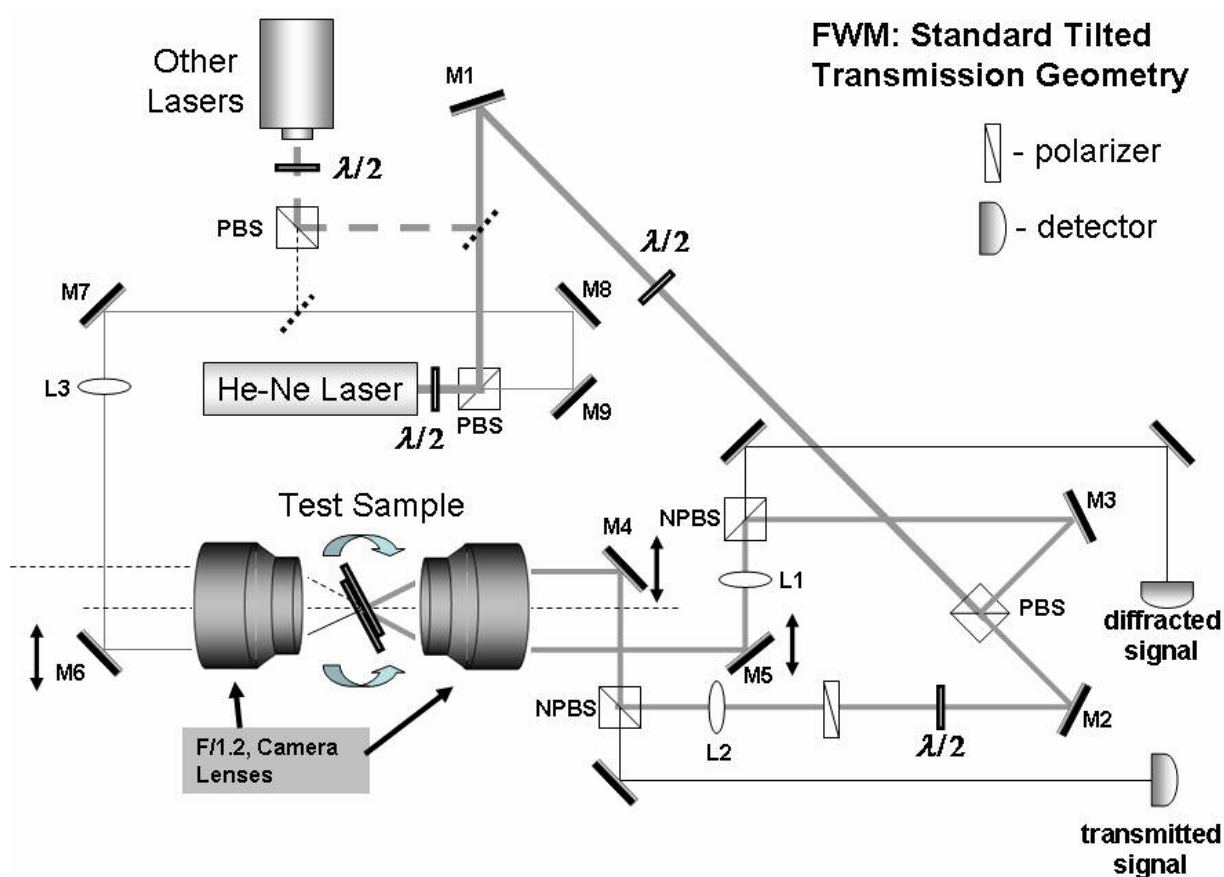


Figure 4-7: Experimental setup used in four-wave mixing and two-beam coupling experiments. Note that many different lasers can be coupled into this system, simply through a replaceable mirror.

The size of the beam at the sample position is adjusted through selection of lenses with appropriate focal lengths (L1 and L2). The focal length of the lens on the probe beam path (L3) is selected to be longer than L1 and L2, so that the readout beam will be smaller than the writing beams. M4 and M5 mirrors can be moved laterally to vary the angle between the writing beams. In the standard geometry, the separation between the two parallel writing beams is kept at 30mm. Considering the focal length of camera lens

(85mm), we have $\sim 20^\circ$ inter-beam angle for writing beams. In transient measurement case, a shutter or a Pockels cell is placed in one of the writing arms.

Even though the non-polarizing beam splitters (NPBS) in the system reduce the writing beam intensity by half, they are a necessary part of the system due to (1) separating counter-propagating beams and (2) providing polarization independent. The latter is a necessary factor for determining an accurate value for the diffraction efficiency. This is because, the PR materials become birefringent under the increasing bias field and therefore the diffracted or transmitted beams become elliptically polarized. A polarization independent beam splitter is insensitive to how birefringent the material will get.

4.3.2.1 Steady-State Diffraction Efficiency

This is the central test method for PR material evaluation. These tests are conducted by ramping up the bias voltage on the sample through small steps while detecting both the diffracted and the transmitted signal. This is generally done slowly (depends on the PR speed of the material) to provide steady-state values at each step in applied voltage. After each step in bias voltage, time is allowed for the lock-in amplifier measurement to settle. The use of a chopper for the readout beam and synchronous detection through the lock-in amplifiers provides better signal-to-noise ratio. The steady-state measurements are controlled by a computer program written in LabView. The bias is applied using a Glassman High Voltage source. The time constant settings of the lock-in amplifiers are set to a value which allows adequate time for settling after each step in voltage, while integrating over a long enough time to provide reasonable noise immunity.

After the sample is placed on the holder, the overlap of the writing beams is adjusted by moving the XYZ stage along the sample lens axis and across the sample lens axis. Once the writing beams appear overlapped in the film, the probe beam is adjusted to counter-propagate (in the DFWM case) with respect to one of the writing beam using the mirrors in the probe path. This can be set near enough to the optimized value to obtain a diffracted signal in most cases by checking the overlap of the probe and writing beam along a certain path. Finally, the signal level is optimized by applying appropriate bias to the sample and the final probe mirror angle is adjusted to obtain minimum transmitted and maximum diffracted signal. The probe mirror is first moved in the lateral direction to adjust the readout angle without moving the spot and then lateral and vertical angles are adjusted. The same cycle is repeated many times. Building FWM system with two fast lenses (F/1.2) provides not only a flexible system for a certain range of writing angles (therefore a certain range of spatial frequencies) and reduced spot size, but also helps to fine tune the reading angle to find the exact Bragg condition without moving the beam spot on the test sample (see Figure 4-8).

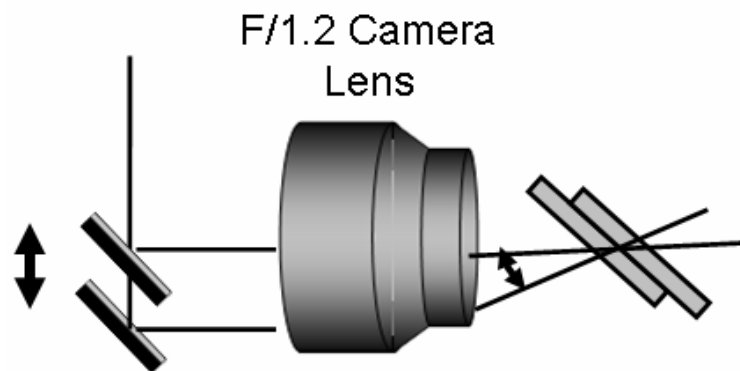


Figure 4-8: Adjusting the reading angle without moving the spot in the test sample. The fast camera lens helps to fine tune the Bragg-matched angle for best condition which will result in 100% diffraction efficiency.

After the readout angle adjustments, the setup is ready for steady-state measurements. The steady-state FWM characterization consists of monitoring the transmitted probe and diffracted probe signals as described briefly earlier. Generally, the writing beams are s-polarized, and the probe beam is p-polarized (preferred due to the geometry of material). This provides minimal interaction between the probe and writing beams and better efficiency. The data are analyzed to determine the diffraction efficiency by observing the depletion of the transmitted beam or comparing the detected signal on transmitted and diffracted beam detectors. The diffraction efficiency can be defined in two different ways: (1) internal and (2) external efficiency. The internal efficiency is simply the ratio of the diffracted probe energy to the total transmitted energy when there is no bias field:

$$\eta_{\text{int}} = I_D / I_T (V = 0) \quad (80)$$

This value does not include losses due to absorption, scattering, or reflections. In perfect Bragg-matched conditions, this value can be 100% and this is the efficiency that's referred to when a system is well-optimized. On the other hand and external efficiency is the ratio of the diffracted probe intensity to the incident intensity:

$$\eta_{ext} = I_D / I_{INC} \quad (81)$$

We generally consider the energy lost by the transmitted probe beam to estimate the internal diffraction efficiency, rather than directly measuring the diffracted intensity and normalizing it with transmitted intensity. But one should also double-check the signal from both detectors to validate the fact that the loss in the transmitted beam is gained by the diffracted one. This case is generally valid for thick holograms, where there is only one order of diffraction. However, one should pay attention in the case of thin holograms. Since the depletion in transmitted beam might also go into multiple other orders.

4.3.2.2 Transient Diffraction Efficiency

In these experiments, the grating formation process is observed at a constant applied bias as the PR process is initiated by turning on the writing beams. Usually, one beam is applied in advance, and then the second is applied as data acquisition proceeds. To resolve a few milliseconds, it is necessary to use a digitizing oscilloscope. The chopper is switched off and checked to make certain it does not block the probe beam. When the rise time of the grating is not very short (>5-10ms), switching one writing beam with a mechanical shutter is preferred due to its simplicity. The shutter opening time was a little less than 1ms and when isolated from the optical table, the vibrational and acoustic noises due to the shutter are minimized. For faster switching times, an electro-optic Pockels cell is more suitable. In the latter case, the Pockels cell needs to be placed in between a crossed polarizer-analyzer set.

The oscilloscope starts recording the data a little before the shutter opens. After the desired observation time, the shutter is closed. The delay time before the shutter opens, the observation time and the delay after the shutter closes can all be set through the LabView program. After, the data is transferred to the computer, the user is prompted to save the data.

The build-up of the phase grating is an important factor for determining the speed of PR gratings. For the Bragg-type holograms in transmission geometry, the efficiency is related to the index modulation as follows (see section 2.6.1):

$$\eta(t) \propto \sin^2 [B\Delta n(t)] \quad (82)$$

where B is a constant.

In the simplest single carrier model for photorefractivity, the transients for index modulation are exponential. However, in polymers the transients are usually non-exponential and must be fit to some other function. The time-dependant data are typically analyzed by fitting the refractive index modulation to a bi-exponential form:

$$\Delta n(t) \propto [1 - m \exp(-t/t_1) - (1 - m) \exp(-t/t_2)] \quad (83)$$

where t_1, t_2 are slow and fast time constants and m is the weighing factor. Often a stretched exponential form is used:

$$\Delta n(t) \propto \left\{ 1 - \exp \left[- (t/\tau_s)^\beta \right] \right\} \quad (84)$$

where, τ_s is the time constant and β ($0 < \beta < 1$) is a parameter that indicates how much the rate of increase slows down with time. The stretched exponential behavior can arise when a phenomenon depends on the convolution of a distribution of time constants⁸⁹,

which is often the case in inhomogeneous media such as polymer composites. The parameter β is related to the width of the time constant distribution, with β becoming smaller with increasing width.

For most of the transient data analysis, the data curves are fitted to a bi-exponential form and the early time constant (t_1) is reported.

4.3.3 *Two-Beam Coupling*

Two-beam coupling (TBC) experiments define interaction between two writing beams in a PR medium in such a way that an exchange of energy is observed between them. It is used to verify the PR nature of gratings observed in FWM, and it provides additional information for understanding the properties of composites. The experimental setup is the same as in the FWM setup shown above. The only difference is that since there is no probe beam present, the intensity values of each writing beam are recorded as a function of electric field. The relative energy levels of the writing beams can then be used to estimate the net gain of the material. Generally, the writing beams are p-polarized to obtain higher gain values compared to the s-polarized case. The data are analyzed to determine the gain coefficient by observing the energy exchange between the writing beams. The energy exchange is characterized by the ratio of each beam's intensity to its intensity in the absence of the other, often denoted by γ as shown:

$$\begin{aligned}\gamma_1 &= \frac{I_1(z)(I_2 \neq 0)}{I_1(z)(I_2 = 0)} \\ \gamma_2 &= \frac{I_2(z)(I_1 \neq 0)}{I_2(z)(I_1 = 0)}\end{aligned}\tag{85}$$

The denominator quantities are obtained by conducting scans like two-beam coupling runs with each beam blocked in turn. Having obtained these curves, the combined gain coefficient value may be calculated using the following equation:

$$\Gamma = \frac{1}{d} [\cos \alpha_1 \ln \gamma_1 - \cos \alpha_2 \ln \gamma_2]\tag{86}$$

where d is the sample thickness and α_1, α_2 are the angles of the two beams with respect to the sample normal inside the PR film.

The direction of the applied electric field defines the direction of energy transfer. Reversing the bias changes the sense of energy transfer. The extent to which the transfer is symmetrical with the reversal of bias may be important. In the case of high gain materials, for example, a phenomenon known as beam-fanning may occur. This is a field-dependent process whereby scattered light beams within a sample are amplified by the same coupling process we are discussing. The process is not symmetrical for the slanted geometries used in PR polymers devices, and is a parasitic process in most cases. It may lead to mistaken estimates for the gain coefficient, which warrants some awareness of it.

In the transient TBC case, one of the writing beams is switched on and the amplification or the attenuation of the other writing beam is monitored as a function of time. Since the gain is directly proportional to the index modulation either bi-exponential or stretched exponential functions are used to fit the rise of γ .

5 RESULTS AND DISCUSSIONS

Having discussed the theory for the photorefractive (PR) effect, materials and characterization techniques, we will now present the several new contributions to this research field from the author and his colleagues. By the beginning of the author's work, thin film devices of low-glass transition PR polymer composites has already reached 100% diffraction efficiencies⁹⁰, millisecond response times^{91,92} and has been proven to be sensitive to wavelengths in the visible and somewhat in the near-infrared.⁹³ Net gain coefficients of more than 400 cm^{-1} were readily achievable.⁹⁴ Organic PR materials were attractive, because they offer the advantages of low-cost, ease of fabrication, tunability over the properties as well as large optical nonlinearities compared to their inorganic counterparts.^{20,95} The shelf lifetimes of composites could be extended into many years. However, there were still a number of avenues open to research. First, the PR devices were required to have high bias voltages for high performance operation; lower bias voltages would be more practical. Second, there are many applications at NIR wavelengths where both sensitivity and performance of the past organic PR materials were lacking; new material approaches were required to address this problem. Third, the response time of organic materials has been limited to 1-4 ms; innovative experimental approaches instead of material modifications were required to achieve submillisecond writing times, single-pulse exposure is the demonstrated method. Fourth, the holograms recorded in organic PR materials usually decay rapidly; new approaches such as thermal fixing has been used to improve persistence of gratings. Fifth, we have opened a new

venue in understanding the behavior of low-glass transition PR composites in the reflection geometry and analyzed the material behavior in that configuration.

5.1 Reducing the Bias Voltage in Photorefractive Polymers

In this study,⁹⁶ the high-voltage bias required for video-rate compatible efficient operation of a PR polymer composite was reduced to 1.3 kV. At this low voltage, the device holds rewriteable Bragg holograms with 80% efficiency in addition to its video-rate response time. The transition of the hologram regime from thick to thin was carefully analyzed.

One of the limitations of high performance organic materials for direct practical applications is the necessity for high bias voltages (5–10 kV for a typical 100 μ m thick sample). The high voltage is necessary for orienting nonlinear molecules, separating the charges, and facilitating their transport in the matrix because of the low conductivity and mobility of organic materials. Several materials such as amorphous organic glasses²⁰ and polymer dispersed liquid crystals have recently been employed to reduce the required bias voltages⁸¹. For amorphous glasses, the operating voltage has been reduced but the response time is much longer, of the order of seconds.²⁰ The drawbacks of polymer-dispersed liquid crystals are high degree of scattering and slow response times.⁸¹ Here we present both a material and a device approach to reduce the operation voltage of a PR polymer to the 1 kV level without sacrificing high diffraction efficiency and fast response time.

5.1.1 *Mixture of Chromophores*

In guest–host PR polymer systems, one can enhance the effective index modulation by doping the matrix with a larger amount of polar, nonlinear optical molecules called chromophores and reducing the glass-transition temperature by adding more of a suitable plasticizer agent. However, loading of large amounts of polar molecules can cause potential disadvantages such as phase separation, crystallization, and reduced mobility. The chromophore mixture approach can provide large birefringence without resulting in phase separation. Increasing the plasticizer content, however, will increase the inert volume, therefore worsening the dynamic properties.

5.1.2 *Reducing the Thickness*

One can investigate a thin PR device at or near minimal Bragg requirement conditions. As stated in Kogelnik’s groundbreaking paper,⁷⁷ the Q factor can be used to differentiate Bragg (one diffracted order at Bragg incidence) from Raman-Nath (multiple diffracted orders) regime:

$$Q = 2\pi\lambda d / n\Lambda^2 \quad (87)$$

where λ is the vacuum wavelength, d the thickness of the film, n the mean refractive index and Λ the grating spacing. Bragg diffraction requires the condition $Q \gg 1$. One can adjust the thickness and grating spacing values but still keep the Q value above 1 to take the advantage of high Bragg diffraction efficiency.

The diffraction efficiency itself is a function of thickness and bias voltage as well. The simplified form of the diffraction efficiency in slanted transmission geometry can be written as,⁷⁷

$$\eta \propto \sin^2 \left[\frac{\pi \Delta n(E) d}{\lambda (\cos \alpha_1 \cos \alpha_2)^{1/2}} \right] \quad (88)$$

$$\Delta n \propto E E_{sc} \propto (E)^P = (V/d)^P \quad (89)$$

where d is the thickness of the film, λ the wavelength and α_1 and α_2 writing beam angles in the polymer, E_{sc} space-charge field and V the bias voltage. The index modulation (Δn) has a power law dependence with the field, where $P \sim 1.9 - 2.0$ (when there is enough traps in the system). Additionally, Δn depends on the grating spacing through a sublinear relationship.

To get the same diffraction efficiency from both 105 μm and 20 μm devices, one should apply voltages with a ratio of $V_{105\mu\text{m}}/V_{20\mu\text{m}} = (d_{105\mu\text{m}}/d_{20\mu\text{m}})^{(p-1)/p} \approx 2.3$. This reduction in the thickness will bring the operating voltage from a typical 3kV level to $\sim 1.3\text{kV}$ (or 65V/ μm) level. At the same time, since the operating field is larger than that of 105 μm -thick case (30V/ μm), the device will have faster dynamics.

5.1.3 Material and Characterization

We have applied the principle described above to reduce the effective voltage requirement for high-performance operation of a polymer PR device. The composite is based on a hole-transport polymer (PATPD) which has a polyacrylate backbone and a well-known hole-transporting tetraphenyldiaminobiphenyl type (TPD) pendant group

attached through an alkoxy linker.⁹⁷ The hole transporter PATPD was doped with a mixture of two NLO chromophores 4-homopiperidinobenzylidenemalononitrile (7DCST) and (N,N-di-n-butylaniline-4-yl)-1-dicyanomethylidene-2 cyclohexene (DBDC) , with C₆₀ as a sensitizer for charge generation at the operating wavelength of 633nm and the plasticizer, N-ethyl carbazole (ECZ) . The mixture of chromophores approach is followed due to better phase stability. Composites prepared included PATPD:DBDC:7-DCST:ECZ:C₆₀ (39.3:40:10:10:0.7 wt. %). Samples were prepared by laminating 20 μ m and 105 μ m thick layers between glass slides with indium-tin-oxide (ITO) electrodes. The absorption coefficient of the film was measured to be 70 cm⁻¹ at 633nm.

To characterize the PR properties of the samples, degenerate four-wave mixing experiments were performed in the standard slanted sample geometry. Two interfering *s*-polarized beams (633nm) of equal fluence (0.5 W/cm² each) were used to write the grating and a weak counter-propagating *p*-polarized beam probed the efficiency of the grating. The writing beams were incident on the sample with an inter-beam angle of 20⁰ in air and the sample surface was tilted 60⁰ relative to the writing beam bisector resulting in a grating period of 3.1 μ m. Under these conditions the Kogelnik's Q value, based on Equation (87) is calculated to be 4.7, which is still in the Bragg (thick) hologram regime. Figure 5-1 shows the percentage of diffracted probe beam as a function of the applied external field under steady-state conditions for 20 μ m and 105 μ m thick devices. The external efficiency (when reflection and absorption losses are included) of the device was 58%. Using the present approach, we were able to reduce the voltage required for

overmodulation (peak of diffraction efficiency) of diffraction efficiency by a factor of 4 compared to a single chromophore containing composite reported earlier.⁹⁷

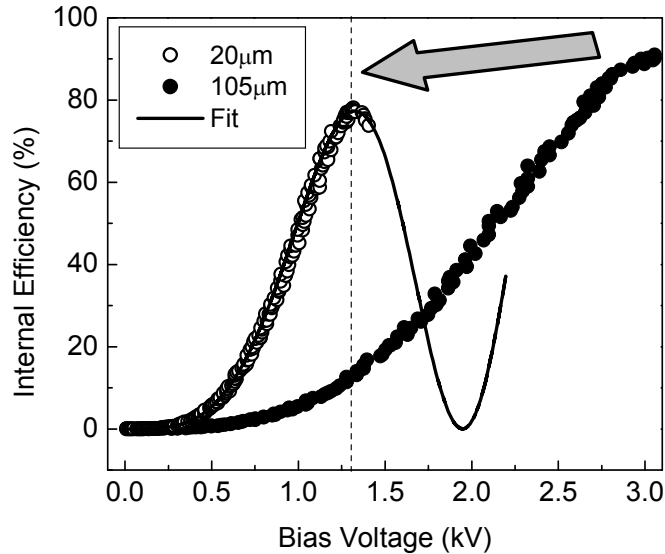


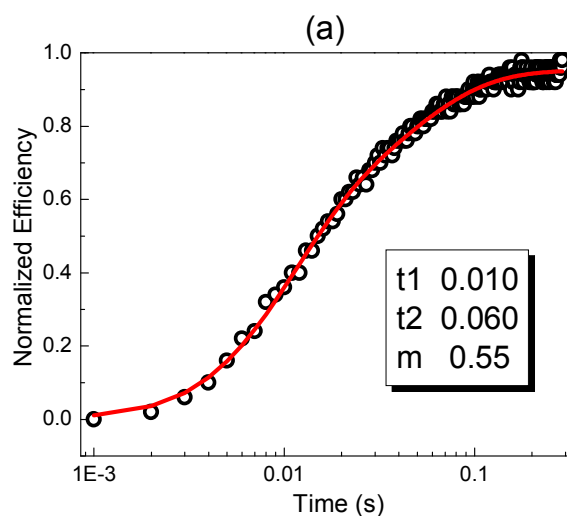
Figure 5-1: Steady-state diffraction efficiency for both 20 μm and 105μm thick devices, as the bias voltage is increased. The peak internal diffraction efficiency of the 20 μm device was 80%. External efficiency was around 58%, which is higher than a similar thick device, due to the low absorption of the thin device.

The dynamics of the index modulation built-up can be extracted from a bi-exponential function fit that is correlated with the growth of the space charge field:

$$\Delta n \propto A[1 - m \exp(-t/t_1) - (1-m) \exp(-t/t_2)] \quad (90)$$

here A is a constant, m a weighing factor, t_1 and t_2 time constants. Figure 5-2a shows the evolution of the diffraction efficiency after switching on the second writing beam at time

$t=0$. The line represents the fit to the data. Remarkably fast dynamics with a characteristic first time constant of 10 ms (at 1.4kV bias voltage) is observed indicating possible application of these composites in systems that operate at video rates. To test the performance of current devices for video-rate compatibility, one of the writing beams is modulated at 1-30Hz full-cycle (on and off) frequency (Figure 5-2b). The efficiency has only dropped to half of its cw value at 30Hz. Therefore, this device can simply operate with high efficiency and video-rate refresh rates without requiring impractical bias voltages.



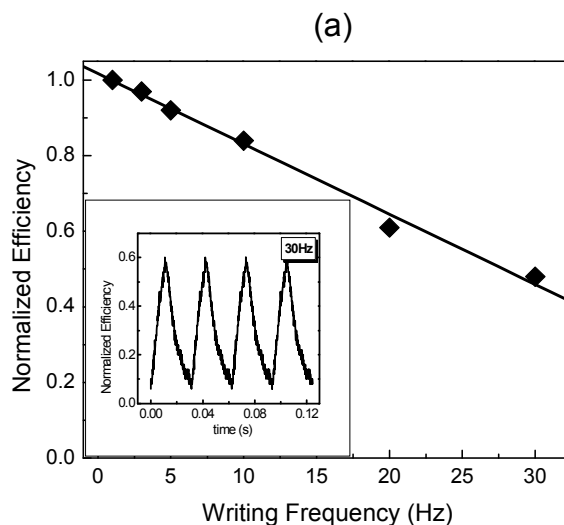


Figure 5-2: (a) Typical growth of diffraction efficiency when one of the writing beams is switched on. The line is a biexponential fit. The total writing beam irradiance was $1\text{W}/\text{cm}^2$ and a bias voltage of 1.4 kV was applied through the device. (b) The net diffraction efficiency is recorded as one writing beam is modulated at 1-30Hz (full cycle write and erase) frequency. The inset shows the response of the photorefractive device at a 30Hz frame rate.

The transition from the thick (Bragg) to thin (Raman-Nath) hologram regime is not sharp. Higher diffraction orders are strong when $Q \ll 1$ (Raman-Nath regime). In this regime, the maximum diffraction efficiency possible for the first order is 34%.⁷⁶ When one varies the grating spacing to change the Q value through the transition region, the peak efficiency starts to drop gradually (Figure 5-3). There were no visible higher orders below $3.5\mu\text{m}$ grating spacing. Above that, higher orders started to become visible. Above $5.2\mu\text{m}$, the higher orders became even stronger and contributed to more than a

50% reduction in the strength of the first order diffracted beam. The overmodulation field is simply shifted due to the increased grating spacing which can be explained through the Kukharev model.⁶⁴ The index modulation (amplitude of sinusoidal modulation of index) was calculated to be $0.012-0.018$, increasing with the grating spacing. When the index modulation is large, the regime of the grating can be reliably specified if the parameter ρ (first defined by Nath) is utilized.⁷⁸ It is defined as $\lambda^2 / \Lambda^2 n \Delta n_1$, where Δn_1 is the index modulation. Based on this parameter, the Raman-Nath regime necessitates $\rho \leq 1$. At a grating spacing of $3.1\mu\text{m}$, $\rho=2$ and at $5.2\mu\text{m}$, $\rho=0.5$, in agreement with our experimental results.

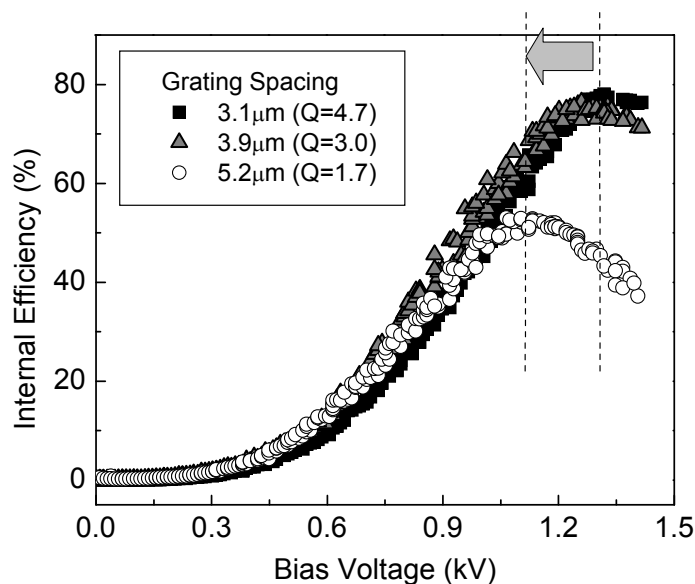


Figure 5-3: The drop of peak efficiency as the state of the hologram is changed from thick (Bragg) to thin (Raman-Nath). The grating spacing is increased to vary the

Kogelnik's Q value. The shift in the peak efficiency reveals the growth in index modulation with increased grating spacing.

Note that, the PR nature of the hologram was confirmed through two-beam coupling measurements.⁹⁸ In the case of equal intensity writing beams, the net gain, Γ was more than 400cm^{-1} at 1.3kV.

In summary, we have reduced the high bias voltage required for the operation of guest-host PR polymers to 1kV level. This is accomplished by doping the PR composite with two NLO chromophores and successfully reducing the device thickness to the minimum Bragg condition. The current device can be operated at low voltages maintaining the video-rate response time. Even some useful diffraction efficiency of 20% can be achieved at a practical voltage of 750V. The PR behavior of device has been characterized in the transition region between thin and thick holograms.

5.2 Photorefractive Polymers Operating at NIR Wavelengths

In recent years, several impressive PR properties have been reported for applications in the visible and infrared regions.^{20,37} Much less consideration has been given to the infrared region mainly due to the unavailability of composites with favourable PR properties that operate within this spectral range. On the other hand, this wavelength range is of major importance, e.g. for medical imaging and optical communications, and compact solid state lasers are readily available. In a recent report on PR composites inorganic semiconductor nanocrystals are used to achieve sensitization at

1310 nm;⁹⁹ but the response time in these hybrid materials are usually slow and diffraction efficiency is lower¹⁰⁰ compared to all-organic composites.

5.2.1 975nm

We have demonstrated²² proof of photorefractivity at 975nm in an all-organic composite with a performance comparable to and possibly faster than the current organic materials at infrared wavelengths^{21,101,102}; a significant step towards organic PR devices at a new infrared wavelength.

We focused our attention on a composite based on PATPD polymer. The hole transporter, PATPD was doped with a nonlinear optical (NLO) chromophore 7-DCST and a near infrared dye, DBM (Figure 5-4) for charge generation at the operating wavelength. Composites prepared include PATPD/7-DCST/ECZ/DBM (54/25/20/1 wt. %) (C1) and PATPD/7-DCST/ECZ/DBM (49/35/15/1 wt. %) (C2). C1 was phase-stable for more than six months at room temperature, while in C2 crystallization was observed after a few weeks. Samples of both composites were prepared by laminating 105 μ m thick layers between glass slides with ITO electrodes. The absorption spectrum around the excitation wavelength and the chemical structure of DBM dye are shown in Figure 5-4. The amount of sensitizer is adjusted to have adequate photosensitivity, yet so as not to reduce the mobility and carrier lifetime due to increased trap density.

A large ratio of photoconductivity σ_{ph} to background conductivity σ_{dark} is very beneficial in PR materials since majority carriers can easily move from the high intensity regions to the low intensity regions and get trapped leading to the formation of stronger

internal space-charge fields. At low illumination the ratio between σ_{ph} and σ_{dark} limits the strength of the space-charge field via the pre-factor $\sigma_{\text{ph}}/(\sigma_{\text{dark}} + \sigma_{\text{ph}})$. Figure 5-4 (inset) shows the photoconductivity of the composites measured during illumination with 975nm light. We accounted for the light intensity attenuation due to finite sample thickness and normalized the data with respect to the absorbed light intensity.¹⁰³ This normalized photoconductivity also reflects the magnitude of photogeneration, carrier mobility and lifetime. At an intensity level of 1 W/cm² and an applied field of 56 V/ μm , the normalized photoconductivity of 1000 pS/cm (C1) is 5 orders of magnitude larger than the dark conductivity.

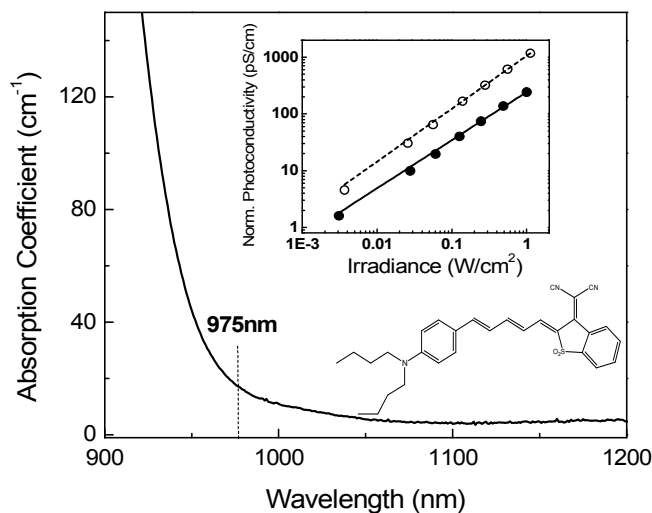


Figure 5-4: Absorption spectrum of the dye is shown near the wavelength under consideration. Chemical structure of the sensitizing dye is also shown. Close to

linear intensity dependence [$\sigma \sim I^{0.93}$ (C1, open circles) and $\sigma \sim I^{0.85}$ (C2, dark circles)] of the photoconductivity is observed at an electric field of 56 V/ μm (inset).

Another crucial parameter for high-performance PR materials is the refractive index modulation which is primarily due to chromophore orientation (in low- T_g materials). With an applied electric field, the orientation of the NLO chromophores results in birefringence that has been measured by an ellipsometric technique.^{104,105} The birefringence was observed to be 0.0012 (C1) and 0.0055 (C2) at an electric field of 76 V/ μm . The relatively low index modulation in C1 is expected due to low loading of the NLO chromophore (25%). To characterize the PR properties written in the samples, FWM experiments were performed in slanted transmission geometry. Two interfering s-polarized beams of equal fluences (0.5 W/cm² each) were used to write the grating and a weak counter-propagating p-polarized beam (3 mW/cm²) was used as the probe beam. The writing beams were incident on the sample at an interbeam angle of 22.5⁰ in the air and the sample surface was tilted 60⁰ relative to the writing beam bisector resulting in a grating period of 4.3 μm . Figure 5-5 shows the percentage of diffracted probe beam as a function of the applied external field under stationary conditions. The internal diffraction efficiency increases to a maximum value of 35% at 95V/ μm for 105 μm thick films without reaching an overmodulation, i.e. a diffraction maximum followed by a successive decrease in diffraction efficiency. This somewhat limited diffraction efficiency in C1 is again caused by the rather low chromophore loading (25%) and the correspondingly small refractive index modulation (see Table 5-1). Furthermore, from the Kogelnik's equation⁷⁷ for diffraction efficiency,

$$\eta \propto \sin^2 \left[\frac{\pi \cdot \Delta n(E) \cdot d}{\lambda (c_R \cdot c_S)^{1/2}} \right] \quad (91)$$

It is clear that at longer wavelengths overmodulation occurs at larger index contrasts. Here Δn is the field dependent index modulation, d thickness of the film, c_R and c_S are geometrical factors. In sample C2, the larger chromophore content (35 wt. %) proved sufficient to reach overmodulation with a maximum in diffraction efficiency of 60% just below 95 V/ μm . On the other hand, index modulation can be limited by the trap density which affects the strength of the space charge field. The field dependence of η can give an estimate of the effective trap density. A reasonable fit of the data to the theory⁶⁴ (Figure 5-5) gives a trap density of $2.3 \times 10^{16} \text{ cm}^{-3}$. This low density clearly proves that the present composites are in the trap-limited regime; further traps are needed for better performance.

Note that, in a well-optimized FWM system, 100% internal efficiency can easily be achieved. If the efficiency measured is below this value, one should also check that the coherence properties of the laser are good enough to provide reasonable contrast of fringes. After these initial measurements, we have realized that the coherence properties of 975nm laser weren't good enough. A fiber Bragg grating was spliced to the output side of the laser to provide a feedback at a reference narrow wavelength, locking the laser to that wavelength. Later, in the measurements, we were able to achieve 100% diffraction efficiency with the same sample.

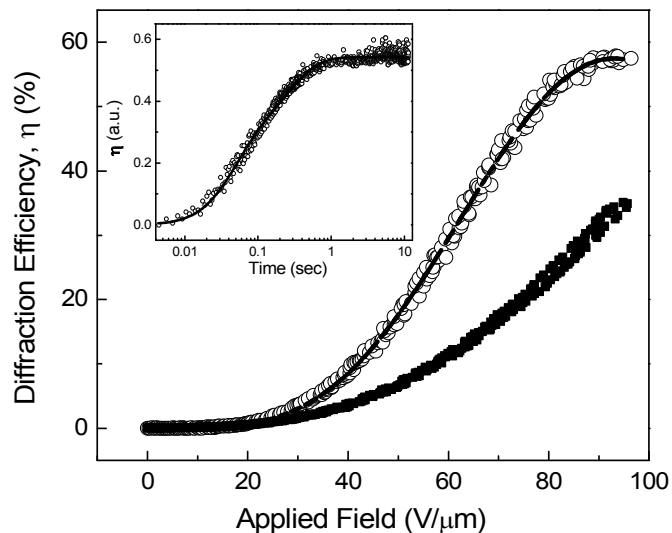


Figure 5-5: Steady-state diffraction efficiency vs external electric field for both C2 (open circles) and C1 (dark squares); the solid line is a theoretical fit for a trap density of $2.3 \times 10^{16} \text{ cm}^{-3}$. Transient growth of the diffraction efficiency as the second writing beam is turned on for C2 is shown in the inset. The solid line in the inset is a bi-exponential growth fit ($\tau_1=33\text{ms}$, $\tau_2=320\text{ms}$, weight factor $m=0.5$).

The dynamics of the grating built-up can be extracted from a bi-exponential function fit that is correlated to the growth of the space charge field (see Section 4.3.2). The Figure 5-5 inset shows the evolution of the diffraction efficiency after switching on the second writing beam at time $t=0$ for C2. The line represents the fit to the data. Remarkably fast dynamics with characteristic time constants of 96 ms for C1 and 33 ms for C2 are observed indicating possible application of these composites in systems that operate at or close to video rates. In sample C2 these dynamics were observed at a field

close to the peak of the diffraction efficiency (overmodulation point). Please note that this was not possible for sample C1 and, therefore, the data for this sample might not be directly compared with the grating dynamics reported in other materials.

Composite	$\sigma_{\text{photo}} / \sigma_{\text{dark}}$ [pS/cm]	Δn @76 V/ μm	Max η_{diff} (Internal)[%]	τ_1 [ms]	Speed [s ⁻¹]	τ_g^{-1} [s ⁻¹]	Γ @76 V/ μm [cm ⁻¹]
C1	1000 / 0.02	0.0012	35%	96	0.5	0.9	60
C2	240 / 0.06	0.0055	60%	33	5.7	11	110

Table 5-1: Summary table for C1 and C2. Conductivity values given are at 56V/ μm applied field and 1W/cm² intensity. Diffraction efficiencies and response times are measured at 95V/ μm . Speed is determined from $[mt_1+(1-m)t_2]^{-1}$. τ_g is the time constant from the stretched exponential fit (see Section 4.3.2).

The unique nonlocal nature of PR gratings was demonstrated by a two beam coupling experiment which is considered to be the signature of photorefractivity in new materials.⁹⁸ We adopted the same slanted sample geometry with only p-polarized writing beams in a 1:1 ratio providing a total fluence of 1 W/cm². As shown in the Figure 5-6, net gain can easily be obtained for both samples. This measurement not only demonstrates the PR nature of the light induced gratings, but also opens the door for applications where continuous redirection of energy between light beams is needed.

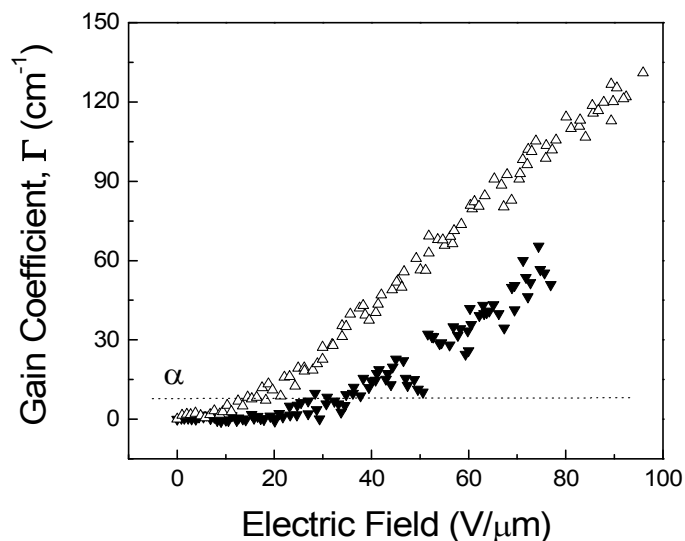


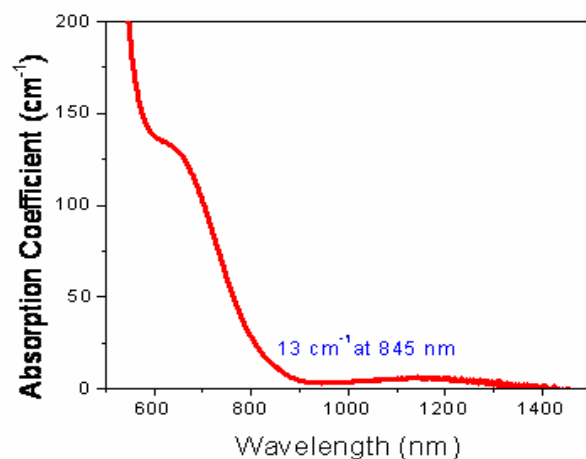
Figure 5-6: The electric field dependence of the two beam coupling gain coefficient of C2 (open triangles) and C1 (dark triangles) for p-polarized writing beams. The absorption coefficient $\alpha=13 \text{ cm}^{-1}$ is included for comparison.

In summary, we have demonstrated high-performance of novel PR polymer composites at 975nm. PR gratings can be written within tens of milliseconds, diffraction efficiency from these gratings reaches 60 % and a two-beam coupling gain of 130 cm^{-1} can be observed. The large photoconductivity validates the possibility of achieving even faster response times within this family of polymer composites. Extending the sensitization of an all organic PR device to the wavelength of almost $1 \mu\text{m}$ represents a significant advance to the development of all-organic PR devices for infrared imaging and optical communication. Further research will focus on increasing the refractive index modulation, improving the response time as well as shelf life time of these materials, and further extending the range of operating wavelength into the infrared region.

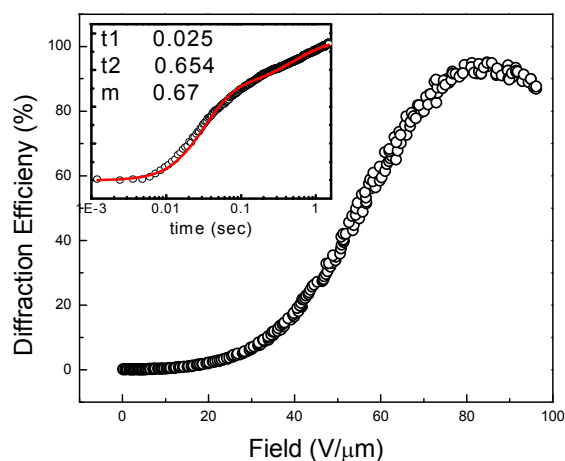
5.2.2 845nm

The wavelength region where the biological tissues are transparent and the atmospheric transmission is higher (700-900nm) has many potential applications for rewritable holographic materials.^{21,37} The organic PR materials have proven to be fast and efficient recording media in the visible window of the spectrum. However, until recently, the organic materials were lack of a good sensitivity that will make the potential applications more feasible. The recording time was long, below video-rate speed.³⁷ Recently, a work published by Mecher et al²¹ in Nature has proved that a good sensitivity can be achieved through gated illumination using a poly(arylene vinylene) copolymer (TPD-PPV) based composite. However, achieving high speed by pre-illumination can be a limitation in real time practical applications.

We have also developed an efficient device operating at 845nm with video-rate response time without the help of pre-illumination. Our device has the necessary absorption for the PR process and the gratings recorded in the material showed almost 100% diffraction efficiency with a recording speed at video-rate (see Figure 5-7). The material is based on PATPD/TNFDM with a composition of PATPD:7-DCST:ECZ:TNFDM (52:35:12:3 wt%). The sensitization at near-infrared wavelengths is believed to be due to the charge-transfer complex between PATPD and TNFDM.



(a)



(b)

Figure 5-7: (a) The absorption spectra of the sample sensitive at 845nm, (b) the transient response (inset) and steady-state diffraction efficiency curves

It is evident that even without pre-illumination, the 845-nm sensitive PR composite shows near-video rate response (25ms response time) with high diffraction efficiency ($\sim 100\%$) at an irradiance of $0.8\text{W}/\text{cm}^2$ and bias field of $80\text{V}/\mu\text{m}$.

5.3 Single-Pulse Gratings in Photorefractive Polymers

Individual nanosecond pulses can be used to record gratings in a PR composite. In this study,¹⁰⁶ a single pulse with 4 mJ/cm^2 energy recorded a grating with 56% diffraction efficiency and a build-up time constant of only $300 \mu\text{s}$ (t_1) demonstrating one-order of magnitude faster recording compared to writing with continuous wave beams. This fast response enables applications in optical processing requiring frame rates of 100Hz or more. Due to the short duration of the writing pulses, the recording is insensitive to vibrations.

Even though some applications necessitate fast recording speeds, the fastest organic PR materials reported so far show response times in the millisecond range.^{91,92,107} The origin of this limit can be attributed to charge-carrier generation and transport and the reorientation of the nonlinear-optical chromophores.²⁰ Selecting transport matrices with drift mobilities more than two orders of magnitude higher than poly(*n*-vinylcarbazole) (PVK) improved the response time by only several times.¹⁰⁷ Depending on the type of composite, the orientation of chromophores can have some or no limitation at all on reducing the speed.²⁰ A complementary approach like light-induced filling of the traps^{21,108} have been used to improve the speed as well. One can also speed up the charge-carrier generation through writing with a single-shot pulse, like in holographic time of flight (HTOF) experiments.⁶⁰ In this work, we report that a single nanosecond pulse can create sufficient charge carriers in a short time which can significantly improve the response time while showing large diffraction efficiency.

5.3.1 *Material Approach*

We have carefully selected the functional elements of this composite for the purpose of fast writing and decay. The hole-transport polymer PATPD was chosen, because it has a relatively large mobility and the ionization potential (I_p) for this polymer is lower than the other components added into it.⁹⁷ In this way, the deep trap density was kept to be minimum to achieve larger drift mobility. The existing shallow traps are believed to be due conformational disorder. In addition to the transport polymer, a rapidly orienting nonlinear optical chromophore 7-DCST is selected due to its fast orientation in several hundred microseconds. The system also includes the plasticizer ECZ and an efficient sensitizer C_{60} . A similar type of composite has been reported in our earlier work.⁹⁷ In the present case, the chromophore concentration is reduced for better transparency at the recording wavelength of 532nm. The composite consisted of PATPD: 7-DCST: ECZ: C_{60} (54.5:25:20:0.5 wt. %). The material was sandwiched in between two pieces of indium-tin-oxide (ITO) coated glasses and the thickness of the film was 105 μ m. The absorption coefficient of the composite was measured to be 104cm⁻¹ at 532nm and 30cm⁻¹ at 633nm.

5.3.2 *Reading PR grating through 532nm and 633nm wavelengths*

To characterize the PR properties of the samples, both degenerate (D) and non-degenerate (ND) four-wave mixing (FWM) experiments were performed in the slanted sample geometry. Two interfering *s*-polarized beams (532nm) with a total pulse fluence of 4mJ/cm² and 1ns pulse-width created the grating. A counter-propagating *p*-polarized

cw beam (532nm, DFWM) or a slightly-deviated cw beam (633nm, NDFWM) probed the efficiency of the grating (Figure 5-8). The writing beams were incident on the sample with an inter-beam angle of 20° in air and the sample normal was tilted 60° relative to the writing beam bisector resulting in a grating period of $2.6 \mu\text{m}$. When read out at 633nm, the probe beam was deviated from the counter-propagating angle to satisfy the Bragg condition. Reading with the red beam is preferred, due to lower absorption of the film at longer wavelengths.

Under steady-state continuous wave (cw) 532nm writing conditions, the peak of the diffraction efficiency (overmodulation) is reached at larger fields for the red reading case compared to the green reading case. This difference can simply be attributed to the inverse wavelength factor in the formula for diffraction efficiency in thick holograms derived by Kogelnik:⁷⁷

$$\eta \propto \sin^2 \left[\frac{\pi \Delta n d}{\lambda \sqrt{\cos \alpha_i \cos \alpha_d}} \right] \quad (92)$$

where Δn is the index modulation, d the thickness of the film, λ the probe wavelength and α_i and α_d the angles for the incident and diffracted beams in the material. For red reading, in addition to different wavelength, the incident and diffracted angles are slightly smaller than in the green reading case. Therefore, for red reading the index modulation has to be larger (more field required) to reach the peak efficiency. For cw recording, large internal diffraction efficiencies of 85-95% can be obtained for both red and green reading and the time constant of the fast transient response was $\sim 4\text{ms}$ at 1.2 W/cm^2 (or $\sim 4.8\text{mJ/cm}^2$) irradiance.

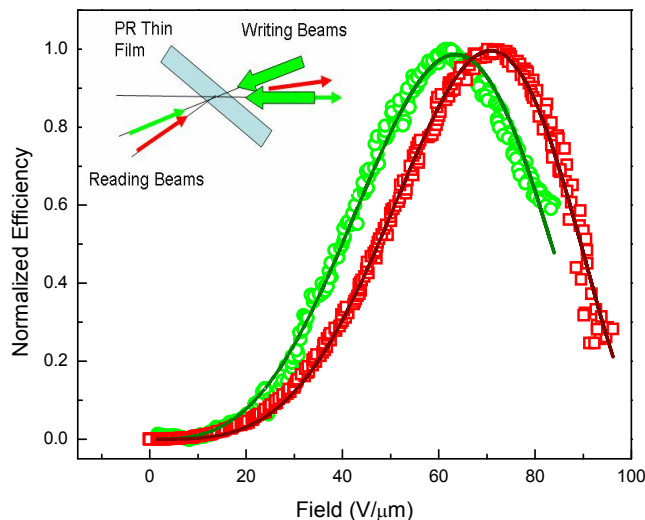


Figure 5-8: The steady-state diffraction efficiency when read through green (circles) and red (square) beams. The slanted transmission geometry used in the writing process is shown in the inset. The red reading beam comes in a slightly different angle to achieve the Bragg condition. The peak of the efficiency is reached at different fields for different reading wavelengths.

5.3.3 Submillisecond Response

In the case of single pulse exposure, the two writing beams create a light grating for the duration of the pulsewidth which is ~ 1 ns, in our case. The recording is almost instantaneous and eliminates the unwanted effects of mechanical vibration in the system. The maximum diffraction efficiency, on the other hand, is reached after ~ 1 -2 ms due to the slow hopping charge transport mechanism that takes place in polymers as well as chromophore orientation. A maximum of 56% internal or 35% external (after all losses)

diffraction efficiency is observed. Rise and decay of the diffracted signal is depicted in Figure 5-9. The readout wavelength was 633nm and the bias field was at 95V/ μm . The temporal characteristics of the space-charge field as well as the index modulation can be extracted by fitting the data to an exponential function with 4 different time constants (2 for rise and 2 for decay):

$$\Delta n \propto [1 - m_1 \exp(-t/t_1) - (1 - m_1) \exp(-t/t_2)] \cdot [m_2 \exp(-t/t_3) + (1 - m_2) \exp(-t/t_4)] \quad (93)$$

$$\eta \propto \sin^2 [B \Delta n] \quad (94)$$

Here, m_1, m_2 are weighing factors, t_1, t_2 and t_3, t_4 time constants for rise and decay, respectively, and B a constant. From the fitted curve we find the fast rise time constant (t_1) to be 300 μs with a weighting factor (m_1) of 0.54, which is one order of magnitude less than the shortest time constants reported earlier.^{91,92,107} In HTOF experiment, a shorter response time has been observed, however the observed efficiency was very low.¹⁰⁸ When the rise and decay portions of the data are separated and fit to the commonly-used bi-exponential function, we still obtain very similar values for the time constants.

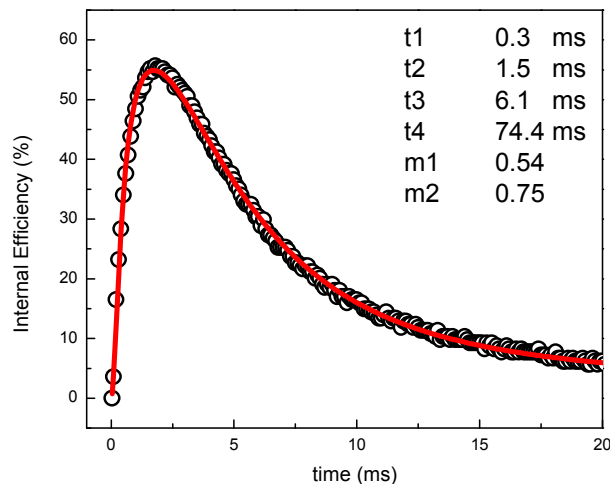


Figure 5-9: The fast rise and decay of diffraction efficiency of PATPD: 7-DCST: ECZ: C₆₀ (54.5:25:20:0.5 wt. %) when exposed to two interfering single pulses of 1 ns pulsewidth with total 4mJ/cm² fluence. The bias field was kept at 95V/μm and the reading beam wavelength was at 633nm. The internal efficiency reached a maximum of 56% (or 35% efficiency after all losses) in only 1.8ms time. The fast time constant for the rise section of the curve is 300μs. The line is an exponential fit function with four time constants (2 for the rise and 2 for the decay).

The pulse energy defines the number of carriers that can be generated in the material. Note that since charge generation is through linear absorption process, the peak power of the pulse doesn't contribute to the PR effect, but the pulse energy does. Nanosecond pulses with different pulsewidths will show the same PR response if their pulse energies are the same. An irradiance of 4mJ/cm² in 105μm-thick film corresponds to 10¹⁸ photons/cm³, more than half of which are being absorbed. The quantum

efficiency, trapping and recombination rate will reduce the total density of trapped charges. For pulse energies of 0.4-3 mJ/cm² the maximum diffraction efficiency is linearly related to the pulse fluence (Figure 5-10). Varying the pulse energy improves the recording time only very slightly. This can be attributed to the fact that speed is limited by mobility and possibly chromophore orientation, not charge-carrier generation. The decay of the grating is also insensitive to writing fluence.

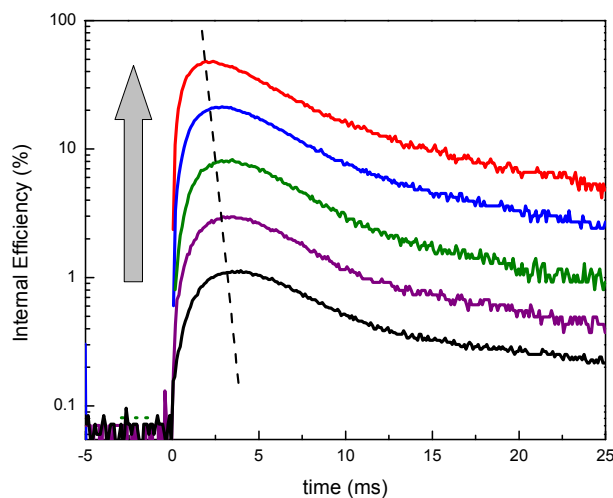


Figure 5-10: The single-pulse diffraction efficiency when the total pulse energy is varied as 0.2, 0.38, 0.75, 1.5, 3.0 mJ/cm². The maximum diffraction efficiency increases linearly with the pulse energy for the most part.

5.3.4 100Hz Frame Rate

Operation of this PR device at 100Hz or higher frame rates requires the decay time to be short too, so that the information from the next frame will not overlap with that from the previous frame. The decay of a grating can be accelerated by uniform

illumination. One can use gated cw illumination at 532nm, a short time after the writing pulse ceases, to help erase the grating. As shown in Figure 5-11, with a gated exposure of only $6\text{mJ}/\text{cm}^2$, we were able to erase the grating in a 10ms window. The delay between the writing pulse and uniform gated exposure can be further adjusted for the best operation. In another possible experimental configuration, a pulsed laser can be employed for both writing (non-uniform illumination) and erasing (uniform illumination). The pulses can be sent at 200Hz, and a fast acousto-optic modulator can switch the polarization between *s* (writing) and *p* (erasing) at 200Hz. In another approach, a chopper can also alternate write and erase pulses.

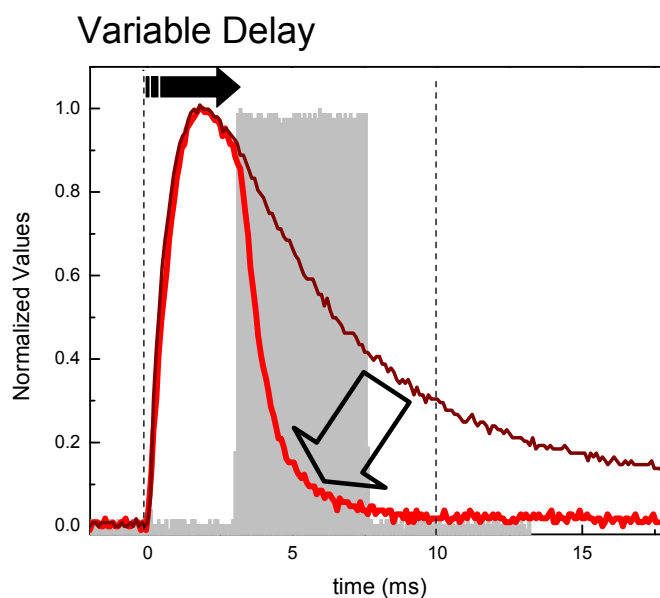


Figure 5-11: The decay of the grating diffraction efficiency is accelerated through a separate, uniform cw illumination at 532nm. The gated illumination lasted only 5ms (gray window) with an exposure of $6\text{mJ}/\text{cm}^2$. The grating is totally erased 10ms

after the pulse arrived. This fast rise and decay proves that we can operate this device at 100Hz (write and erase) frame rates using single pulse writing and gated erasure.

In summary, one can use single-shot pulsed illumination to further improve the dynamic response of PR polymers. The single pulse creates the necessary charge-carriers in a very short time; therefore the speed is limited by the material's drift mobility and chromophore orientation. We have achieved a response time of 300 ns through single pulse writing. Single-shot writing has the further advantage that the recording of gratings is insensitive to vibrations.

5.4 Improving the Grating Persistence in Photorefractive Polymer Composites

Some applications such as large-area 3D display and holographic data storage require a recording medium with long persistence. Inorganic PR crystals such as iron-doped LiNbO₃ have proven to hold gratings for months and even years using approaches such as thermal fixing^{109,110} and two-color (gated) holography¹¹¹. However, in both of these methods, the recording time was very long (100s-6000s), making them impractical for a feasible application. In PR polymers, thermal fixing has been proposed to extend dark decay of gratings.¹¹² However, the efficiency in that demonstration was very low. Improving sensitivity of materials and incorporating innovative experimental techniques (such as thermal fixing) into the recording system is necessary to obtain efficient and persistent PR materials with shorter recording times.

The charge transport and trapping behavior of PR polymeric composites is very critical for controlling the writing speed and persistence of gratings. The relative frontier orbital energies of the constituents in the composite play a key role in determining the lifetime of the grating. Ultimately, a detailed understanding of multi-functional polymer matrices is crucial for controlling the dynamics of the PR gratings for the target applications. The glass-transition temperature of the composite can be adjusted to provide writing at elevated temperatures and when cooled down to room temperature the grating will be rigid with little thermal decay.

The PATPD based polymer composites are efficient and fast, however they lack the necessary persistence. The typical decay time is less than 100ms in cw case and less than 10ms after single-pulse exposure. New material directions are required to improve the lifetime of gratings. Two material directions have so far been taken: (1) include more impurities which has higher HOMO energy level than the other elements composite to act as trapping agents (2) modify the transport matrix to incorporate different side groups with different HOMO energy levels through copolymer approach. The former method has not been successful so far, on the other hand, the second method has been promising and opened a new direction for material studies.

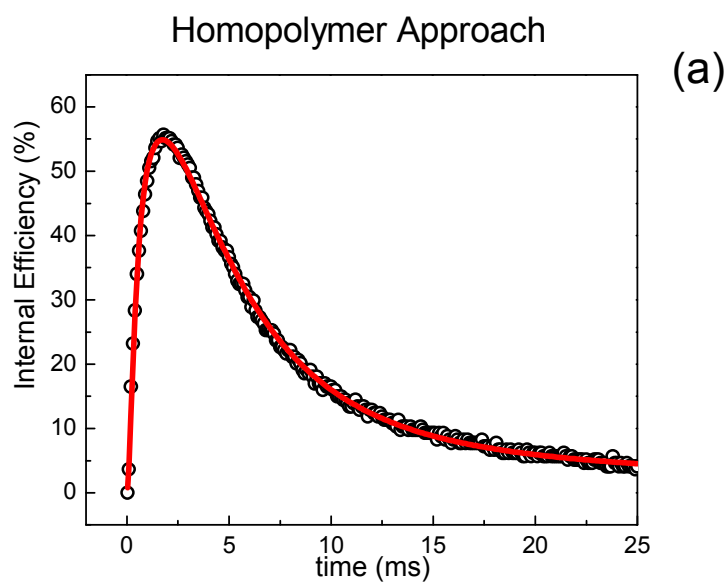
5.4.1 Copolymer Approach

Functional molecules with different HOMO energy levels attached to the backbone of a polymer can alter the trapping properties of a polymer. The charge hopping, transport and trapping can be controlled through relative ratio of functional

elements attached to the copolymer backbone. Modifying the transport matrix in a PR composite can alter the both writing and decay time for the material. During a single-pulse exposure, the decay time of a homopolymer-based composite is < 10 ms; while in the case of copolymer-based composite the decay time can be extended to 1-3 s (see Figure 5-12). The energy of pulse in these measurements was $2.5\text{mJ}/\text{cm}^2$ with a bias voltage of 9kV. Note that, in the copolymer composite, only the transport element has been modified, other functional elements such as NLO chromophores and plasticizers are also incorporated into the composite. As seen in the Figure 5-12, the copolymer approach clearly improves the persistence, in the expense of reduction in the peak diffraction efficiency.

Understanding the charge transport and trapping process is very critical for objectives such as high speed and long persistence. The knowledge of the frontier orbital energy levels is critical to the design and formulation of high performance PR polymers. To meet the objectives required for display applications, we have further explored energy levels, with the goal of combining both rapid response/erase time and image persistence in the same material medium. For example, the more conventional hole-transport matrix poly(*n*-vinylcarbazole) (PVK) (-5.9 eV) sits at an energy level close to 7-DCST (-5.92 eV). It is possible to increase persistence by using this hole transport matrix, while not sacrificing too much write/erase speed. A second approach is to select plasticizers or chromophores that have the ability to provide more persistent traps with PATPD as a host. In addition to that, a more strategic approach is to combine molecules (TPD, carbazole (CbZ) and DCST) that have different frontier orbital energies in a copolymer

system. A composite based on the TPD:CbZ:DCST (5:5:1) copolymer transport moiety which has been developed by the University of Arizona/Nitto Denko Technical team has proven persistent for several seconds (Figure 5-12b) with a maximum 18% diffraction efficiency. A grating erasing ordinarily in seconds can be further fixed with complementary methods such as thermal fixing.



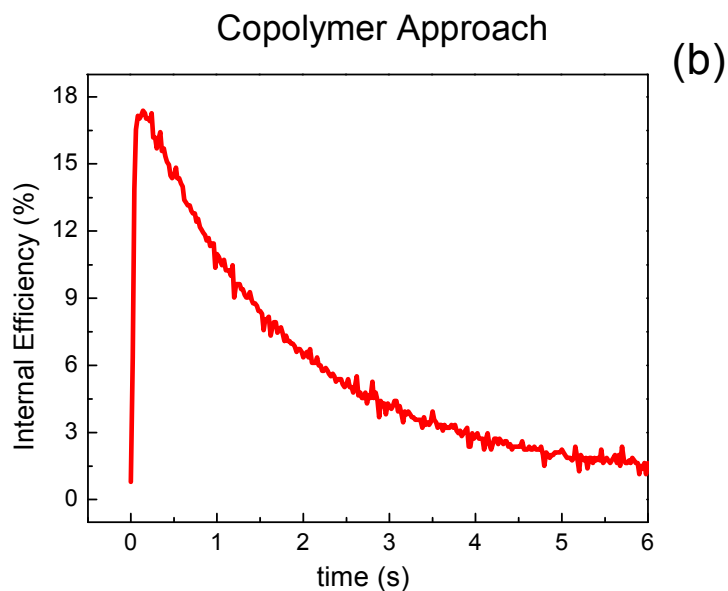


Figure 5-12: The rise and decay of diffraction efficiency in the case of composites based on (a) homopolymer [PATPD:7DCST:ECZ:C₆₀] and (b) copolymer [(TPD:CbZ:DCST/5:5:1) Copolymer: 7F-DCST:ECZ]. The writing was through a single-pulse beam at 532nm with 1ns pulsewidth, 2.5mJ/cm² energy and the reading was with a cw 633nm beam.

Fast writing and long decay times does not usually exist in the same material. To obtain persistence levels of hours, the writing beams are usually switched to cw and the exposure times are above several seconds.

When we analyze the photoconductive properties of three type of copolymers with various TPD:CbZ:7-DCST side chain ratios, the transport and trapping properties will vary. Addition of CbZ increases the trapping and improves the persistence; therefore a reduced photocurrent is observed (Figure 5-13). In this case, the writing takes longer as

well. Elevating the temperature will worsen the persistence of the grating due to increased dark current.

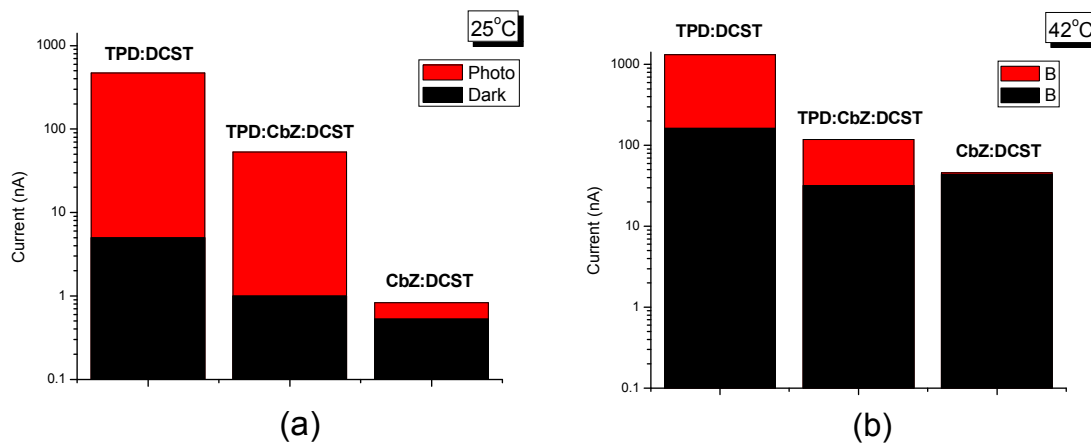


Figure 5-13: The photo and dark current values for PR composites with 3 different copolymer transport elements at 25 °C (a) and at 42 °C (b). TPD:DCST (10:1) copolymer has the largest photocurrent, while CbZ:DCST (10:1) copolymer has the lowest. Note that at elevated temperatures, the dark current becomes very strong and washes out the grating.

5.4.2 Thermal Fixing

Altering the material composition is not sufficient to improve the persistence. Other methods involving tuning of experimental conditions are necessary to further improvement. One of the most promising approaches is thermal fixing. In this technique, the hologram is written in a high- T_g material at elevated temperatures (near T_g) to take advantage of the orientational enhancement effect (see section 2.5.2) and faster recording due to enhanced photoconductivity and chromophore orientational mobility. Then, the

material is quenched to room temperature, freezing the chromophore orientation, decreasing thermal detrapping and ionic dark current and therefore preventing the hologram decay. To conduct such an experiment we have machined a thermal cooling stage and placed the PR sample with a T_g around 40°C in contact with a thermo-electric cooler (TEC) (see Figure 5-14). For best heat removal, the copper stage is water-cooled. The TEC was used for both elevating temperature and fast cooling. Later on, this contact-heating approach is intended to be replaced by CO_2 laser exposure or ITO heating.

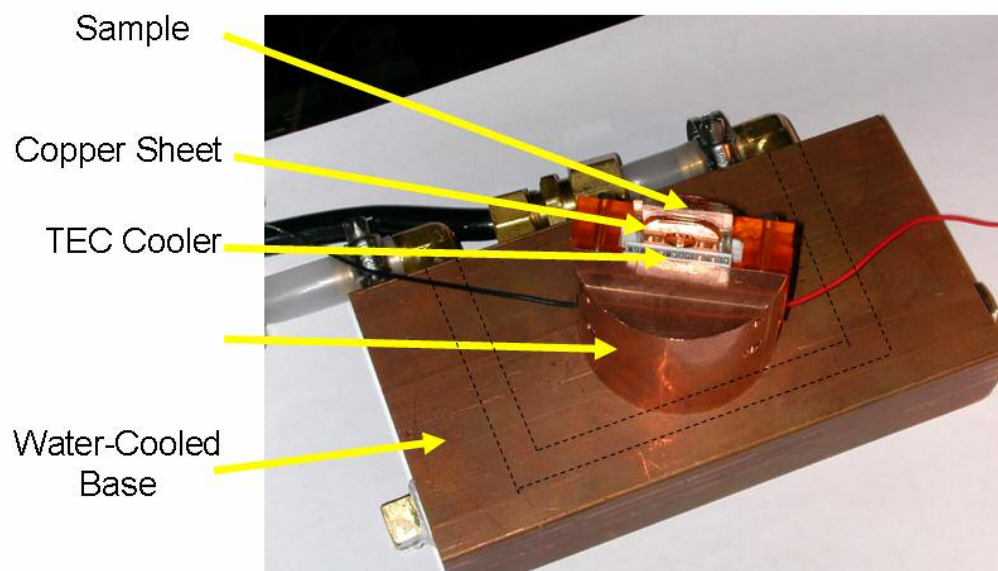


Figure 5-14: Water-cooled thermoelectric apparatus used for thermal fixing tests.

In thermal fixing approach, the grating is written above room temperature (typically $> 40^{\circ}\text{C}$ for our material) and quickly cooled down device to room temperature or below, to freeze the orientation of NLO chromophores. A glass-transition temperature above room-temperature is necessary, therefore the plasticizer is not included in the composition.

Recently, we were able to observe persistent grating with a decay time of 5 hours when we incorporate thermal fixing with the most persistent copolymer composite based on CbZ:DCST (10:1). No plasticizer is included into this composite. Writing beams ($1\text{W}/\text{cm}^2$) exposed the material for 6 seconds at 40°C and this was enough to write a highly efficient grating (Figure 5-15). After the temperature is reduced down to 16°C (which took about 3-4 minutes), the bias voltage was turned off. Even after 16 hours, the efficiency of the grating was at 15% level. The erasure of the rating was done through heating the device to above T_g .

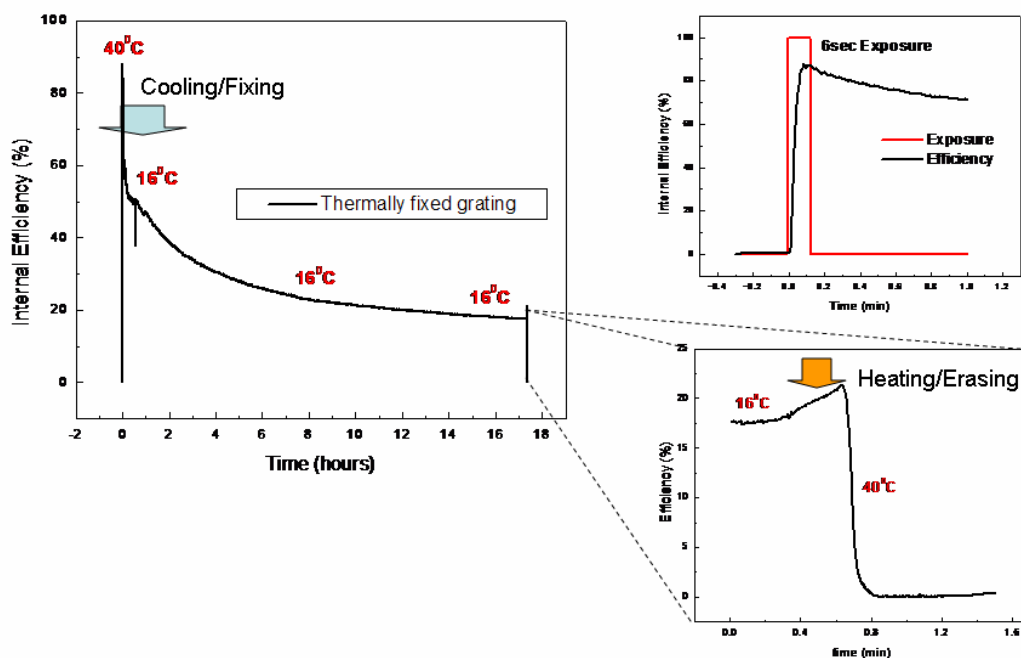


Figure 5-15: The long decay curve for a thermally fixed PR device. The writing was done above 40°C and the device is left to decay at 16°C .

5.5 Large Efficiency in Reflection Geometry

The organic materials have been widely studied in the slanted transmission geometry due to the large efficiencies observed in this particular geometry. However, for some applications the reflection geometry can be more attractive, in particular, when the reconstructing light is preferred to be on the viewer's side and if only a white light source is available for reconstruction of a hologram.

In the standard transmission geometry, the sample has to be slanted when PR polymers are used as recording media. That's because (1) the effective electro-optic coefficient will be non-zero due to the symmetry of poled polymers (2) there will be a component of the applied field along the grating vector \mathbf{K} in order to have a drift source for the transport of the carriers. In polymer composites, the field is necessary to dissociate the charges, drift the carriers and orient the polar molecules (chromophores) that provide a refractive index change. The strength of the projected field depends on the tilt angle. The slant is also necessary for non-zero electro-optic contribution. In a recent publication, PR polymers studied in the reflection geometry had low diffraction efficiency¹¹³. Here, we present a different composite with large efficiency and analyze the angular sensitivity of the volume hologram in reflection geometry.

5.5.1 *Sample Composition and Characterization*

The composite was based on the hole-transport polymer PATPD which was doped with a nonlinear optical chromophore (DBDC), a plasticizer ECZ and C₆₀ as a sensitizer for charge generation at the operating wavelength of 633nm. Composite

prepared included PATPD/DBDC/ECZ/C₆₀ (49.5/30/20/0.5 wt. %). Samples were prepared by laminating 105 μ m thick layers between glass slides with indium tin oxide (ITO) electrodes. The absorption coefficient of the film was measured to be 38 cm⁻¹ at 633nm. The performance of the PR material is judged by the diffraction efficiency of the material, which is measured by four-wave mixing (FWM) experiments. Unlike transmission geometry, each writing beam is incident on different sides of the recording sample. In our configuration, each writing beam had an angle of 72⁰ in air relative to the sample normal (see Figure in section 2.6.2). The writing beams were s-polarized and equal fluence (0.5 W/cm² each) and a weak counter-propagating p-polarized beam probed the efficiency of the grating. The diffracted order was on the same side as the readout beam. The sample was slightly tilted (< 2⁰) to separate the diffracted beam from the reflected beam off the glass surface.

With this geometry, the external bias field has a large projection on the grating vector to create the space charge field. On the other hand due to the symmetry class of poled polymers, the effective electro-optic coefficient will decrease if the writing beam angles are reduced. In our symmetric reflection geometry, the grating spacing is calculated to be 0.235 μ m at the wavelength of 633nm and the slant angle is zero. Notice that, grating spacing is one order less than the case for transmission geometry.

At Bragg-matched incidence, the expression for diffraction efficiency can be simplified into the functional form:

$$\eta = \tanh^2 \left[\frac{\pi \Delta n d}{\lambda \sqrt{\cos \alpha_1 \cos \alpha_2}} \hat{e}_i \cdot \hat{e}_d \right] \quad (95)$$

This function defines internal (lossless) diffraction efficiency in our polymers. The absorption and reflection losses are added later to calculate the external diffraction efficiency.

We have measured the diffraction efficiency in the four-wave mixing geometry as a function of external field under steady-state conditions (Figure 5-16). Instead of observing the usual $\tanh^2(C \Delta n)$ dependence (where C is a constant) as stated in Equation (95), the diffraction efficiency reached to a maximum followed by a successive decrease when the field is ramped up. When we added a slight offset to the readout angle, the diffraction efficiency peaked at different field values depending on the offset. For an external field of $85\text{V}/\mu\text{m}$, the diffraction efficiency has exceeded 30% with a slight offset of reading angle from its initial counter-propagating angle (1.68°). Without the presence of birefringence the Bragg angle is expected to be at the counter-propagating angle. The

usual $\tanh^2(C\Delta n)$ dependence is observed for s-polarized readout (Figure 5-16b).

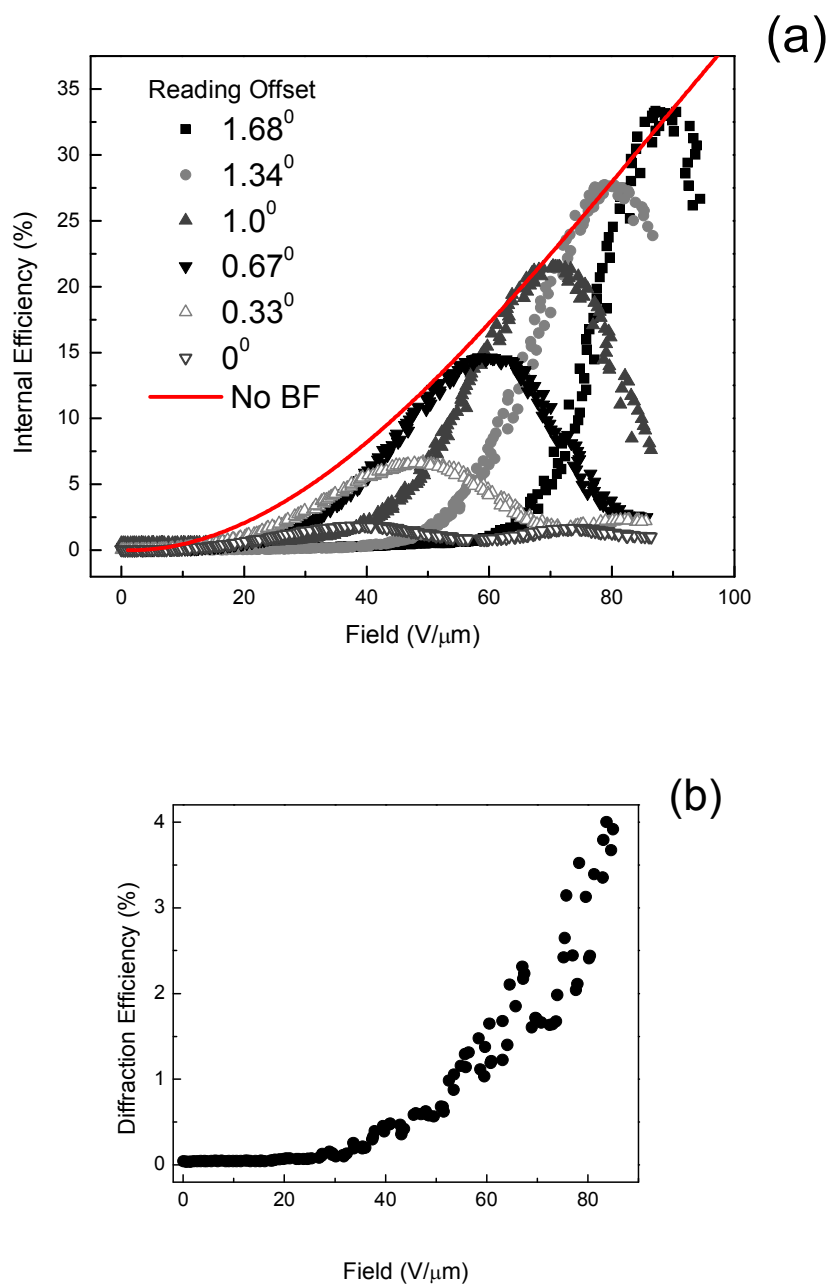


Figure 5-16: (a) Variation of the diffraction efficiency with respect to the external readout angle mismatch (p-polarized readout). As the mismatch angle is varied, the

diffraction efficiency peaks at different field values. The line is the case without birefringence. The case for s-polarized readout is given in (b). An offset angle is not needed in the case of s-polarized readout

The dynamics of the index modulation can be extracted from a bi-exponential function fit that is correlated to the growth of the space charge field. The fast time constant for the build-up of space-charge field was 14ms and the slow time constant was 190 ms for an applied field of 76 V/ μm . In an earlier publication¹¹⁴, the dynamics of the same composition in transmission geometry had similar time constants for rise. In transmission geometry, the grating spacing is much larger. The dynamics is expected to be different in these geometries. The exact reason is not known.

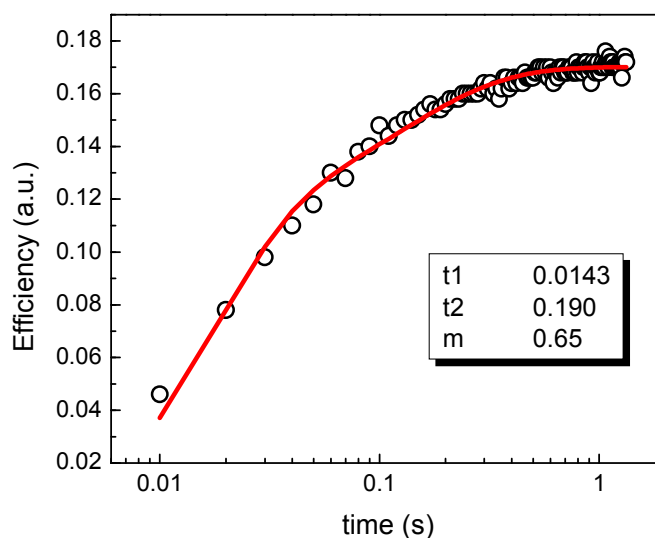


Figure 5-17: The build-up of the diffraction efficiency as the second writing beams is switched on. The data is fitted to a bi-exponential growth function. The fast and slow time constants are given in the inset. The bias voltage was 76V/ μm .

The PR nature of the hologram was confirmed through two-beam coupling measurements. In the case of equal intensity writing beams, the net gain, Γ was more than 80 cm^{-1} at $76 \text{ V}/\mu\text{m}$.

5.5.2 Analysis of Results in Reflection Geometry

The angular selectivity of the PR grating depends on various conditions, such as sample thickness, incident angle of writing beams, refractive index of the material and grating spacing. The thicker the sample or the shorter the grating spacing, the greater the angular selectivity is. In reflection geometry, the PR grating is more sensitive to the angular mismatch compared to the case in transmission geometry. A small variation of the refractive index results in a altered readout angle in the material. When incident readout beam deviates from the Bragg angle, the diffraction efficiency inevitably decreases. Therefore, one should also include the Bragg mismatch equations due the refractive index change in the case of low- T_g polymers to describe the behavior of diffraction efficiency with respect to external field.

In low- T_g PR polymers, the poling of chromophores along the applied field accompanies a change in the refractive index. The linear birefringence has a quadratic relation with field (see Section 2.4.2):

$$\Delta n_x^{(1)} = \Delta n_y^{(1)} = -\frac{1}{2} \Delta n_z^{(1)} \propto E^2 \quad (96)$$

where, $\Delta n_x^{(1)}$, $\Delta n_y^{(1)}$, $\Delta n_z^{(1)}$ are index modulation along each axis. The p-polarized readout beam will sense an increasing refractive index with quadratic field dependence

($\Delta n_{BF}(E_0) = C_0 E_0^2$), where C_0 is a constant. Therefore, the internal angle of readout beam will vary slightly. This would alter the Bragg condition. The variation in internal readout angle can be expressed as:

$$\Delta\alpha(E_0, \alpha_0) = \frac{-\tan(\alpha_1)}{n} C_0 E_0^2 + \alpha_0 \quad (97)$$

where α_1 is the internal read angle, C_0 a constant for refractive index modulation, α_0 the offset angle assigned by experimentalist. The diffraction efficiency of a sample can be measured properly only when the incident angle of the reading beam satisfies the Bragg condition. In Figure 5-16, the decrease in diffraction is believed to be caused by Bragg mismatch due to the variation of refractive index. The material gets more birefringent due to the poling of chromophores.

The other factors in the Kogelnik's coupled wave analysis will be modified as follows:

Obliquity factors

$$\begin{aligned} c_i(E_0, \alpha_0) &= \cos[\alpha_i + \Delta\alpha(E_0, \alpha_0)] \\ c_d(E_0, \alpha_0) &= \cos[\alpha_i + \Delta\alpha(E_0, \alpha_0)] - \frac{\lambda}{[n + \Delta n_{BF}(E_0)] \Lambda(E_0)} \cos \varphi \end{aligned} \quad (98)$$

Other factors

$$\begin{aligned} \nu &= \frac{i\pi\Delta nd}{\lambda\sqrt{c_i c_d}} \hat{e}_i \cdot \hat{e}_d \\ \xi &= \Delta\alpha K d \sin(\varphi - \alpha_1) / 2c_d \end{aligned} \quad (99)$$

Diffraction efficiency:

$$\eta = 1 / \left[1 + \left(1 - \xi^2 / \nu^2 \right) / \sinh^2 \left(\sqrt{\nu^2 - \xi^2} \right) \right] \quad (100)$$

The form of the diffraction efficiency curve is a superposition of its usual \tanh^2 behaviour and the Bragg mismatch due to the variation of birefringence. Overall effect can be calculated and the best fit can be obtained as given in Figure 5-18. A relatively good fit can be obtained for a C_0 value of $1.8e-18$ at the given offset angles.

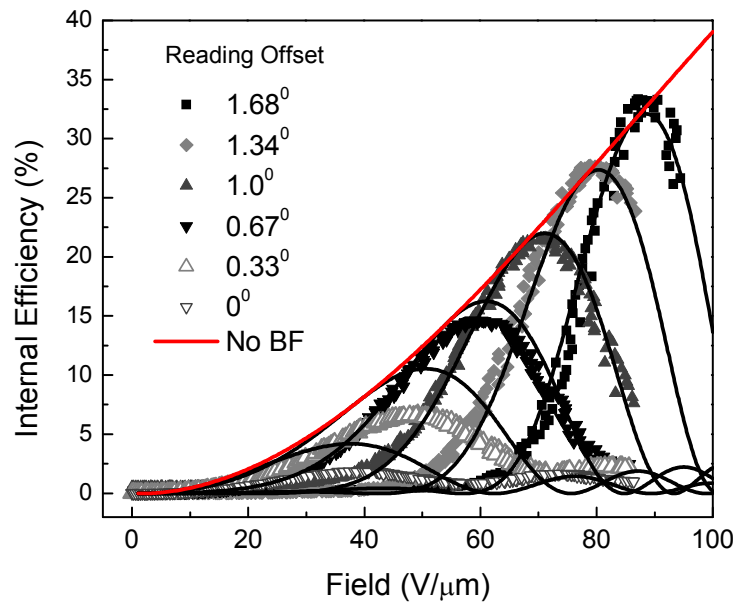


Figure 5-18: Variation of the diffraction efficiency curve with respect to the external readout angle mismatch (p-polarized readout) including the fitted curves based on theory.

On the other hand, in transmission geometry, for a thickness of 100 μm or less, the diffraction efficiency is little affected by the Brag mismatch caused by the variation of the external field (see Figure 2-20). Usually the difference is insignificant, therefore hasn't been taken much into consideration in any of the previous works in this research field.

For the short grating spacing, which is the case for reflection geometry, very large trap densities are required to create significant space-charge fields. Most conventional PR polymers fail in this respect. The resulting refractive index changes in reflection geometry tend to be rather small. In order to get large efficiency in reflection geometry, the effective number of trapping sites has to be increased.

Higher diffraction efficiency values are observed when a PVK based composite PVK:7-DCST:ECZ:BBP:C₆₀ (49.5:35:10:5:0.5 wt.%) is recorded in reflection geometry. A maximum internal diffraction efficiency of 60% has been observed at 85V/ μm . This enhancement in the diffraction efficiency is believed to be due to the larger number of traps in PVK based composite. The efficiency curve is given in Figure 5-19. The birefringence constant C_0 is observed to be less than the previous composite based on PATPD. The speed of PVK based composite was also slower. The PVK composite is also less birefringent, therefore a slight offset in readout angle pushes the peak of the efficiency to high bias fields.

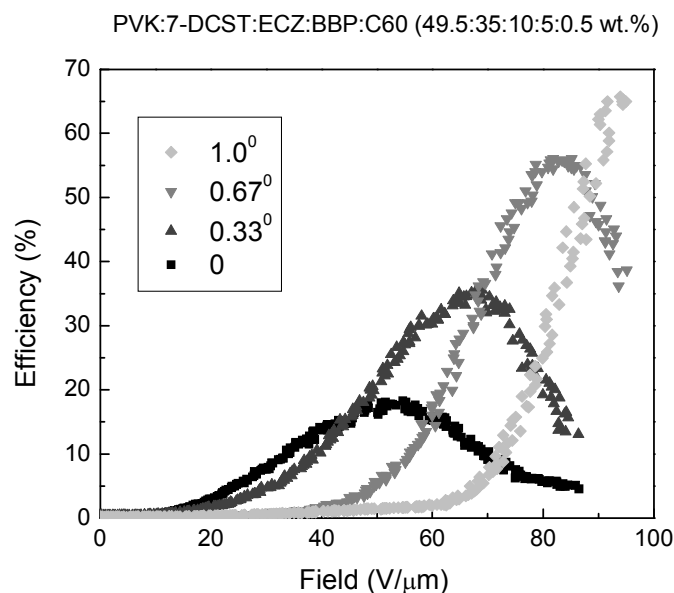


Figure 5-19: Variation of diffraction efficiency as a function of bias field for the composition PVK:7-DCST:ECZ:BBP:C₆₀ (49.5:35:10:5:0.5 wt.%). Each curve has a slight offset by the amount shown in the inset.

In summary, we have demonstrated large diffraction efficiency (up to 60%) in reflection geometry when PR polymers are used as the recording media. The reflection geometry can be useful to get a large viewing angle for recorded holograms, as the field projection on the grating vector will be strong for a wide range of writing angles. The volume PR holograms recorded in reflection are more sensitive to reading angle and slight change in refractive index due to the poling of the chromophores can easily lead to Bragg mismatch. The Bragg-matched reconstruction angle varies with the external field.

6 CONCLUSION AND OUTLOOK

Over the past years, tremendous progress has occurred in both the understanding of the PR effect in many type of materials and the development of high performance materials. The organic PR materials have challenged classical PR materials such as inorganic electro-optic crystals and semiconductors. At present, PR polymers are still leading material choice for many realistic real-time holographic applications. Applications involving rewritable 3D displays are a new direction for PR polymers. Thin films of PR polymers have the advantage of being scalable to large area and can be produced at low cost. The commercial maturity for these materials will be based not only on pure performance characteristics, but also on other criteria, such as reliability, stability and cost.

Despite all this progress for guest-host polymer composites, however, a number of challenges remain. The work presented in this dissertation is intended to address several of challenges in the field of PR polymers and provide the best recording media for applications such as rewriteable 3D displays. There is a need for complex optimization of material for a particular application where many criteria such as efficiency, speed, persistence of holograms, broad spectrum sensitivity and flexible geometries are required. Besides the pure performance characteristics, the PR polymers operating at sub-kilovolts are necessary for practical devices.

We have reduced the high bias voltage required for the operation of guest-host PR polymers to almost 1kV level. This is accomplished by doping the PR composite with two different nonlinear optical chromophores and successfully reducing the device

thickness to the minimum Bragg condition. The current device can be operated at low voltages maintaining the video-rate response time. Even some useful diffraction efficiency of 20% can be achieved at a practical voltage of 750V. We have carefully characterized the PR behavior of device in the transition region between thin and thick hologram.

We have demonstrated high-performance operation of PR polymer composites at near infrared wavelengths of 845nm and 975nm. PR gratings can be written within tens of milliseconds, diffraction efficiency from these gratings can reach almost 100 %. Extending the sensitization of an all organic PR device to the wavelength of almost 1 μm represents a significant advance to the development of all-organic PR devices for infrared imaging and optical communication.

One can use single-shot pulsed illumination to further improve the dynamic response of PR polymers. The single pulse creates the necessary charge-carriers in a very short time; therefore the speed is limited by the material's drift mobility and chromophore orientation. We have achieved a fast response time of 300 μs through single pulse writing. Single-shot writing has the further advantage that the recording of gratings is insensitive to vibrations.

We have demonstrated large diffraction efficiency in symmetric reflection geometry when PR polymers are used as the recording media. The reflection geometry can be useful to get a large viewing angle for recorded holograms, as the field projection on the grating vector will be strong for a wide range of writing angles. The volume PR holograms recorded in reflection geometry reached 60% diffraction efficiency. The

reflection holograms are more sensitive to reading angle and slight change of refractive index due to the poling of the chromophores can easily lead to Bragg mismatch. The Bragg-matched reconstruction angle varies with the magnitude of external field.

Understanding the charge transport and trapping processes is very critical for objectives such as high speed and long persistence. A strategic approach is to combine molecules that have different frontier orbital energies in a copolymer system. A composite based on the CbZ:DCST (10:1) copolymer transport moiety has proven to persist for several minutes. With the addition of thermal fixing, the decay of the grating can be extended to many-hours.

The future direction for thermal fixing approach is to take advantage of selective laser heating of composites with higher glass transition temperatures which can be easily adjusted by the level of plasticizer included. A key aspect of this effort will be to efficiently match laser, material, and substrate properties to achieve both the rapid heating and cooling required. A potential approach is the introduction of engineered nanoparticles with high absorption at the heating wavelength. A novel class of materials called metal nanoshells is reported to absorb at selected IR wavelengths¹¹⁵. The shell can work as an intelligently designed optical absorber and the nanoparticle resonance can be placed anywhere across most of the visible and IR regions of the spectrum, providing for a heating with a commonly available laser wavelength, such as 1.55 μm , to which the rest of the materials are transparent. Hence nanoshell illumination can give rise to very high levels of local heating.

Other new direction for improving the persistence of gratings is addition of a thin (1-20 μm thick) buffer layer. An insulating buffer layer will reduce the amount charges injected into the polymer film, therefore reduce the high dark current when the device is heated up and improve the lifetime of device. A careful selection of buffer layer element with appropriate electrical and conductive properties can improve the grating persistence.

Understanding, the spatial frequency behavior of low- T_g polymer composites is crucial to understand the challenges that will be faced while employing a PR polymer as a recording element for 3D display application. A novel experimental system described in Gunnet-Jepsen et al¹¹⁶ can help to write gratings in a wide range of spatial frequencies, both in reflection and transmission geometry. A further experimental work will be beneficial.

ABBREVIATIONSMaterials:

PVK	poly(<i>N</i> -vinylcarbazole)
CbZ	carbazole
PATPD	poly (acrylic tetraphenyldiaminobiphenyl)
TPD	<i>N,N'</i> -bis(3-methylphenyl)- <i>N,N'</i> -diphenyl-1,1'-biphenyl-4,4'-diamine
PPV	polyphenylenevinylene
TPD-PPV	triphenylamine dimmer phenylenevinylene
TNFM	(2,4,7-trinitro-9-fluorenylidene) malononitrile
TNFDM	(2,4,7-Trinitrofluoren-9-ylidene)malononitrile
7-DCST	4-homopiperidinobenzylidenemalononitrile
DBDC	3-(<i>N,N</i> -di- <i>n</i> -butylaniline-4-yl)-1-dicyanomethylidene-2 cyclohexene
ECZ	<i>N</i> -ethyl carbazole
BBP	butyl benzyl phthalate
PDLC	polymer dispersed liquid crystals
LC	liquid crystal

Others:

PR	photorefractive
OE	orientational enhancement
EO	electro-optic
NLO	nonlinear optical

HOMO	highest occupied molecular orbital
LUMO	lowest unoccupied molecular orbital
CTA	charge transport agent
EA	electron affinity
I_p	ionization potential
CT	charge-transfer
T_g	glass transition temperature
OLED	organic light emitting diode
NIR	near infrared
ITO	indium-tin oxide
TBC	two-beam coupling
FWM	four-wave mixing
DFWM	degenerate four-wave mixing
NFWM	non-degenerate four-wave mixing
TFWM	transient four-wave mixing
TOF	time of flight
EFISH	electric field-induced second harmonic generation
TGHI	time-gated holographic imaging
HTOF	holographic time of flight
DSC	differential scanning calorimetry
OD	optical density
TEC	thermo-electric cooler

PUBLICATIONS & TALKS RELATED TO THIS WORK

- | | |
|---|--|
| JOURNAL PUBLICATIONS | <ol style="list-style-type: none"> 1. M. Eralp, J. Thomas, S. Tay, P. A. Blanche, A. Schülzgen, R. A. Norwood M. Yamamoto and N. Peyghambarian, ‘<i>Variation of Bragg condition in low-glass-transition photorefractive polymers when recorded in reflection geometry</i>’, <i>App. Opt.</i>, in preparation (2007). 2. M. Eralp, J. Thomas, S. Tay, G. Li, A. Schülzgen, R. A. Norwood M. Yamamoto and N. Peyghambarian, ‘<i>Submillisecond response of a photorefractive polymer under single nanosecond pulse exposure</i>’, <i>App. Phys. Lett.</i> 89, 114105 (2006). 3. M. Eralp, J. Thomas, S. Tay, G. Li, A. Schülzgen, R. A. Norwood M. Yamamoto and N. Peyghambarian, ‘<i>Photorefractive polymer device with video-rate response time operating at low voltages</i>’, <i>Opt. Lett.</i> 31, 1408 (2006). 4. G. Li, M. Eralp, J. Thomas, S. Tay, S. R. Marder, A. Schülzgen, R. A. Norwood and N. Peyghambarian, ‘<i>All-optical dynamic correction of communication signals using a photorefractive polymeric hologram</i>’, <i>App. Phys. Lett.</i>, 86, 161103 (2005). 5. M. Eralp, J. Thomas, S. Tay, G. Li, G. Meredith, A. Schülzgen, S. R. Marder and N. Peyghambarian, ‘<i>High-performance photorefractive polymer operating at 975nm</i>’, <i>App. Phys Lett</i> 85, 1095 (2004). |
| REVIEW ARTICLE | <p>J. Thomas, M. Eralp, S. Tay, M. Yamamoto, R. Norwood, N. Peyghambarian, ‘<i>Photorefractive polymers with superior performance</i>’, <i>OPN</i> December 2005, page 35.</p> |
| CONFERENCE TALKS AND PROCEEDINGS | <ol style="list-style-type: none"> 1. M. Eralp, J. Thomas, S. Tay, G. Li, R. A. Norwood and N. Peyghambarian, "<i>Photorefractive polymer in reflection geometry with large efficiency</i>", SPIE Optics & Photonics Conference, 2006, San Diego, CA. 2. M. Eralp, J. Thomas, S. Tay, G. Li, R. A. Norwood and N. Peyghambarian, ‘<i>Photorefractive polymer in reflection geometry with large efficiency</i>’, <i>Proc. SPIE</i> 6331 (2006). 3. M. Eralp, J. Thomas, G. Li, J. Winiarz, S. Tay, A. Schülzgen, R. Norwood and N. Peyghambarian, "<i>Photorefractive polymer device operating at practical voltages</i>", The 89th OSA Annual Meeting, <i>Frontiers in Optics</i>, 2005, Tucson, AZ (Invited). 4. M. Eralp, S. Tay, J. Thomas S. Marder, G. Meredith, A. Schülzgen and N. Peyghambarian, "<i>Photorefractivity with non-destructive readout at near-infrared wavelengths</i>", OSA 2003 Meeting, <i>Frontiers in Optics</i>, 2003, Tucson, AZ. |

REFERENCES

1. C. T. DeRose, Y. Enami, C. Loychik, R. A. Norwood, D. Mathine, M. Fallahi, J. D. Luo, A. K.-Y. Jen, M. Kathaperumal, M. Yamamoto and N. Peyghambarian, *Appl. Phys. Lett.* **89**, 131102 (2006).
2. J. H. Burroughes, D. D. C. Bradley, A. R. Brown, R. N. Marks, K. Mackay, R. H. Friend, P. L. Burns, and A. B. Holmes, *Nature* **347**, 539(1990).
3. L. S. Hung and C. H. Chen, *Materials Science & Engineering Reports* **39**, 143 (2002).
4. N. S. Saricifici, L. Smilowitz, A. J. Heeger, and F. Wudi, *Science* **258**, 1474 (1992).
5. P. Peurnans, A. Yakimov, and S. R. Forrest, *J. App. Phys.* **93**, 3693 (2003).
6. A. Tswnura, H. Koezuka, and T. Ando, *App. Phys. Lett* **49**, 1210 (1986).
7. G. Horowitz, *J. Mat. Res.* **19**, 1946 (2004).
8. J. D. Bhawalkar, G. S. He, and P. N. Prasad, *Reports on Progress in Physics* **59**, 1041 (1996).
9. Y. Enami, C. T. DeRose, C. Loychik, D. Mathine, R. A. Norwood, J. Luo, A. K.-Y. Jen, N. Peyghambarian, *Appl. Phys. Lett.* **89**, 143506 (2006).
10. C. J. Drury, M. J. Mutsaers, C. M. Hart, M. Matters and D. M. de Leeuw, *App. Phys. Lett* **73**, 108 (1998).
11. T. R. Hebner, C. C. Wu, D. Marcy, M. H. Lu, and J. C. Stunn, *App. Phys. Lett* **72**, 519 (1998).
12. J. A. Herlocker, C. Fuentes-Hernandez, J. F. Wang, N. Peyghambarian, B. Kippelen, Q. Zhang, and S. R. Marder, *App. Phys. Lett* **80**, 1156 (2002).
13. A. Ashkin, G. D. Boyd, J. M. Dziedzic, R. G. Smith, A. A. Baliman, J. J. Levinstein, and K. Nassau, *App. Phys. Lett* **13**, 233 (1966).
14. P. Günter and J.-P. Huignard, *Photorefractive Materials and Their Applications I*, Springer-Verlag, Berlin, (1988).
15. P. Yeh, *Introduction to Photorefractive Nonlinear Optics*, John Wiley, New York, (1993).

16. L. Solymar, D. J. Webb, A. Grunnet-Jepsen, *The Physics and Applications of Photorefractive Materials*, Clarendon Press, Oxford, (1996).
17. K. Sutter, P. Gunter, *J. Opt. Soc. Am. B-Opt. Phys.* **7**, 2274 (1990).
18. K. Sutter, J. Hulliger, P. Gunter, *Solid State Commun.* **74**, 867 (1990).
19. S. Ducharme, J.C. Scott, R. J. Twieg, W. E. Moerner, *Phys. Rev. Lett.* **66**, 1846 (1991).
20. O. Ostroverkhova, W.E. Moerner, *Chem.Rev.* **104**, 3267 (2004).
21. E. Mecher, F. Gallego-Gómez, H. Tillmann, H. Hörhold, J. C. Hummelen, K. Meerholz, *Nature* **418**, 959 (2002).
22. M. Eralp, J. Thomas, S. Tay, G. Li, G. Meredith, A. Schülzgen, G. A. Walker, S. Barlow, S. R. Marder and N. Peyghambarian, *App. Phys. Lett.* **85**, 1095 (2004).
23. S. Tay, J. Thomas, M. Eralp, G. Li, S. Marder, G. A. Walker, S. Barlow, M. Yamamoto, R. Norwood, A. Schülzgen and N. Peyghambarian, *App. Phys. Lett* **87**, 171105 (2005).
24. S. Bartkiewicz, K. Matczyszyn, A. Miniewicz, and F. Kajzar, *Opt. Commun.* **187**, 257-261 (2001).
25. G. Cook, C. A. Wyres, M. J. Deer, and D. C. Jones, *Proc. SPIE* **5213**, 63-77 (2003).
26. G. Cook, J. L. Carns, M. A. Saleh, and D. R. Evans, *Mol. Cryst. Liq. Cryst.* **453**, 141 (2006).
27. J. A. Herlocker, C. Fuentes-Hernandez, J. F. Wang, N. Peyghambarian, B. Kippelen, Q. Zhang, S. R. Marder, *Appl. Phys.Lett.* **80**, 1156 (2002).
28. Zilker, S. J. *ChemPhysChem* **2**, 333 (2002).
29. P. Günter and J.-P. Huignard, *Photorefractive Materials and Their Applications II*, Springer-Verlag, Berlin, (1989).
30. R. A., Fischer, Ed, *Optical Phase Conjugation*, Academic Press, New York, (1983).
31. B.L. Volodin, Sandalphon, K. Meerholz, B. Kippelen, N.V. Kukhtarev, and N.

- Peyghambarian, *Opt. Eng.* **34**, 2213 (1995).
32. B. Volodin, B. Kippelen, K. Meerholz, B. Javidi, and N. Peyghambarian, *Nature* **383**, 58 (1996).
33. A. Goonesekera, D. Wright, W.E. Moerner, *Appl. Phys. Lett.* **76**, 3358 (2000).
34. J.P. Huignard and A. Marrakchi, *Opt. Comm.* **38**, 249 (1981).
35. B.L. Volodin, Sandalphon, K. Meerholz, B. Kippelen, N.V. Kukhtarev, and N. Peyghambarian, *Opt. Eng.* **34**, 2213 (1995).
36. D.D. Steele, B.L. Volodin, O. Savina, B. Kippelen, N. Peyghambarian, H. Röckel, and S.R. Marder, *Opt. Lett.* **23**, 153 (1998).
37. B. Kippelen, S.R. Marder, E. Hendrickx, J.L. Maldonado, G. Guillemet, B.L. Volodin, D.D. Steele, Y. Enami, Sandalphon, Y.J. Yao, J.F. Wang, H.R. Röckel, L. Erskine, and N. Peyghambarian, *Science* **279**, 54 (1998).
38. N. Cheng, B. Swedek, and P. N. Prasad, *Appl. Phys. Lett.* **71**, 1828 (1997).
39. G. Li, M. Eralp, J. Thomas, S. Tay, A. Schülzgen, R. A. Norwood, and N. Peyghambarian *App. Phys. Lett.* **86**, 161103 (2005).
40. M. Lucente, *IBM Sys. Journal* **35**, 349 (1996).
41. Lecture *Holography and optical phase conjugation* held at ETH Zurich by Prof. G. Montemezzani (2002).
42. L. Onsager, *Phys. Rev.* **54**, 554 (1938).
43. A. Mozumder, *J. Chem Phys.* **60**, 4300 (1974).
44. P. M. Borsenberger, D. S. Weiss, *Organic Photoreceptors for Imaging Systems*, Marcel Dekker, New York (1993).
45. O. Ostroverkhova, W. E. Moerner, M. He and R. J. Twieg, *Appl. Phys. Lett.* **82**, 3602 (2003).
46. T. K. Daubler, R. Bittner, K. Meerholz, V. Cimrova, D. Neher, *Phys. Rev. B* **61**, 13515 (2000).

47. O. Ostroverkhova, K. D. Singer, *J. Appl. Phys.* **92**, 1727 (2002).
48. E. Hendrickx, Y. D. Zhang, K. B. Ferrio, J. A. Herlocker, J. Anderson, N. R. Armstrong, E. A. Mash, A. P. Persoons, N. Peyghambarian, B. Kippelen, *J. Mater. Chem.* **9**, 2251 (1999).
49. P. W.M. Blom, M. Vissenberg, *Mater. Sci. Eng. R* **27**, 53 (2000).
50. H. Bassler, *Phys. Status Solidi B* **175**, 15 (1993)
51. L.B. Shein, A. Peled, and D. Glatz, *J. App. Phys.* **66**, 686 (1989).
52. J. S. Schildkraut, Y. Cui, *J. Appl. Phys.* **72**, 5055 (1992).
53. A. Miller and E. Abrahams, *Phy. Rev.* **120**, 745 (1960).
54. R. A. Marcus, *Annu. Rev. Phys. Chem.* **15**, 155 (1964).
55. E. Hendrickx, B. Kippelen, S. Thayumanavan, S. R. Marder, A. Persoons, N. Peyghambarian, *J. Chem. Phys.* **112**, 9557 (2000).
56. A. Goonesekera, S. Ducharme, *J. Appl. Phys.* **85**, 6506 (1999).
57. S. A. Visser, W. T. Gruenbaum, E. H. Magin, P. M. Borsenberger, *Chem. Phys.*, **240**, 197 (1999).
58. P. M. Borsenberger, E. H. Magin, J. A. Sinicropi, L. B. Lin, *Jpn. J. Appl. Phys. Part* **37**, 166 (1998).
59. T. Jakob, S. Schloter, U. Hofmann, M. Grasruck, A. Schreiber, D. Haarer, *J. Chem. Phys.* **111**, 10633 (1999).
60. S. J. Zilker, M. Grasruck, J. Wolff, S. Schloter, A. Leopold, M. A. Kol'chenko, U. Hofmann, A. Schreiber, P. Strohhriegl, C. Hohle, D. Haarer, *Chem. Phys. Lett.* **306**, 285 (1999).
61. L. Kulikovskiy, D. Neher, E. Mecher, K. Meerholz, H. H. Horhold, O. Ostroverkhova, *Phys. Rev. B* **69**, 125216 (2004).
62. O. Ostroverkhova and K. D. Singer, *J. App. Phys.* **92**, 1727 (2002).

63. Grunnet-Jepsen, A., Wright, D., Smith, B., Bratcher, M. S., DeClue, M. S., Siegel, J. S., Moerner, W. E., *Chem. Phys. Lett.* **291**, 553 (1998).
64. N.V. Kukharev, V.B. Markov, S. G. Odulov, M. S. Soskin, and V. L. Vinetskii, *Ferroelectrics* **22**, 949 (1979).
65. W. E. Moerner, S. M. Silence, *Chem. Rev.* **94**, 127 (1994).
66. S. M. Silence, D. M. Burland, W. E. Moerner, in *Photorefractive Effects and Materials* (ed. D. D. Nolte), 265, Kluwer Academic Publishers, Boston (1995).
67. S. Ducharme, *Proc. SPIE* **2526**, 144 (1995).
68. W. E. Moerner, A. Grunnet-Jepsen, C. L. Thompson, *Ann. Rev. Mater. Sci.* **27**, 585 (1997).
69. W. Helfrich, *Physics and Chemistry of the Organic Solid State, Vol. 111*, ed. by D. Fox, M. M. Labes, and A. Weissberger, pp. 22-24, Wiley-Interscience, New York (1967).
70. D. M. Burland, R. D. Miller, and C. A. Walsh, *Chem. Rev.* **94**, 31 (1994).
71. M. G. Kuzyk, R. C. Moore and L. A. Kin, *J. Opt Soc Am B* **7**, 64 (1990).
72. G. T. Boyd, C. V. Francis, J. E. Trend and D. A. Ender, *J. Opt. Soc. Am. B* **8**, 887 (1991).
73. Oudar, J.L. and Chemla, D.S., *J. Chem. Phys.* **66**, 2664 (1977).
74. C. R. Moylan, R. D. Miller, R. J. Twieg, V. Y. Lee, *Polym. Second-Order Nonlinear Opt.* **601**, 66 (1995).
75. R. Wortmann, C. Poga, R. J. Twieg, C. Geletneky, C. R. Moylan, R. M. Lundquist, R. G. DeVoe, P. M. Cotts, H. Horn, J. E. Rice, D. M. Burland, *J. Chem. Phys.* **105**, 10637 (1996).
76. P. C. Mehta, V. V. Rampal, *Lasers and Holography*, World Scientific Publishing Co.: Singapore (1993).
77. H. Kogelnik, *Bell Syst. Tech. J.*, **48**, 2909 (1969).

78. M. G. Moharam, L. Young, *Appl. Opt.* **17**, 1757 (1978).
79. E. Hendrickx, B. L. Volodin, D. D. Steele, J. L. Maldonado, J. F. Wang, B. Kippelen, N. Peyghambarian, *Appl. Phys. Lett.* **71**, 1159 (1997).
80. L. P. Yu, *J. Polym. Sci. A: Polym. Chem.* **39**, 2557 (2001).
81. G. P. Wiederrecht, *Annu. Rev. Mater. Res.* **31**, 139 (2001).
82. C. Sanchez, B. Lebeau, F. Chaput, J. P. Boilot, *Adv. Mater.* **15**, 1969 (2003).
83. J. G. Winiarz, L. M. Zhang, M. Lal, C. S. Friend, P. N. Prasad, *Chem. Phys.* **245**, 417 (1999).
84. D. J. Binks, D. P. West, S. Norager, P. O'Brien, *J. Chem. Phys.* **117**, 7335 (2002).
85. S. Wang, S. Yang, C. Yang, Z. Li, J. Wang, W. Ge, *J. Phys. Chem. B* **104**, 11853 (2000).
86. F. Wang, Z. J. Chen, B. Zhang, Q. H. Gong, K. W. Wu, X. S. Wang, B. W. Zhang, F. Q. Tang, *Appl. Phys. Lett.* **75**, 3243 (1999).
87. M. Liphardt, A. Goonesekera, S. Ducharme, J. M. Takacs, and L. Zhang, *J. Opt. Soc. Am. B* **13**, 2252 (1996).
88. W. E. Moerner, S. M. Silence, F. Hache, G. C. Bjorklund, *J Opt. Soc. Am. B* **11**, 320 (1994).
89. S. H. Chung and J. R. Stevens, *Am. J. Phys.* **11**, 1024 (1991).
90. K. Meerholz, B. L. Volodin, Sandalphon, B. Kippelen and N. Peyghambarian, *Nature* **371**, 497 (1994).
91. D. Wright, M. A. Diaz-Garcia, J. D. Casperson, M. DeClue, W. E. Moerner, and R. J. Twieg, *Appl. Phys. Lett.* **73**, 1490 (1998).
92. J. A. Herlocker, K. B. Ferrio, E. Hendrickx, B. D. Guenther, S. Mery, B. Kippelen and N. Peyghambarian, *Appl. Phys. Lett.* **74** (16), 2253 (1999).
93. E. Mecher, F. Gallego-Gómez, H. Tillmann, H. Hörhold, J. C. Hummelen, K. Meerholz, *Nature* **418**, 959 (2002).

94. D. Wright, U. Gubler, Y. Roh, W. E. Moerner, M. He, R. J. Twieg, *Appl. Phys. Lett.* **79**, 4274 (2001).
95. B. Kippelen, N. Peyghambarian, In *Polymers for Photonic Applications II*; Vol. 161, Springer-Verlag: Berlin (2003).
96. M. Eralp, J. Thomas, G. Li, S. Tay, A. Schülzgen, R. A. Norwood, N. Peyghambarian, and M. Yamamoto, *Opt. Lett.* **31**, 1408 (2006).
97. J. Thomas, C. Fuentes-Hernandez, M. Yamamoto, K. Cammack, K. Matsumoto, G. Walker, S. Barlow, G. Meredith, B. Kippelen, S. R. Marder, N. Peyghambarian, *Adv. Mater.* **16**, 2032 (2004).
98. C. A. Walsh, W. E. Moerner, *J. Opt. Soc. Am. B* **9**, 1642 (1992).
99. J. G. Winiarz, L. Zhang, J. Park, P.N. Prasad, *J. Phys. Chem. B* **106**, 967 (2002).
100. J.G. Winiarz, L. Zhang, M. Lal, C.S. Friend, P.N. Prasad, *J. Am. Chem. Soc.*, **121**, 5287-95 (1999).
101. C. Engels, D. Van Steenwinckel, E. Hendrickx, M. Schaerlaekens, A. Persoons, and C. Samyn, *J. Mater. Chem.* **12**, 951 (2002).
102. L. M. Wang, M. K. Ng, and L. P. Yu, *Appl. Phys. Lett.* **78**, 700 (2001).
103. O. Ostroverkhova, W.E. Moerner, M. He, R. J. Twieg, *App. Phys. Lett.* **82**, 3602 (2003).
104. B. Kippelen, Sandalphon, K. Meerholz and N. Peyghambarian, *Appl. Phys. Lett.* **68**, 1748 (1996).
105. R. Bittner, C. Brauchle, K. Meerholz, *Appl. Opt.*, **37** 2843 (1998).
106. M. Eralp, J. Thomas, S. Tay, G. Li, A. Schülzgen, R. A. Norwood, M. Yamamoto, and N. Peyghambarian, *App. Phys. Lett.* **89**, 114105 (2006).
107. U. Hofmann, A. Schreiber, D. Haarer, S. J. Zilker, A. Bacher, D. D. C. Bradley, M. Redecker, M. Inbasekaran, W. W. Wu and E. P. Woo, *Chem. Phys. Lett.* **311**, 41 (1999).

108. J. Wolff, S. Schloter, U. Hofmann, D. Haarer, and S. J. Zilker, *J. Opt. Soc. Am. B* **16**, 1080 (1999).
109. A. Me´ndez, L. Arizmendi, *Opt. Mat.* **10**, 55 (1998).
110. E. M. de Miguel-Sanz, M. Carrascosa and L. Arizmendi, *Phys Rev B* **65**, 165101 (2002).
111. H. Guenther, R. Macfarlane, Y. Furukawa, K. Kitamura, and R. Neurgaonkar, *Appl. Opt.* **37**, 7611 (1998).
112. N. Cheng, B. Swedek, and P. N. Prasad, *Appl. Phys. Lett.* **71**, 1828 (1997).
113. O-P. Kwon, G. Montemezzani, P. Gnter, and S-H. Lee, *App. Phys. Lett.* **84**, 43-45 (2004).
114. C. Fuentes-Hernandez, J. Thomas, R. Termine, G. Meredith, S. Barlow, G. Walker, K. Cammack, K. Matsumoto, M. Yamamoto, S. R. Marder, B. Kippelen, N. Peyghambarian, *App. Phys. Lett.* **85**, 1877 (2004).
115. L. R. Hirsch, R. J. Stafford, J. A. Bankson, S. R. Sershen, B. Rivera, R. E. Price, J. D. Hazle, N. J. Halas, and J. L. West, *PNAS* **100**, 13549 (2003).
116. A. Grunnet-Jepsen, C. L. Thompson, and W. E. Moerner, *J. Opt. Soc. Am. B* **15**, 905 (1998).